

The JWST Spectroscopic Properties of Galaxies at $z = 9 - 14$

MENGTAO TANG,¹ DANIEL P. STARK,² CHARLOTTE A. MASON,^{3,4} VIOLA GELLI,^{3,4} ZUYI CHEN,^{1,3,4} AND
MICHAEL W. TOPPING¹

¹*Steward Observatory, University of Arizona, 933 N Cherry Ave, Tucson, AZ 85721, USA*

²*Department of Astronomy, University of California, Berkeley, Berkeley, CA 94720, USA*

³*Cosmic Dawn Center (DAWN)*

⁴*Niels Bohr Institute, University of Copenhagen, Jagtvej 128, 2200 Copenhagen N, Denmark*

ABSTRACT

We characterize the *JWST* spectra of 61 galaxies at $z = 9 - 14$, including 30 newly-confirmed galaxies. We directly compare the $z > 9$ spectroscopic properties against 401 galaxies at $6 < z < 9$, with the goal of identifying evolution in the star formation histories and ISM. We measure rest-UV emission line properties and UV continuum slopes, while also investigating the rest-optical emission lines for the subset of galaxies at $9.0 < z < 9.6$. With these spectra, we constrain the stellar masses, specific star formation rates, dust attenuation, and the average metallicity and abundance pattern of $z > 9$ galaxies. Our dataset indicates that the emission lines undergo a marked change at $z > 9$, with extremely large C III], H β , and H γ EWs becoming $2 - 3\times$ more common at $z > 9$ relative to $6 < z < 9$. Using the spectra, we infer the distribution of SFRs on short (SFR_{3Myr}) and medium (SFR_{3-50Myr}) timescales, finding that rapid SFR upturns (large SFR_{3Myr}/SFR_{3-50Myr} ratios) are significantly more likely among $z > 9$ galaxies. These results may reflect a larger dispersion in UV luminosity at fixed halo mass and larger baryon accretion rates at $z > 9$, although other physical effects may also contribute. We suggest that the shift in star formation conditions explains the prevalence of extreme nebular spectra that have been detected at $z > 9$, with hard ionizing sources and nitrogen-enhancements becoming more typical at the highest redshifts. Finally, we identify five $z > 9$ spectroscopically confirmed galaxies with red UV colors ($\beta \gtrsim -1.5$), either revealing a small population with moderate dust attenuation ($\tau_V = 0.23 - 0.35$) or very high density nebular-dominated galaxies with hot stellar populations.

Keywords: High-redshift galaxies (734); Observational cosmology (1146)

1. INTRODUCTION

Over the last few years, deep *JWST* (Gardner et al. 2023; Rigby et al. 2023) imaging has provided the first robust constraints on the census of galaxies at $z > 9$ (see Stark et al. 2025 for a review). Early *JWST*/NIRCam (Rieke et al. 2023) imaging campaigns revealed a surprisingly large volume density of luminous $z \gtrsim 10$ galaxies (e.g., Naidu et al. 2022; Castellano et al. 2022; Adams et al. 2023; Finkelstein et al. 2023; Harikane et al. 2023; Whitler et al. 2023a; Casey et al. 2024; Hainline et al. 2024a; Robertson et al. 2024). Most recently, the redshift frontier has been extended to $z \simeq 14$ (Carniani et al. 2024; Naidu et al. 2025), revealing that the popu-

lation of extremely luminous galaxies is already in place within 300 Myr following the Big Bang. Current photometric samples now exceed 400 $z \gtrsim 9$ galaxies, allowing the luminosity function to be reliably measured across numerous fields (e.g., Bouwens et al. 2023; Donnan et al. 2023, 2024; Harikane et al. 2023, 2025; Adams et al. 2024; Finkelstein et al. 2024; McLeod et al. 2024; Whitler et al. 2025). The integrated ultraviolet (UV) luminosity density revealed by these surveys has been shown to be significantly greater than what had been predicted by many groups prior to the launch of *JWST*.

The physical origin of the excess UV luminosity density remains unclear. Some have argued that the evolution can be explained if the dispersion in UV luminosity at fixed halo mass (σ_{UV}) increases with redshift (e.g., Mason et al. 2023; Mirocha & Furlanetto 2023; Shen et al. 2023; Kravtsov & Belokurov 2024), or increases

with decreasing halo mass (e.g., Katz et al. 2023; Sun et al. 2023; Gelli et al. 2024; Feldmann et al. 2025), perhaps reflecting stronger bursts of star formation and a shift to galaxy formation in lower mass halos at earlier epochs. Others have suggested that the star formation efficiency (SFE) may be larger than previously expected at higher redshifts, perhaps a result of redshift evolution (e.g., Dekel et al. 2023; Qin et al. 2023; Somerville et al. 2025) or larger SFE at moderately low halo masses (Feldmann et al. 2025). Additionally, Ferrara et al. (2023) and Mason et al. (2023) have suggested that the slow evolution at the bright end of the luminosity function at $z \gtrsim 9$ may be explained if dust attenuation is reduced at earlier times, driven in part by the efficient ejection of dust from luminous galaxies with extremely large specific star formation rates (e.g., Ziparo et al. 2023).

New observations will be required to determine which of these physical effects are most important in driving the luminosity function evolution at the highest redshifts. Deep spectroscopy provides one of the most immediate avenues for insight. The ratio of the emission line luminosity and underlying continuum emission (the equivalent width, EW) is very sensitive to the recent star formation history, reaching extremely large values in the midst of strong bursts. If σ_{UV} increases toward higher redshift rapidly at $z > 9$, it should leave its imprint on the emission line EW distributions. If star formation conditions evolve at $z > 9$, we may also expect to see a sudden change in properties of the gas, dust, and ionizing sources, all of which can be probed with *JWST* spectroscopy.

NIRSpec (Jakobsen et al. 2022; Böker et al. 2023) observations of the luminous galaxy GN-z11 provided our first look at the spectra of $z \gtrsim 9$ galaxies (Bunker et al. 2023). The spectrum revealed numerous strong emission lines, pointing to a dense population of massive stars formed in a recent burst (see also Maiolino et al. 2024). The emission line ratios reveal dense ionized gas, hard ionizing agents, and a nitrogen-enhanced abundance pattern, all of which are atypical in spectra at lower redshifts. Subsequent spectra have revealed that GN-z11 is not anomalous. The luminous galaxies GHZ2 (Castellano et al. 2024) and MoM-z14 (Naidu et al. 2025) both exhibit similar emission line spectra, potentially also related to strong bursts of star formation. It is conceivable that the emergence of such extreme nebular spectra may hint at a shift in star formation conditions, plausibly linked to the physics that is driving the excess UV luminosity in early galaxies.

The goal of this paper is to provide statistical context necessary to identify evolution in the spectroscopic

properties of galaxies at $z \gtrsim 9$. Previous work has investigated the evolution in the mean emission line properties of the galaxy population, utilizing composite spectra with 30 galaxies at $z \gtrsim 9$ (Roberts-Borsani et al. 2024). Others have investigated the UV continuum slopes in prism spectra using a sample of 19 $z \gtrsim 9.5$ galaxies (Saxena et al. 2024). Since these studies, spectroscopic samples at $z \gtrsim 9$ have grown in number, following a series of campaigns with NIRSpec. Here we utilize the latest spectroscopic database available in the public archive to identify whether there is strong evolution in galaxy properties at $z \gtrsim 9$. We compare the NIRSpec properties of 61 galaxies at $z > 9$ to a sample of 401 galaxies at $6 < z < 9$, quantifying evolution in the dust content, gas properties, and stellar populations at the highest redshifts probed by *JWST*.

The organization of this paper is as follows. In Section 2, we describe the sample of galaxies at $z > 9$ identified from publicly available *JWST*/NIRSpec observations. We present the UV continuum slopes and emission line properties of galaxies in our $z > 9$ sample in Section 2.5. Using the emission line measurements, we characterize the stellar populations and the gas properties $z > 9$ galaxies in Section 4. We then describe the evolution in galaxy spectra from $6 < z < 9$ to $z > 9$ in Section 5. In Section 6, we discuss the evolution in the stellar populations, ionizing sources, and dust content at $z > 9$. Finally, we summarize our conclusions in Section 7. Throughout the paper we adopt a Λ -dominated, flat universe with $\Omega_\Lambda = 0.7$, $\Omega_M = 0.3$, and $H_0 = 70 \text{ km s}^{-1} \text{ Mpc}^{-1}$. All magnitudes are quoted in the AB system (Oke & Gunn 1983) and all EWs are quoted in the rest frame.

2. SPECTROSCOPIC SAMPLE SELECTION

In this section, we construct a sample of galaxies at $z > 9$ with publicly-available NIRSpec spectra. We introduce the NIRSpec spectra in Section 2.1, and then select the $z > 9$ sample in Section 2.2. In Section 2.3, we create $z > 9$ composite spectra. We then describe the photometry measurements in Section 2.4, and the emission line and continuum measurements in Section 2.5. Finally, we introduce the photoionization modeling approaches to infer the physical properties of $z > 9$ galaxies in Section 2.6.

2.1. *JWST*/NIRSpec Spectra

We use the NIRSpec spectra obtained from the following public observations: the *JWST* Advanced Deep Extragalactic Survey¹ (JADES, GTO 1180, 1181, PI:

¹ <https://jades-survey.github.io/>

D. Eisenstein, GTO 1210, 1286, PI: N. Lützgendorf, GTO 1287, PI: K. Isaak, GO 3215, PIs: D. Eisenstein & R. Maiolino; Eisenstein et al. 2023a,b; Bunker et al. 2024; D’Eugenio et al. 2025), the GLASS-JWST Early Release Science Program² (GLASS, ERS 1324, PI: T. Treu; Treu et al. 2022), the Cosmic Evolution Early Release Science³ (CEERS, ERS 1345, PI: S. Finkelstein; Finkelstein et al. 2025) and a Director’s Discretionary Time program (DDT 2750, PI: P. Arrabal Haro; Arrabal Haro et al. 2023a,b), the Ultra-deep NIRCcam and NIRSpec Observations Before the Epoch of Reionization⁴ (UNCOVER, GO 2561, PI: I. Labbé & R. Bezanson; Bezanson et al. 2024; Price et al. 2025), the Red Unknowns: Bright Infrared Extragalactic Survey⁵ (RUBIES, GO 4233, PIs: A. de Graaff & G. Brammer; de Graaff et al. 2025), the CANDELS-Area Prism Epoch of Reionization Survey (CAPERS, GO 6368, PI: M. Dickinson; Kokorev et al. 2025), GO 1871 (PI: J. Chisholm; Chisholm et al. 2024), GO 3073 (PI: M. Castellano; Castellano et al. 2024; Napolitano et al. 2025), and GO 4287 (PI: C. Mason; Whittler et al. 2025, in preparation). All the NIRSpec observations were performed with the multi-object spectroscopy (MOS) mode using the micro-shutter assembly (MSA; Ferruit et al. 2022). We refer readers to the above references for detailed descriptions of the NIRSpec observations.

The NIRSpec spectra were reduced following the same approaches described in Topping et al. (2025a) using the standard JWST data reduction pipeline⁶ (Bushouse et al. 2024). For each object, we extract the 1D spectrum from the reduced 2D spectra using a boxcar extraction. We set the extraction aperture to match the emission line profile or the continuum along the spatial direction, with a typical width of 5 pixels (~ 0.5 arcsec in spatial direction). We refer readers to Topping et al. (2025a) and Tang et al. (2024b) for a full description of the analysis of the spectra of the public spectroscopic sample.

2.2. Sample Selection of $z > 9$ Galaxies

Using the public NIRSpec data sets described in the above subsection, we identify a sample of galaxies with spectroscopic redshifts at $z > 9$. We determine the spectroscopic redshifts as follows. First, we visually inspect the 2D NIRSpec spectra, searching for Ly α break. We choose to search for Ly α break instead of emission lines

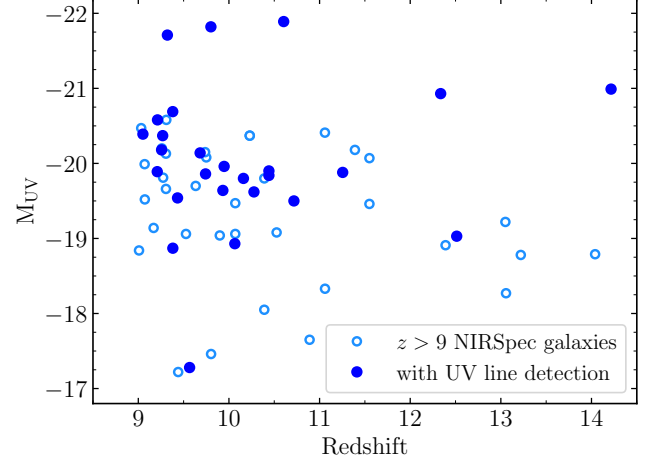


Figure 1. Spectroscopic redshifts and absolute UV magnitudes of the 61 galaxies in our $z > 9$ sample. We highlight sources with rest-frame UV emission line (N IV], C IV, He II, O III], N III], C III]) detections with solid blue circles. Those without UV line detections are shown by open dodger blue circles.

for two reasons: 1) strong rest-frame optical emission lines (H β , [O III]) are often shifted out of the NIRSpec spectrum at $z > 9$, and 2) to ensure we are not biased against sources with weak emission lines (e.g., extremely metal-poor galaxies). We identify 61 galaxies at $z > 9$ with Ly α break. Next, we search for emission lines in these 61 galaxies to derive more accurate spectroscopic redshifts. We find 34 galaxies with optical emission line detections ([O II], [Ne III], H γ , H β , or [O III]), and we derive their redshifts with the following approach. We simultaneously fit the available optical emission lines with Gaussian profiles, and compute the redshifts using the line centers. For the remaining 27 galaxies without emission line detections, we derive their redshifts from Ly α break. We verify the Ly α break inferred redshifts of these 27 galaxies following the approaches described in Tang et al. (2024b). We fit their NIRCcam photometry with population synthesis models (see Section 2.6), varying redshift in the range of $0 < z < 15$. The best-fit redshifts are consistent with those derived from Ly α breaks in the NIRSpec spectra within $\Delta z < 0.3$. Therefore, we adopt the Ly α break inferred redshifts for the subset without emission line detections. Overall, we measure the spectroscopic redshifts of the 61 galaxies in our sample at $9.01 < z < 14.22$ (Figure 1).

In Table B1 we list the 61 galaxies in our $z > 9$ sample, which are in six independent fields: the Abell 2744, the Cosmological Evolution Survey (COSMOS), the Extended Groth Strip (EGS), the Great Observatories Origins Deep Survey (GOODS) North and South, and the UltraDeep Survey (UDS) fields. There are 14, 3, 10, 9,

² <https://glass.astro.ucla.edu/ers/>

³ <https://ceers.github.io/>

⁴ <https://jwst-uncover.github.io/>

⁵ <https://annadeg.github.io/projects/RUBIES/>

⁶ <https://github.com/spacetelescope/jwst>

17, and 8 galaxies in the Abell 2744, COSMOS, EGS, GOODS-N, GOODS-S, and UDS fields, respectively. All these 61 galaxies have low resolution ($R \sim 100$) prism spectra, which were taken in the CEERS, JADES, UNCOVER, RUBIES, CAPERS, and GO 3073 programs. The exposure time of the 61 prism spectra at $z > 9$ spans from 0.8 to 46.7 hours, with a median of 4.4 hours. For a galaxy with $H = 27.7$ (the median magnitude of our $z > 9$ sources) at $z = 10$, this median depth corresponds to a 3σ rest-frame EW limit of 23 \AA . Medium resolution ($R = 1000$) grating spectra have also been obtained in 26 of the 61 galaxies at $z > 9$, which were all taken in the JADES programs. For this subset with $R = 1000$ spectra, the exposure time spans from 0.9 to 11.7 hours for G140M (median 2.2 hours), 0.9 to 6.9 hours for G235M (median 2.6 hours), and 0.9 to 46.7 hours for G395M (median 2.6 hours). The typical EW limits (for an $H = 27.7$ galaxy at $z = 10$) are 17, 18, and 37 \AA in the three configurations, respectively.

The NIRSpec spectra of 31 of the 61 galaxies in our $z > 9$ sample have been presented in literature (Arrabal Haro et al. 2023a,b; Bunker et al. 2023; Curtis-Lake et al. 2023; Wang et al. 2023; Carniani et al. 2024; Castellano et al. 2024; Curti et al. 2025; D’Eugenio et al. 2024; Fujimoto et al. 2024; Hainline et al. 2024b; Heintz et al. 2024; Tang et al. 2024b; Kokorev et al. 2025; Napolitano et al. 2025; Pollock et al. 2025; Witstok et al. 2025a). We have newly identified 30 galaxies at $z > 9$, and we show their spectra in Figure B1. Our sample of 61 galaxies is about $2\times$ larger than that used in earlier studies of $z > 9$ galaxies with NIRSpec (Roberts-Borsani et al. 2024; Heintz et al. 2025). We will present the emission line and continuum measurements of our $z > 9$ sample in Section 2.5.

2.3. Construction of Composite $z > 9$ Spectra

To investigate the average spectroscopic properties of galaxies in our $z > 9$ sample, we create composite spectra by stacking individual spectra. To maximize the sample size for creating composite spectra, we stack the low resolution prism spectra. We construct a stack with the following methods. We first shift individual spectra to the rest-frame using the derived spectroscopic redshifts (Section 2.2). Each spectrum is then interpolated to a common rest-frame wavelength scale (10 \AA per wavelength bin) and normalized by its luminosity density at rest-frame 1500 \AA . Finally, the spectra are median stacked without weighting to avoid bias towards bright systems or those with deep spectra. The composite luminosity density and its uncertainty in each wavelength bin are derived from the median and the stan-

dard deviation of the luminosity densities of individual sources in that bin.

Here we aim to characterize the rest-frame UV to optical emission lines from the composite spectra. We first create a composite spectrum by stacking the prism spectra of all the 61 galaxies in our sample at $9.0 < z < 14.3$. This allows us to constrain the average EWs of rest-frame UV emission lines (e.g., N IV], C IV, O III], C III]) of entire $z > 9$ sample, as well as [O II] and [Ne III] emission lines at redshift up to $z = 12.6$ (56 galaxies). To measure strong rest-frame optical emission lines (e.g., $H\beta$, [O III]), we create another composite spectrum by stacking the spectra of galaxies at a narrower redshift window $9.0 < z < 9.6$, since $H\beta$ and [O III] are shifted out of NIRSpec spectra at $z > 9.6$. The stack at $9.0 < z < 9.6$ contains 22 galaxies, and our goal is to constrain the $H\beta$ EW, [O III] $\lambda\lambda 4959, 5007$ /[O II] $\lambda 3728$ ratio, and electron temperature and oxygen abundance from [O III] $\lambda 4363$ and [O III] $\lambda 5007$ measurements. In Figure 2 we show the two composite spectra at $9.0 < z < 14.3$ and $9.0 < z < 9.6$. We will present the emission line measurements of the composite spectra in Section 2.5.

2.4. Photometric Measurements

We characterize the absolute UV magnitudes and UV slopes of the 61 galaxies in our $z > 9$ sample from their NIRCам photometry. Details of the NIRCам photometry used in this work are described in Tang et al. (2024b). In brief, we utilize the reduced NIRCам images (Valentino et al. 2023) and photometry catalogs released on the DAWN JWST Archive⁷ (DJA; Valentino et al. 2023). The NIRCам images were obtained from CEERS, JADES, UNCOVER, and the Public Release IMaging for Extragalactic Research (PRIMER, GO 1837, PI: J. Dunlop) programs. We use imaging taken with six broad-band filters (F115W, F150W, F200W, F277W, F356W, F444W) and two medium-band filters (F335M, F410M) if available. For each source, we use the photometry measured in the 0.5 arcsec diameter circular apertures and corrected to the “total” fluxes within elliptical Kron (Kron 1980) apertures.

For each galaxy in the $z > 9$ sample, we cross-match its coordinate with the photometry catalog and identify the best-matched source by visually inspecting the image. For the 14 galaxies in the Abell 2744 field, we correct their photometry for gravitational lensing using the magnifications reported in Price et al. (2025), which

⁷ <https://dawn-cph.github.io/dja/>

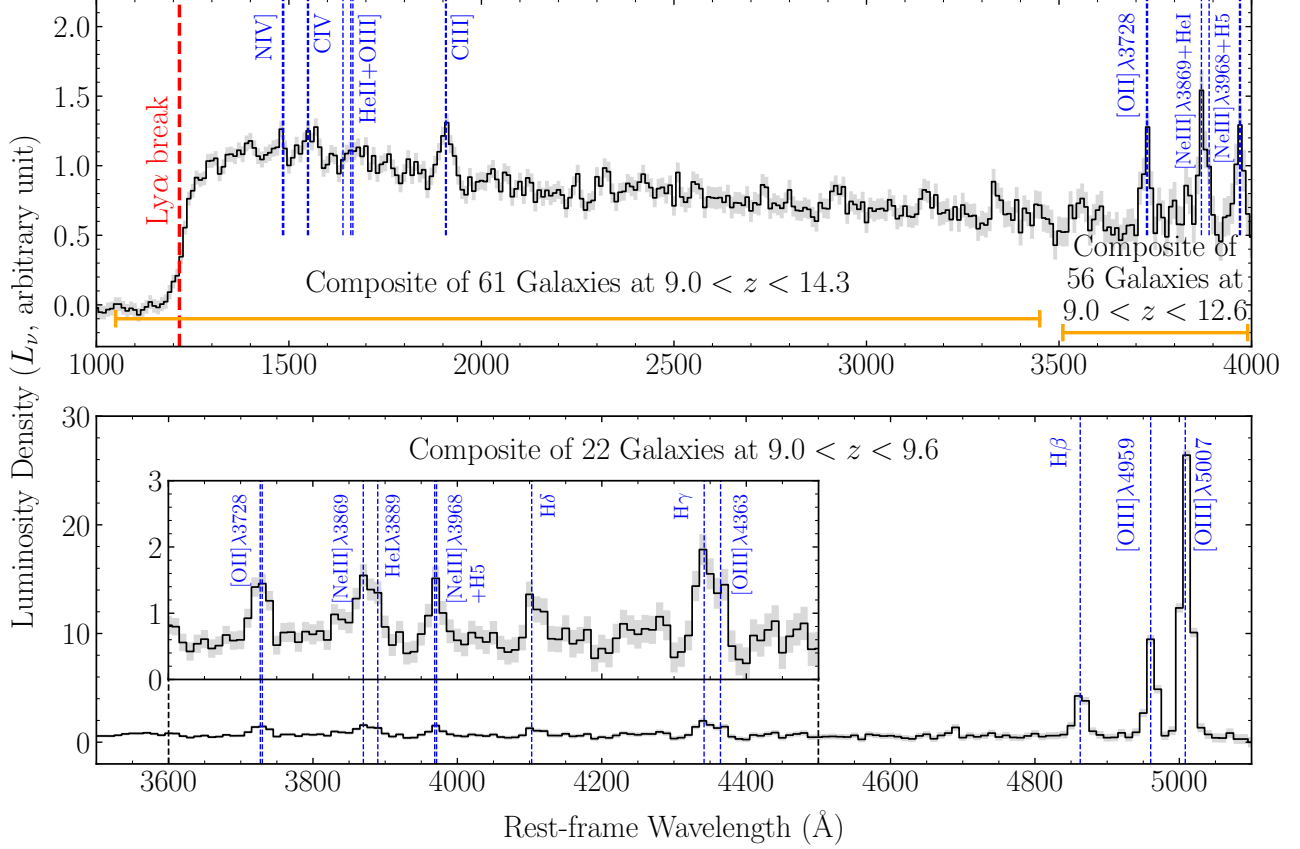


Figure 2. Composite prism spectra of galaxies in our $z > 9$ sample. The top panel shows the stack of all the 61 galaxies at in our $z > 9$ sample ($9.0 < z < 14.3$). The spectrum at rest-frame $\sim 3500 - 4000 \text{ \AA}$ is composed of 56 galaxies at $9.0 < z < 12.6$. The bottom panel shows the composite at rest-frame optical wavelengths obtained by stacking 22 galaxies at $9.0 < z < 9.6$. Emission line detections are marked by blue dashed lines. The grey shaded region presents the 1σ uncertainty of flux density.

are derived from the Furtak et al. (2023) lensing models. The median magnification correction factor of these 14 systems is 1.6. The absolute UV magnitudes (M_{UV}) of the 61 galaxies in our $z > 9$ sample range from -21.9 to -17.2 , with a median of $M_{\text{UV}} = -19.8$ (Figure 1).

2.5. Emission Line and Continuum Measurements

We characterize the emission line fluxes and EWs as well as the UV continuum slopes for the 61 galaxies in our $z > 9$ sample. Using the measured spectroscopic redshifts (Section 2.2), we search for rest-frame UV emission lines (N IV], C IV, He II, O III], N III], and C III]) and available rest-frame optical emission lines ([O II], [Ne III], H γ , [O III] λ 4363, H β , and [O III] λ 5007) in both the low resolution prism spectra and the medium resolution grating spectra.

The line fluxes and EWs are computed from the extracted 1D spectra as follows. We first determine the underlying continuum. For each emission line we fit the continuum nearby the line with a power law ($f_\lambda \propto \lambda^\beta$). In the grating spectra of a subset of our $z > 9$ galaxies,

the continua are not detected ($S/N < 3$) and we adopt the continua measured from the prism spectra of the same sources. For the subset of galaxies with continua detected in both prism and grating spectra, we find that the continua measured from both spectra of the same sources are consistent. Then we measure the emission line fluxes from the continuum-subtracted spectra. For emission lines detected with relatively high S/N (> 5), we compute the line fluxes by fitting the line profiles with Gaussian functions. We use a single Gaussian function for each isolated emission line. For emission lines that are close in wavelength (e.g., [Ne III] λ 3869 and He I λ 3889, H γ and [O III] λ 4363), we simultaneously fit them with multiple Gaussians. For emission lines detected with lower S/N (< 5), we compute the line fluxes from direct integration. Using emission lines with $S/N > 5$, we find that Gaussian fit and direct integration result in similar fluxes. To compute the uncertainties of the line fluxes, we resample the flux densities of each spectrum 1000 times by taking the observed value as the mean and the error as standard deviation. We

then measure the line fluxes from the resampled spectra following the same methods described above and take the standard deviations as the uncertainties. We note that for C IV emission, the flux (and hence EW) may be underestimated at prism resolution due to the underlying absorption. For undetected lines, we derive the 3σ upper limit of line flux by summing the error spectrum in quadrature over 1 instrument resolution element ($\simeq 3000 \text{ km s}^{-1}$ for low resolution prism and $\simeq 300 \text{ km s}^{-1}$ for medium resolution grating spectrum) around the expected line center. The EW (EW limit) of a detected (undetected) emission line is computed by dividing the line flux (flux limit) with the underlying continuum flux density.

We also search for emission lines in the composite spectra of $z > 9$ galaxies constructed in Section 2.3. In the stack of all the 61 galaxies in our $z > 9$ sample ($9.0 < z < 14.3$, top panel of Figure 2), we identify a clear C III] $\lambda 1908$ emission with S/N of 7. We also detect N IV] $\lambda 1485$, C IV $\lambda 1549$, and blended He II $\lambda 1640$ + O III] $\lambda 1663$ emission lines with S/N of 3 – 4. At rest-frame $\sim 3500 - 4000 \text{ \AA}$, the composite spectrum of the 56 galaxies at $9.0 < z < 12.6$ (top panel of Figure 2) presents [O II] $\lambda 3728$, [Ne III] $\lambda 3869$, and [Ne III] $\lambda 3968$ emission lines. For the stack of the 22 galaxies at $9.0 < z < 9.6$ (bottom panel of Figure 2), we identify a suite of rest-frame optical emission lines including [O II] $\lambda 3728$, [Ne III] $\lambda 3869$, and [Ne III] $\lambda 3968$, H δ , H γ , [O III] $\lambda 4363$, H β , [O III] $\lambda 4959$, and [O III] $\lambda 5007$. The fluxes and EWs of emission lines detected in the composite spectra are computed following the same approaches described above. We present the emission line EWs and line ratios measured from the composite spectra at $z > 9$ in Table 1.

We measure the UV continuum slopes (β) from the prism spectra of $z > 9$ galaxies. Of the 61 galaxies in our $z > 9$ sample, 60 have prism spectra covering rest-frame UV wavelengths (the rest-frame UV spectrum of CAPERS-UDS-142042 falls in the detector gap, see Figure B1). For each of these 60 objects, we fit a power law to its prism spectrum in the rest-frame wavelength range $1400 - 2700 \text{ \AA}$. This wavelength range is chosen to be similar to that adopted in the standard Calzetti et al. (1994) approach, minimizing the impact of the Ly α break and the intergalactic medium (IGM) damping wing (Heintz et al. 2025; Mason et al. 2025). We also mask regions at rest-frame $1440 - 1590 \text{ \AA}$, $1620 - 1680 \text{ \AA}$, and $1860 - 1980 \text{ \AA}$ to avoid strong emission lines (e.g., Saxena et al. 2024). To estimate the uncertainty of UV slope measurement of each source, we resample the rest-frame UV continuum flux densities 1000 times and fit the UV slope for each resampled spectrum with the

Table 1. Emission line measurements from the composite spectra of $z > 9$ galaxies.

Composite at $9.0 < z < 14.3$	
# of Galaxies	61
N IV] EW	$5.0 \pm 1.2 \text{ \AA}$
C IV EW	$5.3 \pm 1.4 \text{ \AA}$
He II+O III] EW	$4.3 \pm 1.3 \text{ \AA}$
C III] EW	$12.6 \pm 1.8 \text{ \AA}$
C IV/C III]	0.77 ± 0.24
Composite at $9.0 < z < 12.6$	
# of Galaxies	56
[Ne III] $\lambda 3869$ /[O II] $\lambda 3728$	1.17 ± 0.30
Composite at $9.0 < z < 9.6$	
# of Galaxies	22
H γ EW	$51 \pm 7 \text{ \AA}$
H β EW	$150 \pm 12 \text{ \AA}$
[O III] $\lambda 5007$ EW	$819 \pm 13 \text{ \AA}$
H γ /H β	0.460 ± 0.071
[O III] $\lambda 5007$ /H β	5.2 ± 0.4
([O III]+[O II])/H β	7.5 ± 0.6
[Ne III] $\lambda 3869$ /[O II] $\lambda 3728$	0.88 ± 0.15
[O III] $\lambda \lambda 4959, 5007$ /[O II] $\lambda 3728$	13.4 ± 1.7
[O III] $\lambda 4363$ /H γ	0.42 ± 0.12
[O III] $\lambda 4363$ /[O III] $\lambda 5007$	0.037 ± 0.009

same approaches described above. Then we take the standard deviation of the UV slopes derived from the resampled spectra as the uncertainty. For these 60 galaxies at $z > 9$, the 16th-50th-84th percentiles of the UV slopes are $\beta = -2.64$, -2.33 , and -2.01 , respectively. We present the UV slopes and C III], C IV EWs of our $z > 9$ galaxies in Table B1.

2.6. Photoionization modeling

To explore the stellar population and gas properties of $z > 9$ galaxies, we fit the NIRCам spectral energy distributions (SEDs) and emission lines using the Bayesian galaxy SED modeling and interpreting tool BayEsian Analysis of GaLaxy sEds (BEAGLE, version 0.29.2; Chevallard & Charlot 2016). The BEAGLE tool utilizes the latest version of the Bruzual & Charlot (2003) stellar population synthesis models and the Gutkin et al. (2016) photoionization models of star-forming galaxies with the CLOUDY code (Ferland et al. 2013).

We first fit the rest-frame optical emission line fluxes ([O II] $\lambda 3728$, [Ne III] $\lambda 3869$, H γ , [O III] $\lambda 4363$, H β ,

[O III] $\lambda 4959$, [O III] $\lambda 5007$) as well as the $H\gamma$ and $H\beta$ EWs measured from the composite spectrum to infer the average interstellar medium (ISM) properties at $z > 9$. We assume a constant star formation history (CSFH), allowing the galaxy age to vary between 1 Myr and the age of the Universe at the given redshift with a log-uniform prior. In these models, the hydrogen-ionizing spectrum reaches close to a steady state after 10 Myr of CSFH, and we allow the stellar age to vary to larger values to reproduce the Balmer line EWs. We also assume the Chabrier (2003) initial mass function (IMF) with a stellar mass range of $0.1 - 300 M_\odot$. The metallicity is set to vary in the range $-2.2 \leq \log(Z/Z_\odot) \leq 0$ ($Z_\odot = 0.01524$; Caffau et al. 2011), and the interstellar metallicity is set to equal to the stellar metallicity. We allow the dust-to-metal mass ratio (ξ_d) to vary within the range $0.1 \leq \xi_d \leq 0.5$. The ionization parameter U is adjusted in the range $-4.0 \leq \log U \leq -1.0$. We adopt log-uniform priors for metallicity and ionization parameter, and a uniform prior for dust-to-metal mass ratio. For dust attenuation, we apply the Small Magellanic Cloud (SMC) extinction curve (Pei 1992), allowing the V -band optical depth τ_V to vary between 0.001 and 5 with a log-uniform prior. We apply the prescription of Inoue et al. (2014) to account for the absorption of IGM.

To infer the stellar populations and star formation histories (SFHs), we then fit the SEDs and available C III], $H\gamma$, $H\beta$, and [O III] $\lambda 5007$ EWs of the 61 individual galaxies in our $z > 9$ sample. Here we consider two component SFH models (TcSFH), which allow for a more flexible SFH with a wide range of recent variations in star formation rate (SFR). We adopt a similar TcSFH modeling procedure as that described in Endsley et al. (2024b). The TcSFH models consist of an exponentially delayed SFH component ($\text{SFR} \propto t \cdot e^{-t/\tau}$, where t is the time since the onset of star formation) and a CSFH component. For the delayed SFH component, we allow the star formation timescale τ to span the range between 1 Myr and 30 Gyr. We set t to be between 20 Myr and the age of the Universe at the given redshift. The CSFH component defines the most recent SFH, and the timescale of the recent CSFH component is fitted between 1 Myr and 20 Myr. The strength of the CSFH component is parameterized in terms of specific star formation rate (sSFR) over this period (relative to the final formed stellar mass) in the range $-14 \leq \log(\text{sSFR}/\text{yr}^{-1}) \leq -6$. We adopt log-uniform priors for all the above parameters. For gas properties (ionization parameter, metallicity, dust-to-metal ratio) and dust attenuation, we apply the same fitting ranges and priors as for fitting the composite spectrum.

The assumed SFH can impact the recovered stellar mass (e.g., Carnall et al. 2019; Tacchella et al. 2022; Whitler et al. 2023b). To explore the range of stellar masses for each object, we also fit the SEDs with two alternative SFHs. We consider single CSFH models using BEAGLE, which we expect to provide a lower bound on the stellar masses. We also fit the SEDs with models that incorporate non-parametric SFHs using Prospector (Leja et al. 2019; Johnson et al. 2021), which is based on the Flexible Stellar Population Synthesis code (Conroy et al. 2009, 2010) and the nebular emission models of Byler et al. (2017). We adopt the same Prospector model parameters and priors as in Whitler et al. (2023b), which are also similar to those applied in the BEAGLE models described above. The non-parametric SFH models are piecewise constant functions in time. We adopt five age bins spanning from the time of observation to the lookback time corresponding to a formation redshift z_{form} (we set $z_{\text{form}} = 20$): 0 – 3 Myr, 3 – 10 Myr, 10 – 30 Myr, 30 – 100 Myr, and > 100 Myr. We use the ‘continuity’ prior in Prospector, which allows a smoothly evolving SFR over time.

From the BEAGLE and Prospector fitting, we derive the median value and the marginalized 68% credible interval from the posterior probability distribution for each fitted parameter. We will discuss the photoionization modeling results in Section 4

3. SPECTROSCOPIC PROPERTIES AT $z > 9$

In this section, we present the spectroscopic properties of the galaxies in our $z > 9$ sample. We discuss the UV continuum slopes in Section 3.1. Then we characterize the C III] and O III] (Section 3.2), C IV and He II (Section 3.3), N IV] and N III] (Section 3.4), Balmer emission lines (Section 3.5), [O II], [Ne III], and [O III] in rest-frame optical (Section 3.6), and the [O III] $\lambda 4363$ auroral emission lines (Section 3.7).

3.1. UV continuum slopes

The UV continuum slopes are sensitive to a range of physical properties. The intrinsic slopes are set by the stellar population and ionized gas conditions ($\beta = -2.6$ to -2.4) before being reddened by dust in the ISM (e.g., Cullen et al. 2017; Reddy et al. 2018; Topping et al. 2024a). If $z > 9$ galaxies are different from those at $6 < z < 9$, we may expect to see evolution in the UV colors. Early *JWST* papers focused on measurement of UV slopes at $z > 9$ using NIRCcam photometry, revealing blue colors that appear close to the intrinsic values for ionization-bounded H II regions ($\beta \simeq -2.6$; e.g., Cullen et al. 2024; Franco et al. 2024; Topping et al. 2024a). More recently, spectroscopic samples have

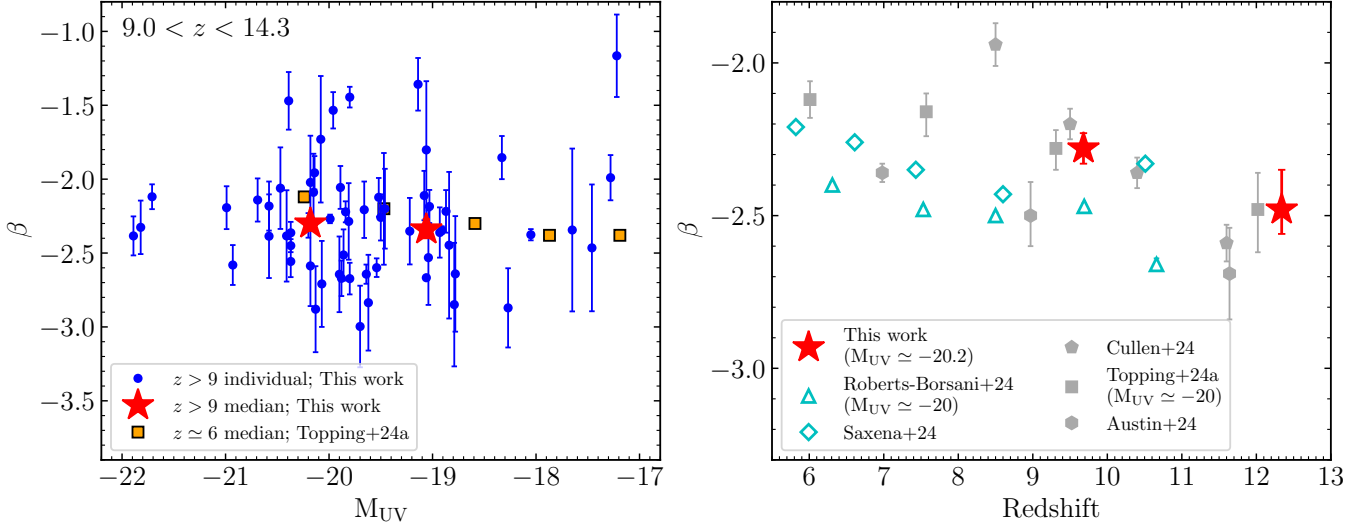


Figure 3. Left panel: M_{UV} vs. UV slope of galaxies in our $z > 9$ spectroscopic sample (blue circles). UV slopes are derived from NIRSpec prism spectra. The median UV slopes of galaxies with $M_{UV} < -19.8$ (median $M_{UV} < -20.2$) and $M_{UV} > -19.8$ (median $M_{UV} = -19.1$) are shown as red stars. As a comparison, we overplot the $\beta - M_{UV}$ relation at $z \simeq 6$ (Topping et al. 2024a) as orange squares. Right panel: Evolution of UV slopes at $6 \lesssim z \lesssim 14$. We show the median UV slopes of galaxies in our $z > 9$ spectroscopic sample as red stars. As a comparison, we overplot UV slopes of spectroscopic samples in the literature as open cyan symbols (diamonds: Saxena et al. 2024; triangles: Roberts-Borsani et al. 2024) and photometrically selected samples as solid grey symbols (pentagons: Cullen et al. 2024; squares: Topping et al. 2024a; hexagons: Austin et al. 2024).

grown in number, allowing the UV slopes to be measured with the NIRSpec prism. Saxena et al. (2024) presented an exploration of UV slopes in 295 spectra at $z > 5.5$ including 19 at $z > 9.5$. They found a trend toward bluer slopes at higher redshift over $5.5 < z < 9.5$. At $z > 9.5$, their results indicate that the UV slopes begin to plateau (or even redden), approaching the intrinsic value ($\beta = -2.6$) expected for stellar and nebular continuum.

We investigate the UV slopes in our spectroscopic sample of 60 galaxies at $z > 9$ (with 41 at $z > 9.5$, $2\times$ more than Saxena et al. 2024). In the left panel of Figure 3, we plot the UV slopes as a function of absolute UV magnitude. The $z > 9$ galaxies are generally blue, with a median UV slope of $\beta = -2.33^{+0.04}_{-0.04}$. We divide our sample into two bins of UV luminosity $M_{UV} < -19.8$ (median $M_{UV} = -20.2$) and $M_{UV} \geq -19.8$ (median $M_{UV} = -19.1$), with each group having a same number of systems (30 galaxies). We find a median UV slope of $\beta = -2.30^{+0.05}_{-0.05}$ in UV-luminous systems ($M_{UV} \simeq -20.2$). For fainter galaxies ($M_{UV} \simeq -19.1$), the median UV slope is similar to that of the more luminous systems with $\beta = -2.35^{+0.07}_{-0.06}$. The absence of a trend with UV slope and absolute magnitude is a departure from what is seen at lower redshifts in the literature, where the UV slopes tend to be bluer in less luminous galaxies (e.g., Cullen et al. 2023; Austin et al. 2024; Topping et al. 2024a). The photometric UV slopes at $z > 9$ also show

a shallow $\beta - M_{UV}$ relation at $M_{UV} < -19$ (see orange squares in Figure 3).

It is conceivable that the shallower relation between UV slope and absolute magnitude may reflect evolution in the nature of the most luminous galaxies at $z > 9$. For example, if UV bright galaxies become increasingly dominated by strong bursts at $z > 9$ (relative to lower redshifts), the most luminous systems will become weighted toward lower mass systems that have been up-scattered in luminosity. Since less massive galaxies tend to have less attenuation and bluer colors (e.g., Reddy et al. 2010; Finkelstein et al. 2012; McLure et al. 2018; Shapley et al. 2022; Morales et al. 2024), this effect would lead to a flatter slope in the $\beta - M_{UV}$ relation at $z > 9$. It is also possible that we are beginning to probe populations that have yet to build up grains that significantly redden the UV continuum (Narayanan et al. 2025) or that the dust that has been formed is ejected (Ferrara et al. 2025).

The UV slopes provide one of our only statistical probes of the nature of galaxies at $z \simeq 11 - 14$. Our database includes 14 sources at $z > 11$, which is $\sim 2\times$ larger than the spectroscopic samples used in previous prism-based UV slope studies (e.g., Saxena et al. 2024). Among these 14 sources, we find an average UV slope of $\beta = -2.37^{+0.05}_{-0.09}$. To quantify evolution in UV slopes at $9 < z < 14$, we consider only galaxies with $M_{UV} < -19.8$. At $z = 9 - 11$ we find a median value of $\beta = -2.28^{+0.05}_{-0.05}$, whereas at $z > 11$, we find $\beta = -2.48^{+0.13}_{-0.08}$, approaching the intrinsic value ex-

pected for galaxies without dust attenuation. Hence our results suggest that prism-based UV slopes may become bluer between $z \simeq 9$ and $z \simeq 14$ (right panel of Figure 3). The trend we find is consistent with that seen in most photometric studies (Austin et al. 2024; Cullen et al. 2024; Topping et al. 2024a). While we do not find clear evidence for the plateau or reddening found in Saxena et al. (2024), we note that our UV slopes at $z > 9$ are broadly consistent with the values reported in that paper. Nearly all studies (photometric and prism-based) indicate that average UV slopes approach the intrinsic value of stellar and nebular continuum at $z > 9$, likely suggesting minimal reddening from dust.

With a sample of 60 $z > 9$ galaxies, we can also explore the extremes of the UV color distribution. We may expect the reddest slopes to provide signposts of systems with dust attenuation caught during extended off-mode periods of star formation when intrinsic slopes redden (e.g., Narayanan et al. 2025) or extremely dense ionized gas that is ionized by hot stellar populations (Katz et al. 2024). We find 5 $z > 9$ galaxies with very red UV slopes ($\beta \gtrsim -1.5$). We note that 1 of the 5 red galaxies is GHZ9 ($\beta = -1.45$), a potential AGN at $z = 10.16$ with a plausible X-ray detection (Kovács et al. 2024; Napolitano et al. 2024). The reddest galaxy is JADES-GS-20064312 ($\beta = -1.17$), the faintest galaxy among the $z > 9$ sample ($M_{UV} = -17.2$). The spectrum of this source does not reveal H β or [O III] emission lines (Figure B1), with 3σ EW upper limits of 91 and 93 Å, respectively. This source appears to be a weak emission line galaxy in addition to having very red UV colors and intrinsically faint UV continuum, all properties that would be expected for a galaxy in a lull of star formation with some dust attenuation.

The $z > 9$ sample also has galaxies with extremely blue UV slopes. Galaxies with confident colors indicating $\beta < -2.8$ are difficult to explain unless the nebular continuum has been removed (e.g., Bouwens et al. 2010; Topping et al. 2022; Cullen et al. 2024). Such blue colors may imply leakage of ionizing photons or a recent downturn in star formation, both of which should reduce the nebular emission contribution to the SED (Topping et al. 2024a). There are 5 galaxies in our sample with $\beta \lesssim -2.8$ (GS-z13-LA, GS-z14-1, CAPERS-COSMOS-109917, JADES-GN-19715, JADES-GN-59720). JADES-GN-19715 is the bluest of the subset ($\beta = -3.00$) and has extremely weak rest-frame optical emission lines (H β EW is 60 Å and [O III] $\lambda 5007$ EW is 230 Å), as is seen in photometric sources with similarly blue sources (Topping et al. 2024a). To quantify the fraction of galaxies with $\beta < -2.8$ at $z > 9$, we follow the approach that Topping

et al. (2024a) developed for photometric samples, considering the subset of galaxies with small uncertainties in UV slopes ($\sigma_\beta < 0.3$). This leaves a total sample of 51 galaxies, including the 5 sources with $\beta < -2.8$. Extremely blue galaxies thus comprise $10^{+6}_{-4}\%$ of our $z > 9$ sample. We note that this fraction is about $3\times$ larger than that at $z \simeq 5 - 9$ (3.4%; Topping et al. 2024a), as may be expected if strong bursts or ionizing photon leakage is more common at $z > 9$.

3.2. C III] and O III] emission lines

C III] is the most commonly detected rest-frame UV emission line among the $z > 9$ galaxies. Of the 61 galaxies in our $z > 9$ sample, 60 have prism spectra covering C III]. In the left panel of Figure 4, we show the C III] EWs of these 60 galaxies as a function of M_{UV} (see Table B1 for measurements). We detect blended C III] $\lambda 1908$ emission with $S/N > 3$ in the prism spectra in 16 of these 60 galaxies. We measure C III] EWs spanning 7 – 41 Å for these 16 galaxies, with a median of 23 Å. C III] emission in 9 of the 16 objects have been reported previously (Bunker et al. 2023; Carniani et al. 2024; Castellano et al. 2024; Curti et al. 2025; D’Eugenio et al. 2024; Fujimoto et al. 2024; Napolitano et al. 2025), and our measurements indicate similar C III] EWs to those presented in literature.

We newly identify 7 galaxies at $z > 9$ with C III] detections with $S/N > 3$ (CAPERS-COSMOS-109917, CAPERS-EGS-25297, CAPERS-EGS-87132, CAPERS-UDS-22431, JADES-GN-55757, JADES-GS-20015720, JADES-GS-20088041; Figure B1). We further note lower S/N C III] emission lines ($S/N = 2 - 3$) in other 7 sources (Table B1). We consider these as tentative detections requiring deeper spectra for confirmation. We do not identify C III] in the prism spectra of the remaining 37 objects, enabling us to place 3σ upper limits on their C III] EWs. The median 3σ C III] EW upper limit of these 37 objects is 23 Å. We see in Figure 4 that many of the non-detections are in faint sources, where the EW limits are only conducive to detecting the most extreme line emission. At the bright end, we do measure several galaxies with upper limits implying EWs below 5 – 10 Å, indicating that a subset of the population at $z > 9$ does have at most moderate strength C III] emission.

C III] emission is detected ($S/N = 7$) in the composite spectrum of galaxies at $9.0 < z < 14.3$ in our sample (top panel of Figure 2), allowing us to infer the average C III] EW at $z > 9$. From the stack we derive an average C III] EW of 12.6 ± 1.8 Å, consistent with the average C III] EW ($12.8 - 13.7$ Å) measured from the composite spectrum of 30 galaxies at $z > 9$ in Roberts-Borsani et al. (2024). Such large C III] EWs are generally found

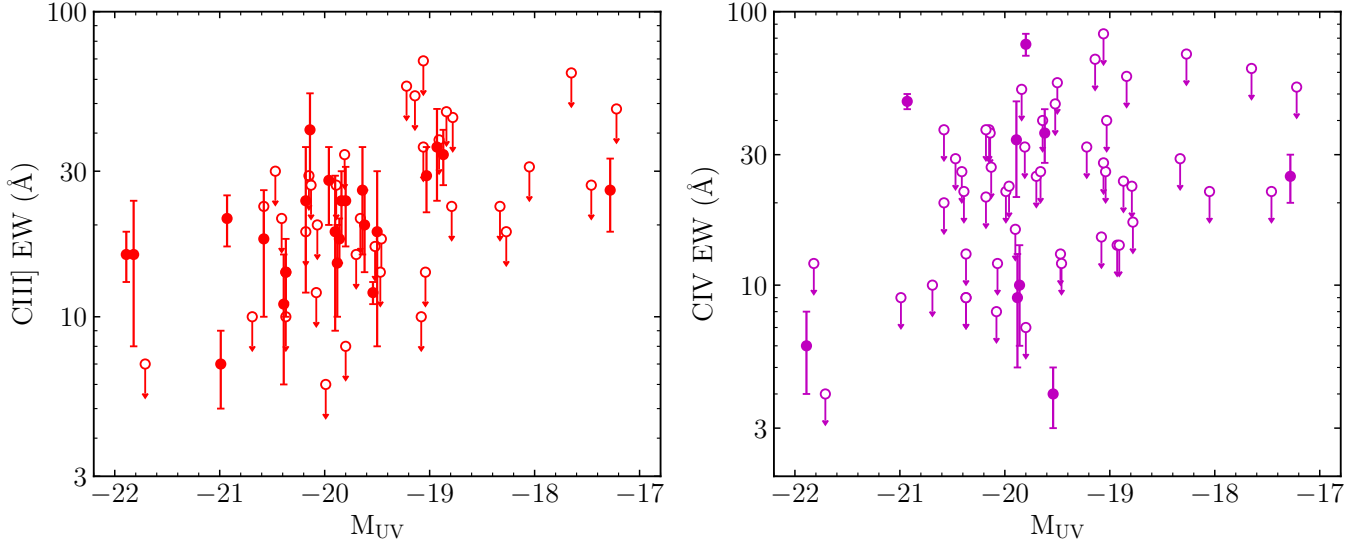


Figure 4. C III] (left) and C IV EWs (right) versus M_{UV} of galaxies in our $z > 9$ sample. We show detections as solid circles (red: C III]; magenta: C IV) and 3σ upper limits for non-detections as open circles.

in galaxies with moderately metal poor gas and large sSFRs, as we will show in Section 4.

Nineteen galaxies in our sample also have medium resolution grating spectra covering C III]. In three of the nineteen galaxies, C III] is detected in both grating and prism spectra (GN-z11, JADES-GS-55757, GS-z9-0). The C III] EWs measured from grating and prism spectra are consistent within 1σ uncertainties. Another two galaxies show C III] emission in the prism but not the grating (JADES-GS-20015720, GS-z14-0). The C III] EWs measured from the prism spectra of these two objects are within the 3σ EW upper limits evaluated from their grating spectra (see also Carniani et al. 2024).

If strong bursts become more common at $z > 9$, we should expect to see a larger fraction of the earliest galaxies with large sSFRs and extremely large C III] EWs ($> 20 \text{ \AA}$). These strong emission lines typically are thought to trace extremely young stellar populations (CSFH age $\lesssim 10 \text{ Myr}$) formed in recent upturns of star formation. To test this possibility, we characterize the incidence of galaxies with C III] EW $> 20 \text{ \AA}$ in our $z > 9$ sample. Here we focus on the subset with deep enough spectra to reach C III] EW limits of 20 \AA at 3σ . There are 33 such galaxies in our $z > 9$ sample, and 9 of them have C III] detections with EW $> 20 \text{ \AA}$ with $S/N > 3$. This results in a strong C III] emitter fraction of $9/33 = 27^{+10}_{-8}\%$ at $z > 9$ (uncertainties derived using the statistics for small numbers of events; Gehrels 1986). We will come back to discuss the evolution of the strong C III] emitter fraction in Section 5.2.

We also characterize the O III] $\lambda\lambda 1661, 1666$ doublet with the goal of investigating the carbon-to-oxygen (C/O) ratio of the ionized gas. At the resolution of the prism, O III] $\lambda\lambda 1661, 1666$ tends to be blended with He II $\lambda 1640$. We detect the O III] $\lambda\lambda 1661, 1666$ doublet with $S/N > 3$ in six individual galaxies (GS-z9-0, GN-z11, GS-z12-0, GHZ2, CAPERS-EGS-25297, CAPERS-EGS-87132). The O III] detections of four of these six galaxies have been presented previously (GN-z11, Bunker et al. 2023; GHZ2, Castellano et al. 2024; GS-z12-0, D’Eugenio et al. 2024; GS-z9-0, Curti et al. 2025). We measure He II+O III] EWs of $9 - 20 \text{ \AA}$ for these four galaxies, consistent with the values reported in the literature. We identify two new detections of the blended He II+O III] emission lines (CAPERS-EGS-25297, CAPERS-EGS-87132; Figure B1). We derive a He II+O III] EW of $20 \pm 6 \text{ \AA}$ for CAPERS-EGS-25297 and $20 \pm 5 \text{ \AA}$ for CAPERS-EGS-87132.

We also detect blended He II+O III] emission in the composite spectrum of the 61 galaxies at $9.0 < z < 14.3$ (top panel of Figure 2). The average He II+O III] EW measured from the composite is $4.3 \pm 1.3 \text{ \AA}$, which is smaller than those of individual detections. In Section 4.3, we will use the combination of O III] and C III] to constrain the C/O ratios in $z > 9$ galaxies.

3.3. C IV and He II emission lines

We search for emission lines from high ionization species C IV and He II in the spectra of $z > 9$ galaxies. These lines likely indicate the presence of hard radiation fields, powered by either low metallicity massive stars (e.g., Stark et al. 2015; Mainali et al. 2017) or AGNs (Nakajima et al. 2018). The C IV EWs of galaxies in our

$z > 9$ sample are shown in the right panel of Figure 4. We detect C IV $\lambda 1549$ emission with $S/N > 3$ in the prism spectra of 6 galaxies, with a median EW of 31 \AA (see Table B1). Five of the C IV detections have been reported previously in the literature (GN-z11, Bunker et al. 2023; GHZ2, Castellano et al. 2024; UNCOVER-22223, Fujimoto et al. 2024; GS-z9-0, Curti et al. 2025; GHZ9, Napolitano et al. 2025).

The new C IV detection is associated with CAPERS-COSMOS-109917 (Figure B1), with a measured EW of $36 \pm 8 \text{ \AA}$. We also note the presence of tentative C IV detections ($S/N = 2 - 3$) in three galaxies (JADES-GN-17858, JADES-GN-55757, JADES-GS-20015720; Figure B1). However, the vast majority of the galaxies in our sample (51 of 61 objects) do not show C IV emission lines. Most of the non-detections yield upper limits on C IV which can only rule out extremely strong line emission, with a median 3σ upper limit of 24 \AA . In the composite spectrum, we detect C IV emission with S/N of 4 (top panel of Figure 2). We measure an average C IV EW of $5.3 \pm 1.4 \text{ \AA}$ for the $z > 9$ galaxies from the stack.

To constrain how commonly $z > 9$ galaxies have hard radiation fields, we quantify the fraction of $z > 9$ galaxies with strong C IV emission. We consider galaxies with deep enough spectra to reach a C IV EW limit of 10 \AA at 3σ . We identify 13 such galaxies, with 4 showing strong C IV emission ($EW > 10 \text{ \AA}$) in their spectra. This indicates that the fraction of strong C IV emitters is $4/13 = 31^{+18}_{-14}\%$ at $z > 9$. We will investigate the evolution of this fraction in Section 5.3.

The detection of nebular He II $\lambda 1640$ emission (ionization potential = 54 eV) provides another probe of the presence of a hard ionizing spectrum. Since He II is blended with O III] in the prism spectra, we only quantify He II emission line strengths in the grating spectra of galaxies in our $z > 9$ sample. Among the 26 galaxies with grating spectra, we identify He II emission lines in two objects: GN-z11 and GS-z9-0. The He II emission lines of these two galaxies are relatively narrow ($FWHM = 250 - 330 \text{ km s}^{-1}$), consistent with a nebular (and not stellar) origin. We derive a He II EW of $5.7 \pm 1.8 \text{ \AA}$ for GN-z11 and $4.3 \pm 1.5 \text{ \AA}$ for GS-z9-0, comparable to the EWs reported for these two objects in literature (Bunker et al. 2023; Curti et al. 2025). For the remaining 24 galaxies without He II detection, we place a median 3σ upper limit on He II EW of 14 \AA . Future deep medium or high resolution grating spectroscopic observations are required to place more robust constraints on the He II emission in $z > 9$ galaxies.

3.4. N IV] and N III] emission lines

JWST/NIRSpec observations have begun revealing strong N IV] and N III] emission lines in a handful of $z > 5$ galaxies (e.g., Bunker et al. 2023; Castellano et al. 2024; Marques-Chaves et al. 2024; Topping et al. 2025a), suggesting nitrogen-enriched gas, potentially related to strong bursts of star formation (Topping et al. 2024b, 2025a) or in other cases AGN (e.g., Ji et al. 2024; Isobe et al. 2025). With our large $z > 9$ sample assembled from the public NIRSpec database, we look for N IV] or N III] emission lines in galaxies in the very early Universe. We identify blended N IV] $\lambda 1485$ detections ($S/N > 3$) in the prism spectra of 4 galaxies at $z > 9$ (GN-z9p4, GN-z11, UNCOVER-3686, GHZ2), which all have been reported previously (Bunker et al. 2023; Castellano et al. 2024; Fujimoto et al. 2024; Schaerer et al. 2024). The composite spectrum of galaxies at $9.0 < z < 14.3$ does show a N IV] detection with S/N of 4 (top panel of Figure 2). We measure an average N IV] EW of $5.0 \pm 1.2 \text{ \AA}$ at $z > 9$ from the stack. We note that non-detections of N IV] are only able to rule out the strongest line emission in most cases. The median 3σ N IV] EW upper limit is 24 \AA , well above the EW of the detected emission lines.

We recover the N III] $\lambda 1750$ emission in two galaxies in our sample, GN-z11 (Bunker et al. 2023) and GHZ2 (Castellano et al. 2024). We measure a N III] EW of $14 \pm 3 \text{ \AA}$ for GN-z11 and $13 \pm 4 \text{ \AA}$ for GHZ2, comparable to the EWs reported for these systems in the literature. The composite spectrum does not present an N III] emission feature, placing a 3σ upper limit $< 4.4 \text{ \AA}$ to the average N III] EW at $z > 9$.

With the constraints on nitrogen emission lines, we quantify the fraction of galaxies with N IV] emission linked to enhanced nitrogen and hard ionizing spectra at $z > 9$. Because the detected N IV] emission lines are relatively weak ($EW = 5 - 11 \text{ \AA}$), we only consider galaxies with N IV] EW limits that reach to 5 \AA at 3σ . There are only 6 such galaxies in our $z > 9$ sample. Although the current statistics are poor, four of these six galaxies present N IV] emission, indicating a very large N IV] emitter fraction of $67^{+21}_{-28}\%$ at $z > 9$.

3.5. $H\beta$, $H\gamma$, and Balmer Decrements

The hydrogen Balmer emission lines provide constraints on the light-weighted stellar population ages (via $H\beta$ EWs) and the dust attenuation of the H II regions (via the Balmer decrements). The NIRSpec spectra allow us to measure $H\beta$ and $H\gamma$ emission lines in galaxies at redshifts up to $z \simeq 9.8$ and $z \simeq 11.1$, respectively.

Among the 61 galaxies in our $z > 9$ sample, 29 are at $9.0 < z < 9.8$ with NIRSpec spectra covering the

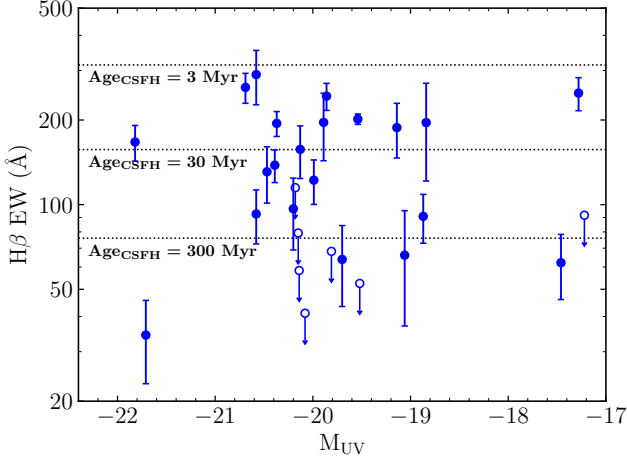


Figure 5. $H\beta$ EW versus M_{UV} of galaxies in our $z > 9$ sample. We show detections as blue solid circles and 3σ upper limits for non-detections as open circles. The dotted lines show the corresponding CSFH ages for $H\beta$ EWs. The CSFH ages are derived from BEAGLE models assuming the Chabrier (2003) IMF with stellar masses in the range $0.1 - 300 M_{\odot}$, an ionization parameter $\log U = -2.5$, and a metallicity $Z = 0.1 Z_{\odot}$ (see Section 2.6).

observed wavelength of $H\beta$. We identify $H\beta$ emission lines in the spectra of 20 galaxies (see Figure 5). The $H\beta$ EWs span a wide range, with 16th-50th-84th percentiles of 91 Å, 162 Å, and 242 Å, respectively. For context, stellar population ages of 3, 30, and 300 Myr correspond to $H\beta$ EWs of 300, 160, and 80 Å, respectively, assuming constant star formation history in the stellar population models described in Section 2.6 (Figure 5). It is clear that a large fraction of the population appears to have very large $H\beta$ EWs, as might be expected in galaxies caught in strong bursts. However, there are also non-detections indicating very weak $H\beta$ (< 75 Å), perhaps pointing to systems in a lull following a recent downturn in star formation.

We also find a large dispersion in the $H\gamma$ EW distribution. There are 49 galaxies at $9.0 < z < 11.1$ with $H\gamma$ constraints, of which 18 show detections. The $H\gamma$ EWs are described by a distribution with 16th-50th-84th percentiles of 39 Å, 73 Å, and 125 Å. The average values of the $H\beta$ and $H\gamma$ distributions are consistent with the $9.0 < z < 9.6$ composite (bottom panel of Figure 2) which reveals $H\beta$ EW of 150 ± 12 Å and $H\gamma$ EW of 51 ± 7 Å, similar to the EWs reported in Roberts-Borsani et al. (2024). We will discuss the star formation histories implied by the spectra in Section 4.1.

We quantify the fraction of galaxies with extremely large $H\beta$ or $H\gamma$ EWs. At $9.0 < z < 9.8$, we consider systems with $H\beta$ EWs > 240 Å, which the EWs are associated with very young stellar populations (CSFH

age $\lesssim 5$ Myr). At higher redshifts where $H\gamma$ is visible ($9.8 < z < 11.1$), we adopt an equivalent threshold of $H\gamma$ EW greater than 80 Å. There are 40 galaxies in our $z > 9$ sample with deep enough spectra to reach $H\beta$ EW limit of 240 Å or $H\gamma$ EW limit of 80 Å at 3σ . Nine of these forty galaxies present $H\beta$ EW > 240 Å at $9.0 < z < 9.8$ or $H\gamma$ EW > 80 Å at $9.8 < z < 11.1$, indicating a strong Balmer line emitter fraction of $23^{+8}_{-7}\%$. We will investigate the evolution of this fraction in Section 5.1.

The $H\gamma$ to $H\beta$ emission line ratios constrain the dust attenuation. There are 12 galaxies in our sample with both $H\gamma$ and $H\beta$ emission detections. We derive $H\gamma/H\beta$ ratios spanning between 0.436 ± 0.087 and 0.618 ± 0.204 . Systems with $H\gamma$ non-detections are also consistent with this range. Assuming the electron temperature that we infer from the composite spectrum in Section 3.6 ($T_e = 2.1 \times 10^4$ K), the intrinsic $H\gamma/H\beta$ ratio expected from case B recombination is 0.474 (Osterbrock & Ferland 2006). We thus find that the $H\gamma/H\beta$ ratios are typically consistent with the case B value within uncertainties. Assuming the Cardelli et al. (1989) extinction curve, the lowest $H\gamma/H\beta$ ratio (0.436 ± 0.087) suggests an $E(B - V)$ of $0.16^{+0.28}_{-0.16}$. The composite spectrum reveals an average $H\gamma/H\beta$ ratio (0.460 ± 0.071) that also indicates a fairly small value of reddening, $E(B - V)$ of $0.06^{+0.20}_{-0.06}$. Based on the Balmer line ratios, we find that $z > 9$ galaxies have little attenuation toward their H II regions, consistent with the conclusions based on the UV continuum slopes.

A subset of the $z > 9$ galaxies in our sample have relatively red UV slopes (Section 3.1), potentially indicating a combination of dust attenuation or redder intrinsic UV slopes. We find that these systems have the lowest $H\gamma/H\beta$ ratios, potentially indicating moderate (but still relatively low) level of reddening. For example, RUBIES-EGS-929993 has $\beta = -1.36$, and its $H\gamma/H\beta$ ratio (< 0.44) suggests an $E(B - V)$ of > 0.1 . JADES-GS-20077159 has $\beta = -1.47$ with $H\gamma/H\beta = 0.436 \pm 0.087$, indicating an $E(B - V)$ of $0.16^{+0.28}_{-0.16}$. The reddest object (JADES-GS-20064312) does not have $H\gamma$ or $H\beta$ detections. Deeper spectra are required to better quantify the Balmer decrements of the red systems, as uncertainties currently prevent confident statements on the nebular attenuation.

3.6. $[O II]$, $[Ne III]$, and $[O III]$ emission lines

Rest-frame optical emission lines (e.g., $[O II]$, $[Ne III]$, $[O III]$) provide useful insights into the properties of ionized gas. At $z > 9$, we are able to access some of the optical lines with NIRSspec in certain redshift windows (e.g., $[O II]$ and $[Ne III]$ at $z \lesssim 12.6$, $[O III] \lambda 5007$ at $z \lesssim 9.6$). We characterize the available rest-frame opti-

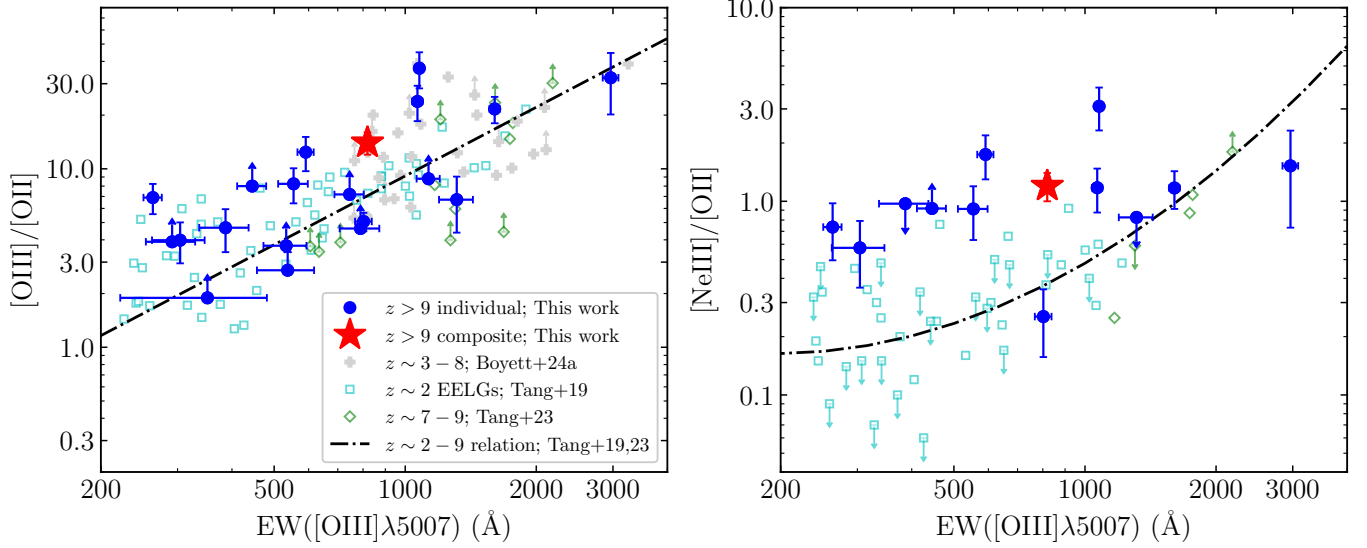


Figure 6. Ionization-sensitive line ratios ($[\text{O III}]/[\text{O II}]$, left; $[\text{Ne III}]/[\text{O II}]$, right) versus $[\text{O III}] \lambda 5007$ EW for $z > 9$ galaxies (blue circles). Measurements from the composite spectrum of galaxies at $9.0 < z < 9.6$ are shown by red stars. For comparison, we overplot the data at $z \sim 2 - 9$ in literature, including extreme emission line galaxies (EELGs) at $z \sim 2$ (Tang et al. 2019; cyan open squares), *JWST* measurements at $z \sim 7 - 9$ (Tang et al. 2023; green open diamonds) and at $z \sim 3 - 8$ (Boyett et al. 2024a; grey cross). We also show the relationships between line ratios and $[\text{O III}]$ EW derived from $z \sim 2 - 9$ dataset (Tang et al. 2019, 2023) as black lines.

cal emission lines in the spectra of galaxies in our $z > 9$ sample, and we use these measurements to explore the gas conditions and ionizing spectra of $z > 9$ systems.

$[\text{O III}] \lambda 5007$ is the most luminous emission line in the rest-frame optical. We identify $[\text{O III}] \lambda 5007$ detections in 20 of the 22 galaxies at $9.0 < z < 9.6$ that have coverage of $[\text{O III}]$. Similar to the $\text{H}\beta$ and $\text{H}\gamma$ EWs, the $[\text{O III}] \lambda 5007$ EWs of these 20 galaxies span a wide range, with 16th-50th-84th percentiles of 301, 745, and 1395 Å, respectively. From the composite spectrum of the 22 galaxies at $9.0 < z < 9.6$ in our sample (bottom panel of Figure 2), we derive an average $[\text{O III}] \lambda 5007$ EW of 819 ± 13 Å, broadly consistent with the median $[\text{O III}] \lambda 5007$ EW measured from individual detections. The large dispersion in $[\text{O III}]$ EWs may point to a range of star formation histories and gas conditions. We will discuss this further in Section 4.

Ionization-sensitive emission line ratios ($[\text{O III}]/[\text{O II}]$, hereafter O32, and $[\text{Ne III}]/[\text{O II}]$, hereafter Ne3O2) have been found to scale with rest-frame optical emission line EWs in star-forming galaxies over cosmic time ($z \sim 0 - 9$; e.g., Tang et al. 2019, 2023; Sanders et al. 2020; Boyett et al. 2024a). This may reflect a variety of physical effects (i.e., ionization parameter, metallicity, density) that correlate with the emission line EWs. Here we investigate whether the $z > 9$ sample follows similar trends. We compute the O32 and Ne3O2 ratios of galaxies with measurements on $[\text{O II}]$, $[\text{Ne III}]$, and $[\text{O III}]$, investigating the ionization state of the ISM in

these systems. To determine the sample average, we will also consider the composite spectrum and systems where we can only place limits on the line ratios.

We detect $[\text{O II}] \lambda 3728$ emission in the spectra of 26 galaxies and $[\text{Ne III}] \lambda 3869$ emission in 19 galaxies at $9.0 < z < 12.6$. When computing O32 ratios (and limits on O32), we correct for dust using the $E(B - V)$ inferred from $\text{H}\gamma/\text{H}\beta$ ratios and assuming the Cardelli et al. (1989) extinction curve. For those without $\text{H}\gamma/\text{H}\beta$ measurements, we use $E(B - V) = 0.06$ inferred from the average $\text{H}\gamma/\text{H}\beta$ ratio (Section 3.5). In Figure 6, we show O32 (left panel) and Ne3O2 vs. $[\text{O III}] \lambda 5007$ EW (right panel) for $z > 9$ galaxies (blue circles). For comparison, we also show the correlations between ionization-sensitive line ratios and $[\text{O III}]$ EW that have been found at lower redshift (black dashed lines).

There are two key points to take away from the O32 and Ne3O2 data. First, we find that $z > 9$ galaxies with larger $[\text{O III}]$ EWs tend to have larger O32 and Ne3O2 ratios, similar to the general trend seen at lower redshift. Second, many of the $z > 9$ galaxies have O32 and Ne3O2 ratios above the ionization vs. $[\text{O III}]$ EW sequence derived at lower redshift. This may suggest that $z > 9$ galaxies have even more extreme ionization conditions in their ISM comparing to galaxies at lower redshifts with similar $[\text{O III}]$ EWs. Additionally, if the ionized gas densities are very high in these systems (e.g., $\gtrsim 10^4 \text{ cm}^{-3}$, above the critical densities of the $^2\text{D}^0$ level of the O II ion), the low-ionization $[\text{O II}]$ lines will be suppressed by

collisional de-excitation, increasing the O32 and Ne3O2 ratios. Collisional de-excitation of [O II] has been shown to be important in the strongest bursts (e.g., [Topping et al. 2024b](#)). If very high gas densities are also seen in more typical $z > 9$ sources (i.e., not just the highest [O III] EWs), we may expect to see elevated O32 and Ne3O2 ratios.

The picture is similar when considering the composite spectrum. In the stack of the 22 galaxies at $9.0 < z < 9.6$ (bottom panel of Figure 2), we derive a large average O32 ratio of 13.4 ± 1.7 . This is about $3\text{--}10\times$ larger than the typical O32 seen at $z \simeq 1\text{--}5$ ($\text{O32} \simeq 1\text{--}5$; e.g., [Steidel et al. 2016](#); [Sanders et al. 2016](#); [Shapley et al. 2023](#)), consistent with line ratios expected for a highly ionized ISM. We also derive a large average Ne3O2 ratio (0.88 ± 0.15) from the stack. Both the O32 and Ne3O2 ratios are above the ionization – EW sequence derived at lower redshift (see red stars in Figure 6), consistent with the picture revealed by individual systems in our sample.

3.7. [O III] $\lambda 4363$ emission line

The [O III] $\lambda 4363$ auroral emission line provides the potential for constraints on the electron temperature and the gas-phase oxygen abundance. There are three galaxies with [O III] $\lambda 4363$ detections, with two previously reported in the literature, GS-z9-0 ([Curti et al. 2025](#)) and GN-z9p4 ([Schaerer et al. 2024](#)). We newly-identify [O III] $\lambda 4363$ in CAPERS-EGS-25297 (Figure B1). We find large [O III] $\lambda 4363/\text{H}\gamma$ ratios ($0.33\text{--}0.44$) for these three objects comparing to other $z = 2\text{--}9$ systems with [O III] $\lambda 4363$ detections (e.g., [Nakajima et al. 2023](#); [Sanders et al. 2024](#)), suggesting high electron temperatures in the ISM. We also identify [O III] $\lambda 4363$ auroral line in the composite spectrum of the $9.0 < z < 9.6$ galaxies in our sample (bottom panel of Figure 2), allowing us to estimate the average temperature and oxygen abundance of $z > 9$ galaxies. The [O III] $\lambda 4363/\text{H}\gamma$ ratio measured from the composite is relatively large of 0.42 ± 0.12 . We will use these measurements to calculate the temperature and oxygen abundance of the H II regions in $z > 9$ galaxies in Section 4.2.

4. PHYSICAL PROPERTIES AT $z > 9$

Using the emission line measurements and SEDs of $z > 9$ galaxies in our sample, we characterize the stellar masses and SFHs (Section 4.1), the gas-phase oxygen abundances (Section 4.2), the carbon-to-oxygen ratios (Section 4.3), and the nitrogen-to-oxygen ratios (Section 4.4).

4.1. Stellar masses and star formation histories

We first characterize the stellar populations (stellar masses, SFRs, sSFRs) of the $z > 9$ galaxies in our sample. Because the rest-frame optical continuum is essential for constraining the stellar mass, we focus on the subset of 45 galaxies at $9.0 < z < 10.8$. At these redshifts, there is at least one NIRCcam filter that covers the continuum redward the Balmer break. While line contamination is still a source of error, the emission lines in the rest-frame optical filters at these redshifts tend to be relatively weaker features ([O II], [Ne III]). Our goal in this section is to investigate the stellar masses (and associated uncertainties) and constrain the recent star formation histories. We close by comparing the gas-phase properties implied by the photoionization model fits to those derived from the emission line ratios described above.

We describe our fitting methodology and assumptions in Section 2.6. To summarize, we use the BEAGLE tool to fit both the NIRCcam SED and (if available) the C III], $\text{H}\gamma$, $\text{H}\beta$, and [O III] $\lambda 5007$ EWs. Our default models consider a two component SFH (TcSFH), consisting of an exponentially delayed component and a recent ($1\text{--}20$ Myr) constant star formation component, following the approach introduced in [Endsley et al. \(2024b\)](#). The TcSFH model enables flexibility in fitting the recent star formation history, allowing bursts or lulls of star formation in the few Myr before observation. Below we will briefly discuss the impact of using several different star formation histories on the inference of stellar mass.

Our results reveal that the $z > 9$ stellar masses inferred from the TcSFH models are all relatively low (left panel of Figure 7, shown as a function of M_{UV}), with 16th-50th-84th percentiles of $1.0 \times 10^8 M_{\odot}$, $3.0 \times 10^8 M_{\odot}$, and $5.2 \times 10^8 M_{\odot}$, respectively. The stellar masses are at most $\simeq 10^9 M_{\odot}$. For the subset of systems with stellar masses reported in literature ([Arrabal Haro et al. 2023a](#); [Castellano et al. 2023](#); [Curtis-Lake et al. 2023](#); [Tacchella et al. 2023a](#); [Curti et al. 2025](#); [Kokorev et al. 2025](#)), we compare these values with the stellar masses derived from BEAGLE TcSFH models. We find good agreement between the two, with differences less than 0.3 dex.

Outshining can play a significant role in driving uncertainties in the stellar masses (e.g., [Roberts-Borsani et al. 2020](#); [Laporte et al. 2021](#); [Tang et al. 2022](#); [Tacchella et al. 2023b](#); [Whitler et al. 2023b](#)). However, we find this effect is not as pronounced at $z > 9$, given the limited cosmic time prior to the redshift of observation. In addition to the TcSFH models, we consider Prospector non-parametric SFH models with a continuity prior that allows a significant older component (see Section 2.6). We also fit galaxies with CSFH models using the BEAGLE tool. In general, we find that the

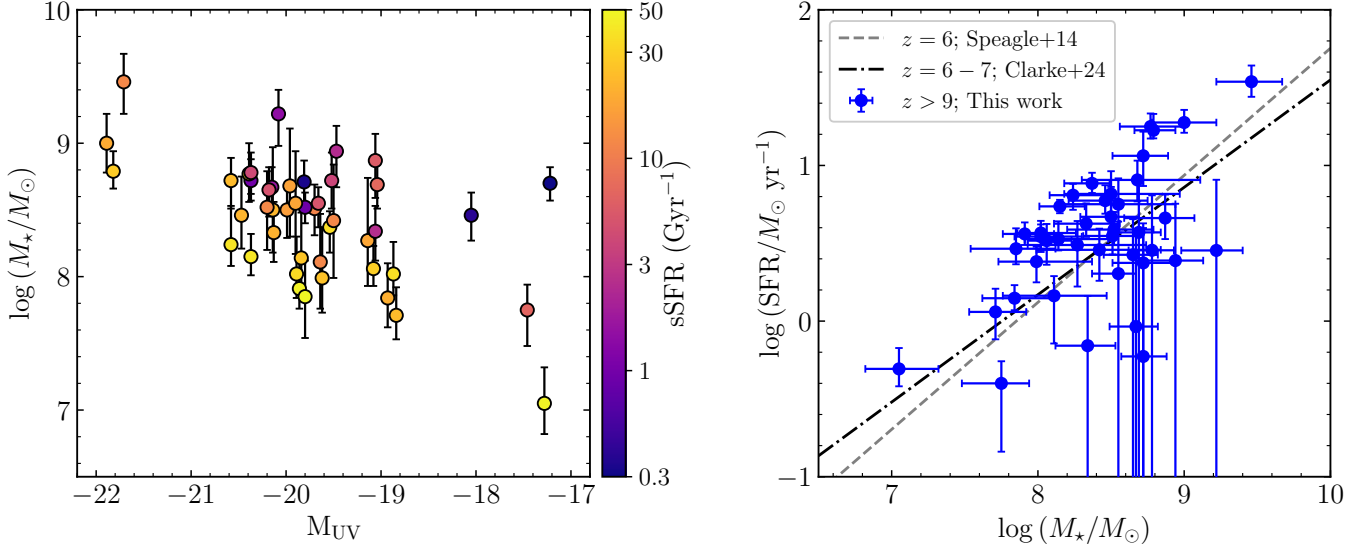


Figure 7. Left panel: Stellar mass versus M_{UV} for galaxies at $9.0 < z < 10.8$ in our sample. The stellar masses are derived from BEAGLE models assuming a two component SFH (Section 2.6). Colors show the sSFRs (averaged over the most recent 10 Myr) derived from BEAGLE. Right panel: SFR (averaged over the most recent 10 Myr) versus M_* for galaxies at $9.0 < z < 10.8$ (blue circles). For comparison, we overplot the star forming main sequence derived from *JWST* observations in Clarke et al. (2024) at $z = 6 - 7$ (black dash-dotted line) and derived by Speagle et al. (2014) computed at $z = 6$ (grey dashed line).

TcSFH and Prospector continuity models give similar stellar masses for our sample, as expected since both setups allow an older stellar component on top of a recent burst of star formation. The stellar masses inferred from CSFH models tend to be modestly smaller ($\simeq 1.5\times$) than those from TcSFH. For the strongest $H\beta$ line emitters ($\text{EW} > 240 \text{ \AA}$), the variation is at most a factor of two. This is a departure from $z \simeq 7$, where outshining in young systems could create order of magnitude differences in stellar masses with varying treatments of the SFH (e.g., Whitler et al. 2023b). We will adopt the TcSFH masses in our analysis that follows, but we note that a small uncertainty will be present in the stellar masses of the largest $H\beta$ line emitters.

In the right panel of Figure 7, we show the SFRs of our $z > 9$ sample as a function of stellar mass (i.e., star forming main sequence, SFMS). We define the SFR as that averaged over the most recent 10 Myr and use the values derived from the TcSFH models. The SFRs scale with stellar mass, with 16th-50th-84th percentiles of 1.4 , 3.5 , and $7.2 \times 10^8 M_\odot \text{ yr}^{-1}$. We compare the SFMS at $z > 9$ with that derived at $z = 6 - 7$ (Speagle et al. 2014; Clarke et al. 2024) in the right panel of Figure 7, which is derived by fitting SEDs assuming a delayed- τ SFH that is similar to our SFH assumption (Section 2.6). We find that the SFRs of $z > 9$ galaxies are on average $1.5\times$ higher than that at $z = 6 - 7$ at fixed stellar mass. A detailed comparison of evolution in the SFMS would require careful modeling of mass incompleteness at $z \gtrsim 9$, which is beyond the scope of

this current analysis. However, we note that there is clearly a shift toward larger SFR at fixed stellar mass, as expected based on the evolution of baryon accretion rates with redshift (Neistein & Dekel 2008; Dekel et al. 2009; McBride et al. 2009).

The sSFRs constrain the recent SFH in $z > 9$ galaxies. Here we define the sSFR as that averaged over the 10 Myr prior to the redshift of observation, and we use the values derived from the TcSFH models. The sSFR is constrained by both the emission line EWs and the shape of the NIRCcam SED. We find that sSFRs of the $z > 9$ galaxies tend to be large, with the distribution having 16th-50th-84th percentiles of 2.5 Gyr^{-1} , 14 Gyr^{-1} , and 34 Gyr^{-1} , respectively (left panel of Figure 7). The middle and upper-end of the distribution suggest recent upturns in star formation, whereas the lowest sSFRs correspond to galaxies that have likely experienced a recent lull or downturn in star formation (as discussed below).

To better quantify the recent SFHs at $z > 9$, we calculate the ratio between the SFR averaged over the most recent 3 Myr ($\text{SFR}_{3\text{Myr}}$) and that over the past 3–50 Myr ($\text{SFR}_{3-50\text{Myr}}$) for each galaxy at $z > 9$. This ratio provides a more direct measure of whether the SFH has recently risen or declined (e.g., Endsley et al. 2024a; Kokorev et al. 2025). We find that galaxies with the strongest emission lines ($H\beta \text{ EW} > 240 \text{ \AA}$ or $\text{C III] EW} > 20 \text{ \AA}$) have the largest $\text{SFR}_{3\text{Myr}}/\text{SFR}_{3-50\text{Myr}}$ ratios of > 4 (up to $\simeq 15$) inferred from TcSFH models. In these cases, the SED needs to be dominated by a young stellar

population to reproduce the optical emission line EWs and continuum SED. Among the 61 galaxies at $z > 9$, 14 have $\text{SFR}_{3\text{Myr}}/\text{SFR}_{3-50\text{Myr}}$ ratio larger than 4 (> 2 at 84% confidence interval). This suggests that 23% of our $z > 9$ galaxies may have recently experienced strong upturns in their SFHs.

We also expect sources to be in an off-mode if star formation is very bursty at $z > 9$. In these galaxies, we expect weaker emission lines, as O stars disappear from the stellar population. At lower redshifts, modest rest-frame optical emission line EWs are common and easily explained by constant star formation histories extending for several 100 Myr. However, at $z > 9$ the age of the universe ($\lesssim 500$ Myr) is not sufficient to facilitate lower rest-frame optical emission lines if star formation is constant. As we showed in Section 3.5, the CSFH BEAGLE models require stellar population ages of $\gtrsim 500$ Myr to produce $\text{H}\beta$ EWs with $< 75 \text{ \AA}$. As a result, we find that the sources in our sample with comparably weak rest-frame optical lines tend to be significantly better fit with SFHs having recent SFR downturns, facilitating the diminished emission line strengths.

Indeed, we find 8 systems in our $z > 9$ sample with weak (or undetected) $\text{H}\beta$ emission lines ($\text{EW} < 75 \text{ \AA}$). According to the TcSFH models, these sources have low $\text{SFR}_{3\text{Myr}}/\text{SFR}_{3-50\text{Myr}}$ ratios (< 0.2), indicating significant recent downturns in star formation. At $z \simeq 6 - 8$, it has been shown that such systems tend to be found at the faint end of the UV luminosity function (e.g., Endsley et al. 2024b; Begley et al. 2025). While statistics remain poor at $z > 9$, we also find that low inferred $\text{SFR}_{3\text{Myr}}/\text{SFR}_{3-50\text{Myr}}$ ratios are frequently found in faint galaxies. For the seven systems with $M_{\text{UV}} > -18.5$ in our sample, four (57%) have inferred $\text{SFR}_{3\text{Myr}}/\text{SFR}_{3-50\text{Myr}}$ ratios below 0.2 (see low sSFR galaxies at faintest magnitudes in the left panel of Figure 7). On the other hand, this fraction decreases dramatically to 9% for galaxies with $M_{\text{UV}} < -18.5$. These results may suggest that at $z > 9$, strong recent downturns in SFR become more common in galaxies with the lowest UV luminosities, as may be expected if the brightest systems tend to be bright in part because they have experienced a recent burst (see also Gelli et al. 2025). We will discuss the implications of our inferred SFHs for the nature of stellar populations at $z > 9$ further in Section 6.1.

4.2. Gas-phase oxygen abundances

We are able to constrain gas-phase metallicities using the rest-frame optical line ratios reported in Section 3. The $[\text{O III}] \lambda 4363$ detection in the composite spectrum enables inference of the direct method metallicity. As-

suming an electron density ($n_e \simeq 2 \times 10^4 \text{ cm}^{-3}$) that is typical of the high-ionization zones of $z > 9$ galaxies (derived using $[\text{C III}] \lambda 1907/\text{C III}] \lambda 1909$ flux ratios in Topping et al. 2025b), we infer an electron temperature $T_e(\text{O III})$ of $2.1^{+0.3}_{-0.4} \times 10^4 \text{ K}$ for the O^{++} zone using the PYTHON package PyNeb (Luridiana et al. 2015) to reproduce the observed line ratios in the composite. We next derive the O^+ zone electron temperature $T_e(\text{O II})$. Because the $[\text{O II}] \lambda\lambda 7320, 7330$ auroral lines are not covered by the NIRSpec spectra at $z > 9$, we apply the relation $T_e(\text{O II}) = 0.7 \times T_e(\text{O III}) + 3000 \text{ K}$ (Campbell et al. 1986; Garnett 1992). Using the measured $[\text{O III}] \lambda 5007/\text{H}\beta$ and $[\text{O III}] \lambda 3728/\text{H}\beta$ ratios, we infer an average gas-phase oxygen abundance $12 + \log(\text{O}/\text{H}) = 7.59^{+0.14}_{-0.16}$ ($0.08^{+0.03}_{-0.03} Z_\odot$, where solar metallicity corresponds to $12 + \log(\text{O}/\text{H}) = 8.71$; Gutkin et al. 2016). This indicates moderately metal poor gas is common in the $z > 9$ galaxies.

We also characterize the gas-phase metallicity via strong line ratios: $[\text{O III}] \lambda 5007/\text{H}\beta$ (O3) and $([\text{O III}] + [\text{O II}])/\text{H}\beta$ (R23) ratios. For 17 galaxies with both $\text{H}\beta$ and $[\text{O III}] \lambda 5007$ detections in the NIRSpec spectra, we measure O3 ratios ranging from 3.1 to 10.2, with a median value of 5.0. This is consistent with the composite which shows an average O3 of 5.2 ± 0.4 . Using the relationship between O3 and oxygen abundance derived from $z \simeq 2 - 9$ galaxies in Sanders et al. (2024), we infer an average oxygen abundance $12 + \log(\text{O}/\text{H}) = 7.41^{+0.08}_{-0.08}$ ($0.05^{+0.01}_{-0.01} Z_\odot$) given the composite O3 ratio. The R23 ratios suggest a similar picture. We derive the average dust-corrected R23 ratio of 7.5 ± 0.6 from the composite spectrum. Using the R23 – O/H relation in Sanders et al. (2024), we infer $12 + \log(\text{O}/\text{H}) = 7.39^{+0.08}_{-0.08}$, consistent with the oxygen abundance inferred from O3. Both measurements are similar to those reported in Roberts-Borsani et al. (2024) and also comparable to the direct method metallicity derived above.

The BEAGLE photoionization models also constrain the metallicity through fits to rest-frame optical emission lines. In particular, for the composite spectrum at $9.0 < z < 9.8$, we fit the $[\text{O II}] \lambda 3728$, $[\text{Ne III}] \lambda 3869$, $\text{H}\gamma$, $[\text{O III}] \lambda 4363$, $\text{H}\beta$, $[\text{O III}] \lambda 4959$, and $[\text{O III}] \lambda 5007$ emission line fluxes as well as $\text{H}\gamma$ and $\text{H}\beta$ EWs. The flux ratios and EWs are well-reproduced by BEAGLE models. The elevated O32 and Ne3O2 ratios at $z > 9$ are fit by a large ionization parameter of $\log U = -2.11^{+0.08}_{-0.07}$. The best-fit metallicity inferred by BEAGLE models is $0.11^{+0.02}_{-0.02} Z_\odot$, corresponding to a gas-phase oxygen abundance $12 + \log(\text{O}/\text{H}) = 7.76^{+0.05}_{-0.05}$. This value is slightly larger than that inferred from the direct method and the O3 and R23 ratios. We note that the

observed [O III] $\lambda 4363$ flux is slightly underpredicted in the best-fitting models (in spite of the strong lines being well-fit), likely contributing to the higher-implied metallicity. Slight offsets between metallicities inferred via the direct method and photoionization models are common, potentially reflecting temperature (or other property) variations in the ionized gas that are not captured in the models. Nevertheless, the key result remains that the average gas-phase oxygen abundance in spectroscopic samples at $z > 9$ appears to be moderately low, of order 0.05 to 0.11 Z_{\odot} (Table 2).

4.3. Carbon-to-oxygen ratios

At the low metallicities of our galaxies, we expect the gas-phase C/O ratios to be sub-solar, assuming that the C/O – O/H trends seen in local and lower redshift galaxies (e.g., Garnett et al. 1995; Berg et al. 2016, 2019; Steidel et al. 2016) hold at $z > 9$. However, if the primary or pseudo-secondary production mechanisms of carbon are different in $z > 9$ galaxies, we may expect to see variations in the C/O ratios. In particular, at extremely low metallicities probed by halo stars and damped Ly α absorbers (DLAs), observations have indicated that C/O ratios begin to increase, reaching close to the solar value (e.g., Cooke et al. 2011). This effect is thought to be related to the yields of the first generation(s) of massive stars. *JWST* spectroscopy offers the potential to test if a similar C/O ‘excess’ is seen in the lowest metallicity galaxies at very high redshift. In this subsection, we will summarize what is known about C/O ratios at $z > 9$ given current constraints on the rest-frame UV spectra of the 61 galaxies in our sample.

We first consider the composite spectrum of galaxies at $9.0 < z < 14.3$. The stack shows both C III] and O III] (the latter blended with He II), allowing us to constrain the average C/O ratio. To do so, we first compute the C^{++}/O^{++} ratio using the C III]/O III] flux ratio with PyNeb. Here we assume an electron density for highly-ionized gas $n_e = 2 \times 10^4 \text{ cm}^{-3}$ (Topping et al. 2025b) and an electron temperature $T_e = 2.1 \times 10^4 \text{ K}$ inferred from [O III] $\lambda 4363$ detection (Section 4.2). Because of the low spectral resolution ($R \sim 100$), it is difficult to deblend O III] and He II. To estimate the strength of O III], we assume a He II/O III] flux ratio of 0.25, which is the typical value inferred from $z > 4$ galaxies with He II or O III] detections in the grating spectra (Bunker et al. 2023; Jones et al. 2023; Cameron et al. 2024; Marques-Chaves et al. 2024; Topping et al. 2024b, 2025a; Curti et al. 2025). This results in a C III]/O III] ratio of 2.5 ± 0.8 and hence $C^{++}/O^{++} = 0.23 \pm 0.07$. Finally, we convert the C^{++}/O^{++} ratio to C/O ratio by applying an ionization correction factor (ICF). This step accounts for the frac-

tion of carbon that is triply ionized while oxygen is still primarily doubly ionized due to the higher ionization potential of O^{++} (55 eV) than C^{++} (48 eV). To estimate the ICF, we use the [O III] $\lambda\lambda 4959, 5007$ /[O II] $\lambda 3728$ ratio (Section 3.6) and convert it to the ionization parameter ($\log U = -2.06$) and ICF (1.05) using the relations in Berg et al. (2019). This gives a value of $\log(C/O) = -0.62 \pm 0.15$ ($0.44 \pm 0.14 \text{ C/O}_{\odot}$; left panel of Figure 8 and Table 2). We note that the solar abundance ratio is $\log(C/O) = -0.26$ from Asplund et al. 2009. Thus, based on the composite spectrum, we conclude that typical $z > 9$ galaxies have sub-solar C/O ratios.

However, it is conceivable that we may find individual examples of $z > 9$ galaxies with elevated C/O ratios. Using the methods described above, we infer the C/O ratios for the six galaxies with O III] and C III] detections. Our assumptions vary depending on the spectra, so we explain our methods for each source below. We note that the C/O ratios of several of these sources have been discussed in the literature previously (Cameron et al. 2023a; Castellano et al. 2024; D’Eugenio et al. 2024; Curti et al. 2025). But to ensure a self-consistent database, we re-derive the C/O ratios with our spectral reductions, even if previous measurements exist.

One of the first steps is characterizing the electron temperature. In the case of two galaxies (GS-z9-0 and CAPERS-EGS-25297), we see [O II], [O III] $\lambda 4363$, and [O III] $\lambda 5007$ detections. For these two sources, we derive electron temperatures ($2.0 \times 10^4 \text{ K}$ and $2.7 \times 10^4 \text{ K}$) from the [O III] $\lambda 4363$ /[O III] $\lambda 5007$ ratios with PyNeb and ICF (1.05 and 1.30) from the [O III]/[O II] ratios (Berg et al. 2019). At the higher redshifts of the other four galaxies (GN-z11, GS-z12-0, GHZ2, CAPERS-EGS-87132), the [O III] lines are shifted out of the NIR-Spec spectra, precluding measurement of the temperature. For these systems, we adopt the electron temperature and ICF that was derived from the composite spectrum.

We next constrain the C III]/O III] flux ratios. The deblended O III] emission lines are detected in the medium resolution grating spectra of GS-z9-0 and GN-z11, enabling direct measurement of the flux ratio. We derive $\log(C/O) = -0.83 \pm 0.10$ ($0.27 \pm 0.06 \text{ C/O}_{\odot}$) for GS-z9-0 and $\log(C/O) = -0.73 \pm 0.16$ ($0.34 \pm 0.13 \text{ C/O}_{\odot}$) for GN-z11, consistent with the C/O ratios reported for these sources previously (Cameron et al. 2023a; Curti et al. 2025). For the other four galaxies (GS-z12-0, GHZ2, CAPERS-EGS-25297, and CAPERS-EGS-87132), we only detect blended He II+O III] emission in the prism spectra. As with our composite, we assume the He II/O III] ratio is 0.25.

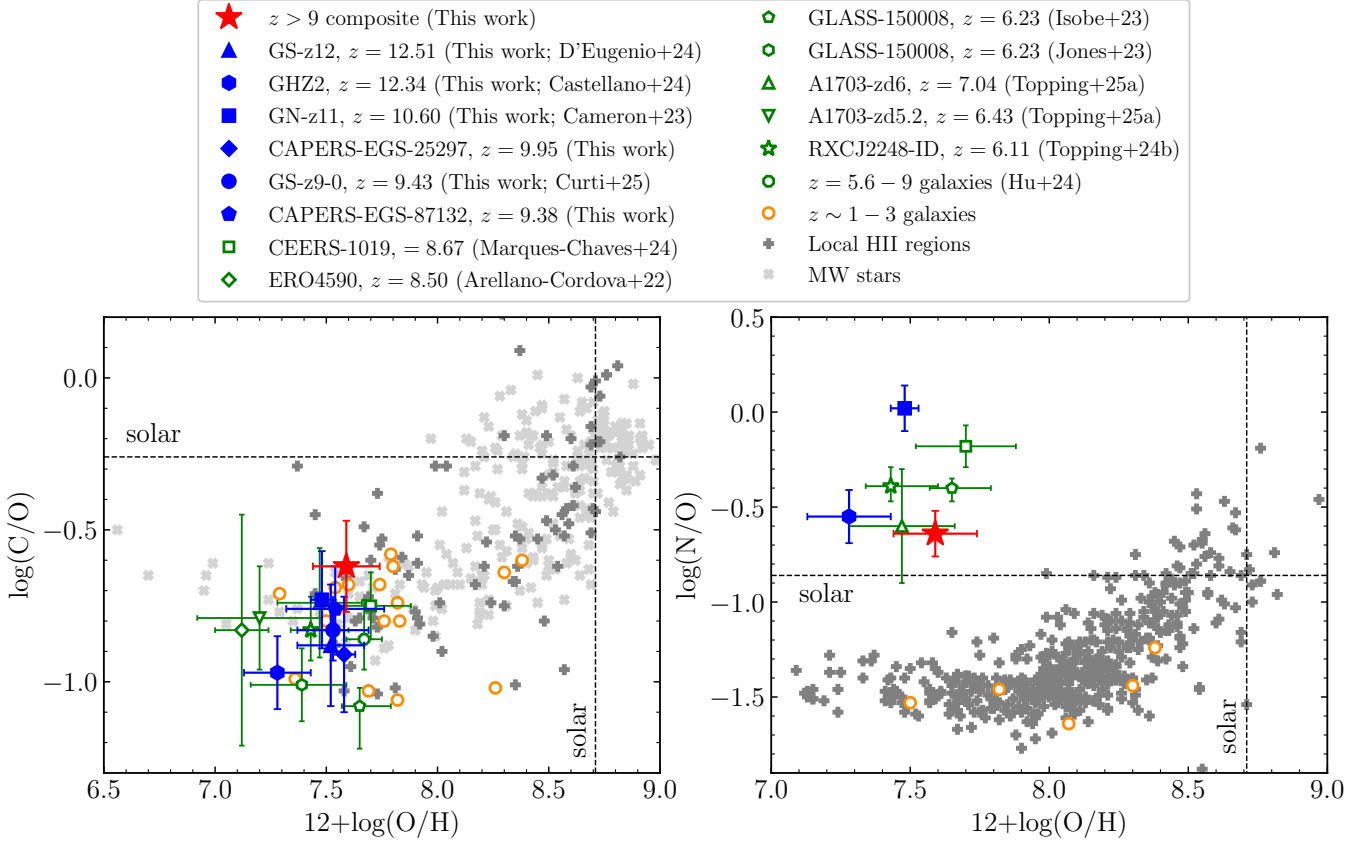


Figure 8. C/O ratio (left) and N/O ratio (right) as a function of oxygen abundance O/H. We show the abundance patterns of individual $z > 9$ galaxies as solid blue symbols (triangle: GS-z12-0; hexagon: GHZ2; square: GN-z11; diamond: CAPERS-EGS-25297; circle: GS-z9-0; pentagon: CAPERS-EGS-87132) and the composite spectrum at $z > 9$ as solid red stars. For comparison, we overplot the abundance patterns of high redshift galaxies with *JWST*/NIRSpec measurements in literature as open green symbols: CEERS-1019 (square, Marques-Chaves et al. 2024), ERO4590 (diamond, Arellano-Córdova et al. 2022), GLASS-150008 (pentagon, Isobe et al. 2023; hexagon, Jones et al. 2023), A1703-zd6 and A1703-zd5.2 (triangle, Topping et al. 2025a), RXCJ2248-ID (star, Topping et al. 2024b), and the average at $z = 5.6 - 9$ (octagon, Hu et al. 2024). We also present $z \sim 1 - 3$ galaxies (open orange circles, Erb et al. 2010; Christensen et al. 2012; Bayliss et al. 2014; James et al. 2014; Stark et al. 2014; Steidel et al. 2016; Amorín et al. 2017; Berg et al. 2018; Mainali et al. 2020; Matthee et al. 2021; Iani et al. 2023; Citro et al. 2024), local H II regions (solid dark grey plus, Esteban et al. 2004, 2009, 2014; García-Rojas et al. 2004, 2005; García-Rojas & Esteban 2007; López-Sánchez et al. 2007; Pilyugin et al. 2012; Berg et al. 2016, 2019; Toribio San Cipriano et al. 2016; Senchyna et al. 2017), and Milky Way stars (solid light grey cross, Gustafsson et al. 1999; Akerman et al. 2004; Bensby & Feltzing 2006; Nissen et al. 2014).

Following the steps described above, we derive $\log(C/O) = -0.97 \pm 0.12$ (0.19 ± 0.05 C/O $_{\odot}$) for GHZ2, consistent with that reported in Castellano et al. (2024). For the two galaxies with newly-identified O III] and C III], we derive $\log(C/O) = -0.91 \pm 0.19$ (0.22 ± 0.09 C/O $_{\odot}$; CAPERS-EGS-25297) and $\log(C/O) = -0.76 \pm 0.14$ (0.32 ± 0.10 C/O $_{\odot}$; CAPERS-EGS-87132).

We finally consider GS-z12-0, which was first discussed in D’Eugenio et al. (2024). This source presents a confident detection of C III] (S/N = 4) and a somewhat weaker (S/N = 3) detection of O III] (blended with He II). Adopting the approach described above, we infer a C/O ratio of $\log(C/O) = -0.88 \pm 0.20$ from the C III]/O III] measurement. This implies a sub-solar C/O

ratio (0.24 ± 0.11 C/O $_{\odot}$), similar to what is seen in the other galaxies described above. D’Eugenio et al. (2024) have pointed out that a larger C/O ratio is obtained for this galaxy based on the C III]/([O II] + [Ne III]) ratio. However, they find a sub-solar C/O ratio (similar to what we derived above) when using the more standard rest-frame UV-based methods. Based on these results, we conclude that there is not enough information to reliably confirm that GS-z12-0 is an outlier in its C/O ratio. A deeper grating spectrum separating O III] and He II should yield a more confident C/O ratio.

There are ten galaxies in our sample that have C III] emission without showing detection of O III]. We compute the 3σ lower limits on the C/O ratios in these sys-

Table 2. Average physical properties of galaxies in our $z > 9$ sample derived for the composite spectra.

From BEAGLE photoionization modeling	
Age _{CSFH} (Myr)	23^{+9}_{-7}
sSFR (Gyr ⁻¹)	43^{+21}_{-12}
$\log(\xi_{\text{ion}}/\text{erg}^{-1} \text{ Hz})$	$25.60^{+0.05}_{-0.06}$
$\log U$	$-2.11^{+0.08}_{-0.07}$
Z/Z_{\odot}	$0.11^{+0.02}_{-0.02}$
ξ_d	$0.38^{+0.08}_{-0.14}$
From emission line ratios	
$E(B - V)$	$0.06^{+0.20}_{-0.06}$
$T_e(\text{O III})$ (K)	21000^{+3000}_{-4000}
$12 + \log(\text{O}/\text{H})_{T_e}$	$7.59^{+0.14}_{-0.16}$
$12 + \log(\text{O}/\text{H})_{\text{R23}}$	$7.39^{+0.08}_{-0.08}$
$12 + \log(\text{O}/\text{H})_{\text{O3}}$	$7.41^{+0.08}_{-0.08}$
$\log(\text{C}/\text{O})$	-0.62 ± 0.15
$\log(\text{N}/\text{O})$	-0.64 ± 0.12

NOTE—C/O and N/O ratios are derived using the O III] emission line measured from the composite spectrum at $z > 9$, which is deblended from He II assuming a He II/O III] flux ratio of 0.25 implied from the best-fit BEAGLE model.

tems, following the same methods described above. We find that the spectra imply C/O ratio lower limits ranging from 0.15 C/O_⊙ to 0.44 C/O_⊙, with a median of 0.22 C/O_⊙. Deeper spectra will be required to verify the C/O ratios in these systems, but the current lower limits appear consistent with the C/O – O/H trends seen at lower redshifts (e.g., Garnett et al. 1995; Berg et al. 2019).

4.4. Nitrogen-to-oxygen ratios

We characterized the N IV] and N III] emission lines in our $z > 9$ sample in Section 3.4. Previous investigations have computed the N/O ratios for the small number of $z > 9$ galaxies with nitrogen line detections, finding evidence for elevated N/O abundance ratios that are similar to those seen in many globular cluster stars (Cameron et al. 2023a; Senchyna et al. 2024; Castellano et al. 2024; Schaerer et al. 2024; Curti et al. 2025; c.f., Flury et al. 2024). With a sample size of 61 galaxies, we can now put the $z > 9$ detections in context, both considering a composite spectrum and the large number of non-detections. Here we use the emission line measure-

ments to characterize the typical N/O ratios in $z > 9$ galaxies.

We first consider the N/O ratio implied by the composite (top panel of Figure 2). The detection of N IV] in the composite hints at nitrogen enhanced conditions. In quantifying the N/O ratio, we will assume that the oxygen abundance is dominated by O⁺⁺, following other recent analyses (e.g., Isobe et al. 2023; Castellano et al. 2024; Marques-Chaves et al. 2024; Topping et al. 2024b). Since N III] is not detected in the composite spectrum, we derive the N/O ratio from the N IV]/O III] flux ratio as $\text{N}/\text{O} \simeq \text{N}^{3+}/\text{O}^{++}$. Using PyNeb and assuming $T_e = 2.1 \times 10^4$ K (Section 3.7) and $n_e = 2 \times 10^4 \text{ cm}^{-3}$ (Topping et al. 2025b), we derive an average N/O ratio of $\log(\text{N}/\text{O}) = -0.64 \pm 0.12$ ($1.7 \pm 0.5 \text{ N}/\text{O}_{\odot}$; right panel of Figure 8 and Table 2), suggesting a super-solar N/O ratio (solar abundance ratio $\log(\text{N}/\text{O}) = -0.86$; Asplund et al. 2009).

This result suggests that typical galaxies at $z > 9$ may have nitrogen-enhanced gas conditions. To test whether this result is driven by the small number of detections, we generate another composite spectrum without the four nitrogen line emitters (GN-z9p4, GN-z11, UNCOVER-3686, GHZ2). Following the same steps described above, we derive an elevated N/O ratio that is consistent with that inferred from the composite including those four systems.

For completeness, we also assemble the N/O ratios in the four individual $z > 9$ galaxies in our sample with N IV] detections. Two galaxies have spectra that reveal the rest-frame UV nitrogen lines and O III] (GN-z11 and GHZ2). Both N IV] and N III] are detected in the NIRSpec spectra of these two systems, and we infer their N/O ratios as $\text{N}/\text{O} \simeq (\text{N}^{3+} + \text{N}^{++})/\text{O}^{++}$. We find $\log(\text{N}/\text{O}) = 0.02 \pm 0.12$ ($7.6 \pm 2.1 \text{ N}/\text{O}_{\odot}$) for GN-z11 and $\log(\text{N}/\text{O}) = -0.55 \pm 0.14$ ($2.0 \pm 0.6 \text{ N}/\text{O}_{\odot}$) for GHZ2 (right panel of Figure 8), consistent with those inferred in the respective discovery papers (Bunker et al. 2023; Cameron et al. 2023a; Senchyna et al. 2024; Castellano et al. 2024). In the other two N IV] emitters in our $z > 9$ sample (GN-z9p4 and UNCOVER-3686), we do not detect O III] emission. Using the 3σ upper limits of O III] flux, we derive N/O of $> 1.6 \text{ N}/\text{O}_{\odot}$ for both GN-z9p4 and UNCOVER-3686.

Finally, there are four $z > 9$ galaxies in our database with O III] emission but without nitrogen line detections (GS-z9-0, GS-z12-0, CAPERS-EGS-25297, and CAPERS-EGS-87132). Using the 3σ upper limits of N IV] and N III] fluxes, we infer N/O ratios of $< 0.5 - 2.9 \text{ N}/\text{O}_{\odot}$ for these four systems, with a median 3σ upper limit of N/O of $< 1.8 \text{ N}/\text{O}_{\odot}$. Deeper spectra

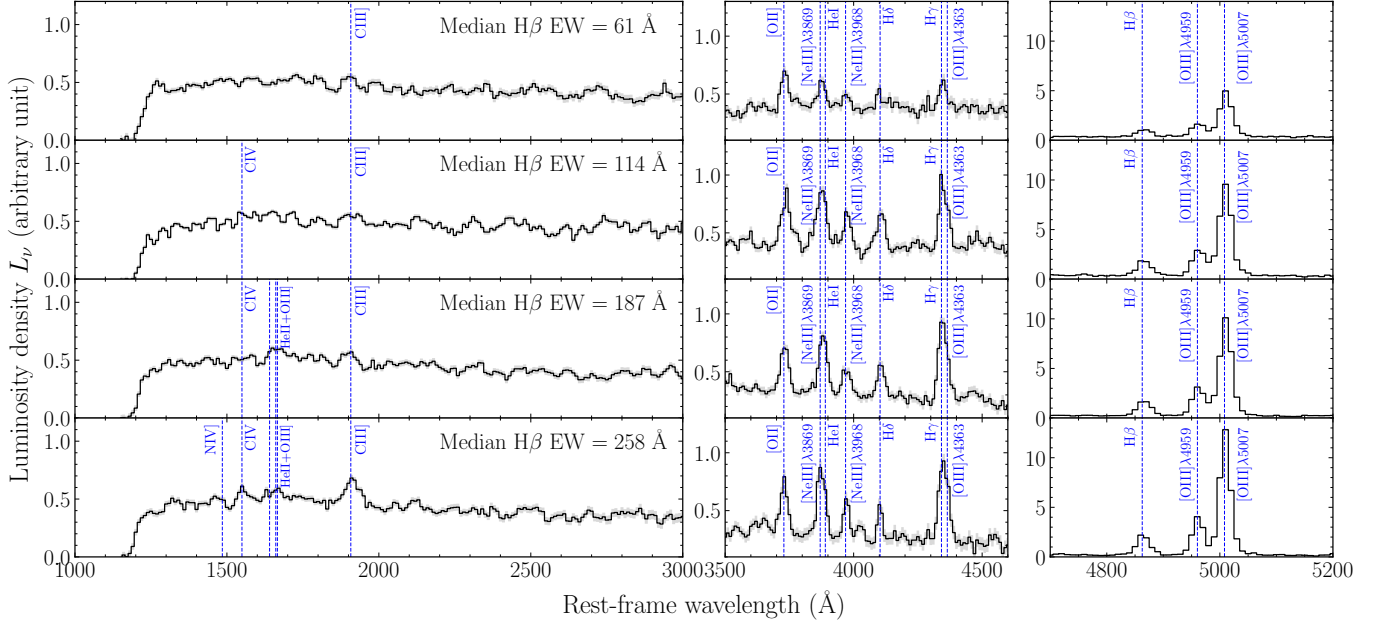


Figure 9. Composite prism spectra of galaxies in our $6 < z < 9$ sample, binned by $H\beta$ EW. From the top to the bottom we show the composites of galaxies with $H\beta$ EW = 10 – 80 Å, 80 – 150 Å, 150 – 230 Å, and 230 – 500 Å. Emission line detections are marked by blue dashed lines.

will be required to verify if the gas is nitrogen-enriched in these galaxies.

5. EVOLUTION IN GALAXY SPECTRA AT $z > 9$

One of the primary goals of this paper is to investigate whether there is evidence for a sudden shift in the burst fraction or star formation efficiency at $z > 9$. The first step is empirical, establishing whether the spectral properties are notably different than those at lower redshifts. To facilitate such a comparison, we build a reference sample of 401 galaxies at $6 < z < 9$ with NIRSpect observations. The selection of spectroscopic sources at $6 < z < 9$ is conducted similarly to that at $z > 9$ and is described in Appendix A. The composite spectra of our $6 < z < 9$ sample is shown in Figure 9, separated into bins of $H\beta$ EW (see Appendix A). In the following subsections, we directly compare the distribution of emission line strengths at $z > 9$ to those at $6 < z < 9$, paying close attention to whether the data reveal the emergence of a population with strong bursts.

5.1. $H\beta$ and $H\gamma$ emission

The hydrogen recombination lines provide the most direct constraint on the presence of strong bursts. If strong bursts become more common at $z > 9$, we should see an increase in the presence of galaxies with extremely large $H\beta$ and $H\gamma$ EWs. We have demonstrated that $23^{+8}_{-7}\%$ of the $z > 9$ galaxies in our sample present extremely strong $H\beta$ (EW > 240 Å) or $H\gamma$ emission lines (EW > 80 Å) linked to very young stellar populations

formed in recent bursts. Using the spectroscopic sample at $6 < z < 9$, we can test whether this population is becoming more common at earlier epochs.

Because $H\beta$ emission lines have higher S/N ratios than $H\gamma$ emission lines, we primarily focus on the fraction of galaxies with strong $H\beta$ (EW > 240 Å) at $6 < z < 9$. All of the 401 $6 < z < 9$ galaxies in our spectroscopic sample have deep enough spectra to reach $H\beta$ EW limit of < 240 Å at 3σ , and 41 of them show strong $H\beta$ with EW > 240 Å. This indicates a fraction of strong $H\beta$ emitters of $10^{+2}_{-2}\%$. We also quantify the fraction of strong $H\gamma$ emitters (EW > 80 Å) at $6 < z < 9$ using the subset of systems with spectra reaching $H\gamma$ EW limit of < 80 Å at 3σ (141 objects). Among this subsample, we identify 13 galaxies with $H\gamma$ EW > 80 Å, indicating a fraction of $9^{+3}_{-2}\%$ that is similar to the fraction of strong $H\beta$ emitters. This reveals that strong Balmer line emitters ($H\beta$ EW > 240 Å or equivalently $H\gamma$ EW > 80 Å) are $\simeq 2\times$ more common at $z > 9$ than at $6 < z < 9$ (left panel of Figure 10), as would be expected if $z > 9$ galaxies are significantly more likely to be undergoing strong bursts of star formation.

We can also investigate the evolution in the mean $H\beta$ EW, using composite spectra centered at $z \simeq 6.5$, 7.5, and 8.5 (see Appendix A) together with our composite at $z > 9$. We find 103 Å ($z \simeq 6.5$), 108 Å ($z \simeq 7.5$), 136 Å ($z \simeq 8.5$), while our $z > 9$ composite is characterized by $H\beta$ EW = 150 Å (Table 1). Hence our data support mild evolution in the mean $H\beta$ EWs, with slightly larger

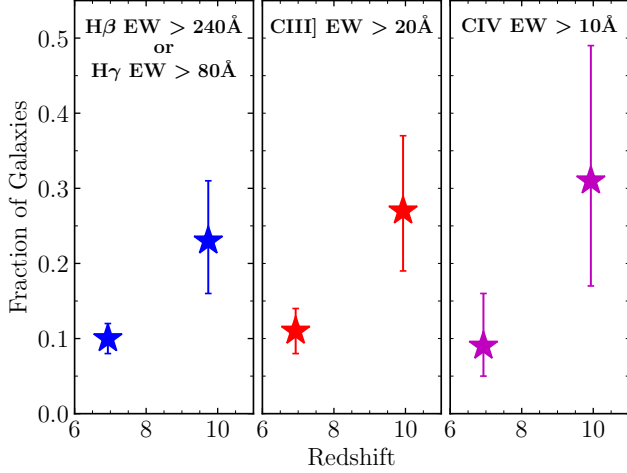


Figure 10. Redshift evolution in the fraction of galaxies presenting strong emission lines. The left, middle, and right panels show the fraction of galaxies with strong H β (EW > 240 Å) or H γ (EW > 80 Å), C III] (EW > 20 Å), or C IV (EW > 10 Å) emission lines, respectively.

values at $z > 9$ (left panel of Figure 11), similar to what was reported in Roberts-Borsani et al. (2024).

Overall, our database supports evolution in the H β EWs at $z > 9$, with the most prominent shift at the upper end of the H β EW distribution. This provides our first line of evidence suggesting that the emission line properties are fundamentally different at $z > 9$, with the most extreme emitters forming a larger fraction of the population. We note that this is unlikely to be a selection effect since the $z > 9$ sample should not be any more biased toward emission line sources than that at $6 < z < 9$. Indeed, at $z > 9$, most of the strong lines are redshifted out of the NIRSpec bandpass, reducing the dependence on emission lines for redshift confirmation. The rise in the strongest line emitters at $z > 9$ is precisely what would be expected if the galaxy population is becoming more dominated by systems that have recently experienced a significant upturn in star formation. In the following two subsections, we investigate whether similar signatures are seen in other emission lines.

5.2. C III] emission

Previous work has demonstrated that the mean C III] EW increases with redshift at $z > 6$ (Roberts-Borsani et al. 2024). Our spectra suggest a similar result. We have generated composites from our lower redshift sample, with bins centered at $z \simeq 6.5, 7.5, 8.5$ (Appendix A). The C III] EWs of the stacks increase with redshift (right panel of Figure 11), from 6.6 ± 0.6 Å at $z \simeq 6.5$, to 7.7 ± 1.1 Å at $z \simeq 7.5$, to 12.7 ± 1.7 Å at $z \simeq 8.5$. The

C III] EW in our $z > 9$ composite (12.6 ± 1.8 Å) is larger than the range found at $6 < z < 9$, suggesting continued evolution toward larger C III] EWs at higher redshifts.

Perhaps more striking is the fact that a large fraction ($27^{+10}_{-8}\%$) of $z > 9$ galaxies have extremely large C III] EWs (> 20 Å). Here we test whether the fraction of strong C III] emitters increases sharply with redshift at $z > 9$ through comparison to our sample at $6 < z < 9$. Among the galaxies with deep enough spectra to reach C III] EW limits of 20 Å at 3σ (149 galaxies), 16 present C III] with EW > 20 Å, indicating a large C III] EW fraction of $11^{+3}_{-3}\%$ at $6 < z < 9$. This is significantly less than the fraction ($27^{+10}_{-8}\%$) of $z > 9$ galaxies that show similarly large C III] EWs (middle panel of Figure 10). This suggests that the upper end of C III] EW distribution likely undergoes significant evolution at $z > 9$, with extremely large C III] EWs 2 – 3 \times more common than at $6 < z < 9$.

To gain intuition for why the C III] EW distribution evolves with redshift at $z > 9$, we measure the dependence of C III] EW on the H β EW at $6 < z < 9$. Since the latter quantity tracks the light-weighted stellar population age (and based on Section 5.1, appears to increase at $z > 9$), we may expect evolution in the C III] EWs if the galaxy population comes to be dominated by stronger bursts or larger star formation efficiency.

As described in Appendix A, we have created stacked spectra in four bins of H β EW (Figure 9). Using the composite spectra, we find that the C III] EW increases steadily with H β EW (Figure 12), from C III] EW = 5 ± 1 Å (at H β EW = 61 Å) to C III] EW = 19 ± 2 Å (at H β EW = 258 Å). The individual galaxies at $6 < z < 9$ present a similar trend, though with scatter. To quantify the connection between C III] EW and H β EW, we fit the stacked C III] EWs and H β EWs (in the logarithm) with a linear function:

$$\log_{10}(\text{EW}_{\text{CIII]}}/\text{Å}) = 0.92 \cdot \log_{10}(\text{EW}_{\text{H}\beta}/\text{Å}) - 0.89 \quad (1)$$

Based on this relation, we see that the very high C III] EW (> 20 Å) galaxies which comprise 27% of the population at $z > 9$ tend to have H β EW = 240 Å at $6 < z < 9$, corresponding to light-weighted stellar population ages of 5 Myr, for constant star formation with BEAGLE. We emphasize that this equation gives the average C III] EW as a function of H β EW. The scatter about this relation is driven by variations in gas-phase metallicity and C/O ratios (e.g., Gutkin et al. 2016; Jaskot & Ravindranath 2016; Plat et al. 2019; Tang et al. 2021). In the context of the results at $6 < z < 9$, the observed shift in the C III] EW distribution at $z > 9$ can be explained by evolution in the light-weighted stellar pop-

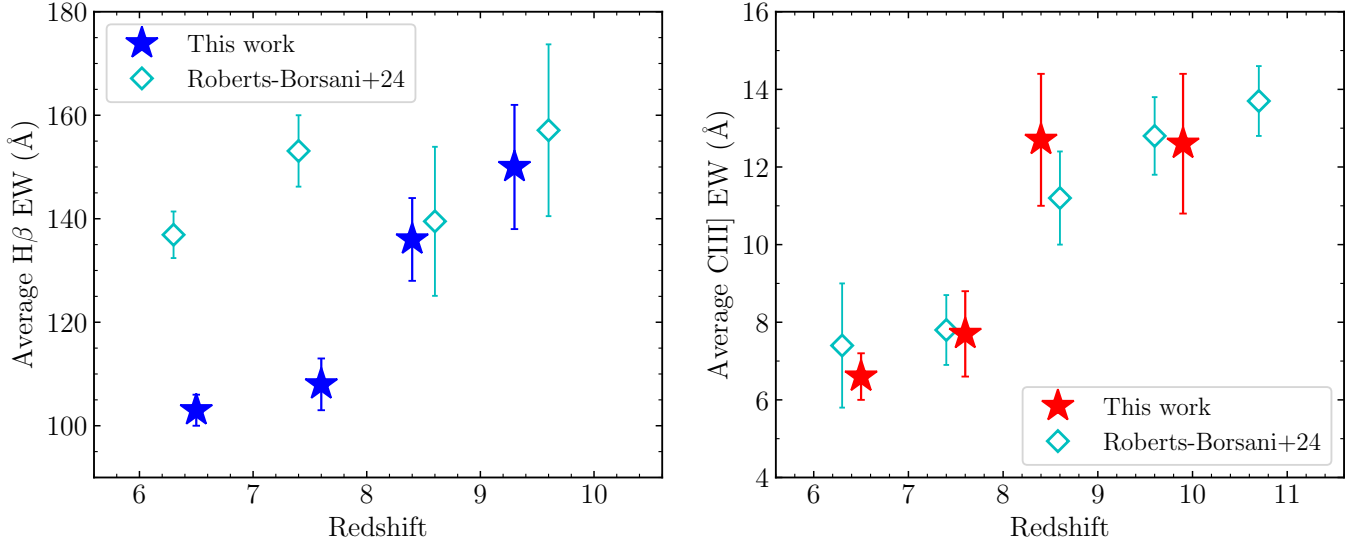


Figure 11. Redshift evolution of the average H β EW (left panel) and C III] EW (right panel) measured from composite spectra from $6 < z < 9$ to $z > 9$ (blue stars: H β ; red stars: C III]). We overplot data from Roberts-Borsani et al. (2024) as open cyan diamonds as comparison.

ulation ages (which regulate the H β EWs) coupled with variations in the gas-phase properties at $z > 9$. We will discuss these possibilities in more detail in Section 6.

5.3. C IV emission

We have found that our composite spectrum at $z > 9$ exhibits C IV emission (EW = 5.3 Å), indicating hard radiation fields capable of triply ionizing carbon are likely typical. Moreover, roughly 31% of $z > 9$ galaxies have extremely strong C IV emission (EW > 10 Å). Here our goal is to determine if such strong C IV emitters are more common at $z > 9$ than in similar samples at $6 < z < 9$, as may be expected if there is a rise in hard ionizing sources at $z > 9$.

We first quantify the fraction of $6 < z < 9$ galaxies presenting C IV emission with EW > 10 Å directly from the spectroscopic sample. There are 43 galaxies with deep enough spectra to reach C IV EW limits of 10 Å at 3σ . We identify 4 with C IV detections having EW > 10 Å. This indicates the fraction of strong C IV emitter of $9^{+7}_{-4}\%$ at $6 < z < 9$, consistent with that of $z > 4$ galaxies (8%) presented in Topping et al. (2025a). Notably, this fraction is well below that measured at $z > 9$ ($31^{+18}_{-14}\%$; right panel of Figure 10). While statistics remain poor at the highest redshifts, our results suggest that the strongest C IV emitters are indeed more common among the $z > 9$ population.

We can gain insight into the physics regulating the emergence of strong C IV emitters at $z > 9$ by investigating the connection between the C IV and H β EWs in the composite spectra at $6 < z < 9$ (Figure 9). In the stack of galaxies with H β EW = 10 – 80 Å, we do

not identify C IV emission, placing a 3σ upper limit on the average C IV EW < 3 Å. We only start seeing the presence of C IV emission in the composites of galaxies with larger H β EWs. The C IV EW increases from 3.2 ± 0.9 Å to 4.9 ± 1.3 Å to 7.1 ± 1.4 Å in the composites of galaxies with H β EW = 80 – 150 Å, 150 – 230 Å, and 230 – 500 Å, respectively. To quantify the relationship between C IV EW and H β EW, we fit the logarithm of EWs measured from composite spectra with a linear function:

$$\log_{10}(\text{EW}_{\text{CIV}}/\text{Å}) = 0.97 \cdot \log_{10}(\text{EW}_{\text{H}\beta}/\text{Å}) - 1.45 \quad (2)$$

The C IV EW – H β EW trend suggests a picture that is consistent with what is implied from the demographics of C IV detections at lower redshifts. The hard ionizing spectra powering strong C IV is more typical among metal poor ($\lesssim 0.1 Z_{\odot}$) galaxies dominated by extremely young stellar populations formed in recent strong bursts of star formation (Senchyna et al. 2019; Topping et al. 2025a). Based on these results, the increase in the fraction of strong (EW > 10 Å) C IV emitters at $z > 9$ can be explained by the emergence of a metal poor population with extremely large H β EW of > 330 Å, consistent with the increase in large H β and H γ EWs presented in Section 5.1. Such H β EWs correspond to a very young stellar population age of < 3 Myr assuming CSFH, as expected in galaxies that have experienced a recent strong burst of star formation. It is also possible that the evolution in C IV emission may reflect the rise of AGN with hard ionizing spectra at $z > 9$. Indeed, one of the C IV

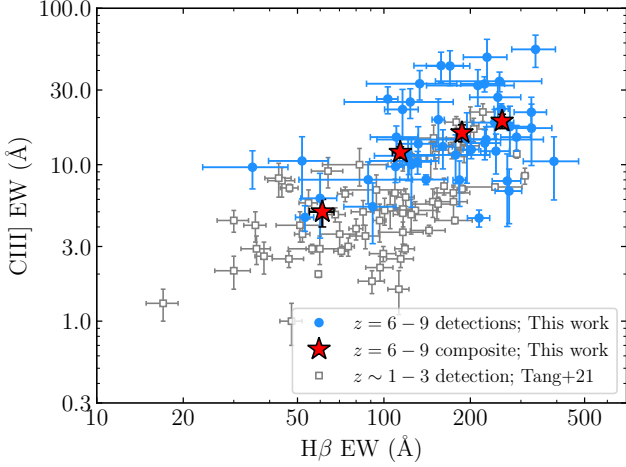


Figure 12. Dependence of C III] EW on H β EW. We show the average C III] EWs and H β EWs measured from the composite spectra at $6 < z < 9$ (red stars), binning by H β EW. We also show the subset with C III] detections with S/N > 3 at $6 < z < 9$ (blue circles). As a comparison, we overplot the data at $z \sim 1-3$ as grey open squares (see Tang et al. 2021 and references therein).

emitters (GHZ9) has been claimed as a potential AGN based on X-ray emission (Kovács et al. 2024; Napolitano et al. 2024). We will return to comment on implications of the C IV evolution for ionizing sources at $z > 9$ in Section 6.2.

6. DISCUSSION

6.1. Stellar Populations at $z > 9$

The spectra of $z \gtrsim 9$ galaxies are starting to provide a window on what appears to be a significant transformation in the galaxy population at the highest redshifts probed by *JWST*. We have shown that H β , H γ , and C III] emission line EWs undergo rapid evolution between $6 < z < 9$ and $z > 9$, as would be expected if younger stellar populations (formed in recent bursts) come to dominate the spectra at $z > 9$. Not only is the average emission line EW larger at $z \gtrsim 9$ (as previously shown in Roberts-Borsani et al. 2024), but a greater fraction of the population is found with extremely large EW line emission. In the context of the population synthesis models, these results suggest that nearly $23^{+7}_{-6}\%$ of $z \gtrsim 9$ galaxies have undergone strong upturns in recent star formation, with the SFR averaged over the most recent 3 Myr more than 4 times that averaged over the previous 3–50 Myr. In contrast, only $10^{+2}_{-2}\%$ of the $z \simeq 6-9$ population was found in the midst of such strong bursts of star formation. To illustrate the implied evolution, we show the inferred $\text{SFR}_{3\text{Myr}}/\text{SFR}_{3-50\text{Myr}}$ ratios in $6 < z < 9$ and $z > 9$ samples in Figure 13. Overall, the $z > 9$ distribution of $\text{SFR}_{3\text{Myr}}/\text{SFR}_{3-50\text{Myr}}$

ratios appears more flattened, with the upper end of the distribution shifted toward larger values.

One potential explanation for the observed evolution is that the UV scatter (σ_{UV}) increases with redshift above $z \simeq 9$, broadening the range of UV luminosities exhibited by galaxies of a given halo mass. In this case, the observed galaxy population at higher redshifts will have a larger contribution from low mass halos which have been upscattered to larger luminosities. The impact of σ_{UV} evolution has been discussed in the context of the UV luminosity function (e.g., Mason et al. 2023; Mirocha & Furlanetto 2023; Shen et al. 2023; Sun et al. 2023; Gelli et al. 2024; Kravtsov & Belokurov 2024), providing a plausible explanation for the abundance of the brightest galaxies at $z \simeq 14$ (c.f., Feldmann et al. 2025). However it will also lead to an increase in the prevalence of galaxies with extremely large emission line EWs, as we have shown is likely to be the case at $z \gtrsim 9$ (Section 5, see also Roberts-Borsani et al. 2024; KokoREV et al. 2025). An increase in σ_{UV} should also introduce a larger population of galaxies with recent downturns in star formation, broadening the distribution of $\text{SFR}_{3\text{Myr}}/\text{SFR}_{3-50\text{Myr}}$ ratios. We have demonstrated some of the weakest emission line sources in our sample are likely to be in such a phase (see Section 4.1).

Other mechanisms may also contribute to an increase in the frequency of galaxies with strong bursts at $z \gtrsim 9$. These additional explanations mostly require the UV scatter to have a strong dependence on halo mass, with larger σ_{UV} in lower mass halos as is often found in hydrodynamical simulations (e.g., Katz et al. 2023; Sun et al. 2023; Feldmann et al. 2025). In this case, any physical effect which causes higher redshift samples to probe lower mass halos (at a given UV luminosity) will also cause higher redshift samples to sample halos with larger σ_{UV} . One such mechanism is evolution in baryon accretion rates, which are expected to scale as $(1+z)^{2.5}$ (Neistein & Dekel 2008; Dekel et al. 2009; McBride et al. 2009), and increasing the SFR at fixed halo mass by a corresponding factor. As a result, higher redshift galaxies should tend to sit in lower halo masses at a given M_{UV} . If σ_{UV} is larger in the lower mass population, the higher redshift samples will preferentially probe halos where stronger bursts are present. Evolution toward larger SFE at higher redshift (e.g., Dekel et al. 2023; Qin et al. 2023; Somerville et al. 2025) would also cause the $z \gtrsim 9$ samples to sample lower halo masses at fixed M_{UV} than those at lower redshift, further amplifying the evolution in the strong burst fraction. Finally, we note that the observed shift in emission line EWs could be additionally impacted by evolution in the initial mass function or an increasing fraction of AGN. Meanwhile

if there is significant positive evolution in the ionizing photon escape fractions, we may observe a rise in the fraction of weak emission line sources. Progress toward decoupling these effects should come with deeper spectroscopy of bright $z > 9$ galaxies.

While the various physical mechanisms described above each broaden the distribution of $\text{SFR}_{3\text{Myr}}/\text{SFR}_{3-50\text{Myr}}$ ratios, they are nevertheless distinct in how they alter the distribution. In a future work (Gelli et al., in preparation), we will quantify the impact that the proposed evolution in σ_{UV} , baryon accretion rates, and SFE (or a shallow relationship between halo mass and SFE as in Feldmann et al. 2025) have on the star formation histories. This work offers the potential for a new observational constraint on explanations for the slow evolution of the UV luminosity function at $z \simeq 9 - 14$, ensuring that the proposed mechanisms are consistent with the inferred $\text{SFR}_{3\text{Myr}}/\text{SFR}_{3-50\text{Myr}}$ ratios seen in Figure 13. The utility of such comparisons will be improved as more robust limits are placed on weak emission lines in sources that may have experienced recent downturns of star formation. The existing upper limits are often not stringent enough to place meaningful constraints on the recent SFH, particularly at the highest redshifts where we primarily sample the rest-frame UV. Approved *JWST* programs in Cycle 4 should enable progress through combination of MIRI spectroscopy (probing the rest-frame optical) with new ultra-deep NIRSpect observations (probing the rest-frame UV).

6.2. Implications for Ionizing Sources at $z > 9$

A shift in star formation histories at $z \gtrsim 9$ may also help explain the prevalence of the extreme rest-frame UV spectra at the highest redshifts probed by *JWST* in the last few years. The high ionization emission in GNz11 (Bunker et al. 2023) provided the first evidence that hard ionizing agents may be common at $z \gtrsim 9$. Subsequent investigations have built on this picture, revealing extremely strong C IV emission in GHZ2 (Castellano et al. 2024), GHZ9 (Napolitano et al. 2025), and in MoM-z14 (Naidu et al. 2025). The CAPERS program (GO 6368, PI: M. Dickinson) has recently added another strong C IV emitter (CAPERS-COSMOS-109917) to the $z > 9$ database (Section 3.3).

In this paper, we have demonstrated that 31% of $z > 9$ galaxies have C IV emission with $\text{EW} > 10 \text{ \AA}$ (Figure 10), more than three times the percentage of the $6 < z < 9$ population with similarly strong C IV. While AGN activity may help power C IV emission in some cases (perhaps likely in GHZ9 given its X-ray detection, Napolitano et al. 2025), metal poor stellar populations

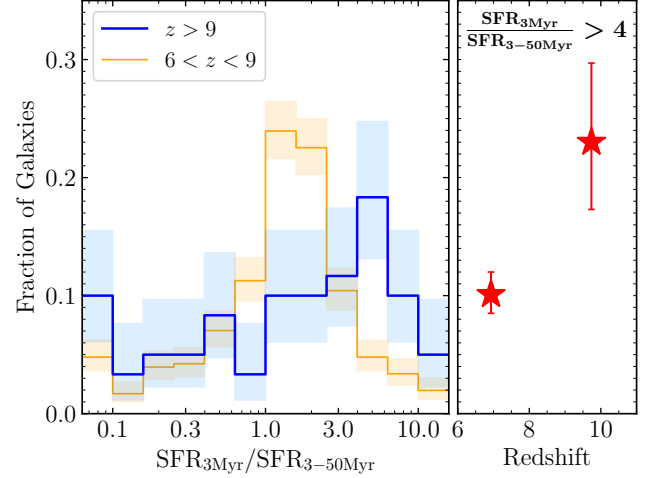


Figure 13. Left panel: Distribution of SFR ratios ($\text{SFR}_{3\text{Myr}}/\text{SFR}_{3-50\text{Myr}}$) of galaxies at $z > 9$ (blue line) and $6 < z < 9$ (orange line) in our spectroscopic sample. The SFR ratios are derived from TcSFH models with BEAGLE (Section 2.6), with shaded regions showing 1σ confidence intervals. Galaxies with large upturns in SFR ($\text{SFR}_{3\text{Myr}}/\text{SFR}_{3-50\text{Myr}} > 4$) are more common among $z > 9$ galaxies than $6 < z < 9$ galaxies. Right panel: Evolution of the fraction of galaxies with large upturns in SFR ($\text{SFR}_{3\text{Myr}}/\text{SFR}_{3-50\text{Myr}} > 4$) from $6 < z < 9$ to $z > 9$.

with young ages can power C IV emission up to $> 60 \text{ \AA}$ (Plat et al. 2025, in preparation). This model-based prediction is supported by the observed strong relationship between C IV EW and H β EW (Section 5.3). Based on these results, we suggest that the rise of hard ionizing spectra at $z > 9$ is likely a consequence of the increase in the percentage of the $z > 9$ population that is experiencing strong bursts of star formation (i.e., those with the largest H β EWs and largest C III] EWs).

Given the shift in star formation conditions, we may also expect to see evolution in the ionized gas properties at $z > 9$. There has been considerable focus on the nitrogen-enhanced abundance pattern seen in GNz11 (Bunker et al. 2023) and GHZ2 (Castellano et al. 2024) (along with similar galaxies at slightly lower redshifts, e.g., Isobe et al. 2023; Marques-Chaves et al. 2024; Topping et al. 2024b, 2025a). Here we find that the composite spectrum of 61 $z > 9$ galaxies shows evidence for N IV] emission, with line ratios that suggest mild nitrogen enhancement ($\text{N}/\text{O} = 1.7 \pm 0.5 \text{ N}/\text{O}_{\odot}$) is common in $z > 9$ galaxies. The physics that causes the nitrogen-enriched abundance pattern remains debated (e.g., Nagele & Umeda 2023; Cameron et al. 2023a; Charbonnel et al. 2023; Isobe et al. 2023, 2025; Flury et al. 2024; Kobayashi & Ferrara 2024; Senchyna et al. 2024; Ji et al. 2025), but the demographics suggest a link to the high density conditions which form during

compact bursts of star formation (Topping et al. 2024b, 2025a; Schaerer et al. 2024). Topping et al. (2025a) have demonstrated that nitrogen-enhancement only becomes common among galaxies with $[\text{O III}]+\text{H}\beta$ EW > 2500 Å. While such strong bursts are relatively rare at $z \simeq 6$, our results suggest they become fairly common at $z > 9$, providing a natural explanation for the rise of nitrogen-enhancement in the early galaxy population. The nitrogen emitters may provide signposts of dense stellar environments where stellar collisions are likely (Charbonnel et al. 2023; Marques-Chaves et al. 2024; Senchyna et al. 2024). These dense star clusters may provide the ideal environments for the build-up of intermediate mass black holes (IMBHs; e.g., Miller & Hamilton 2002; Portegies Zwart & McMillan 2002; Kremer et al. 2020; Rantala et al. 2025; see Greene et al. 2020 for a review). The *JWST* spectroscopic database is revealing that galaxies at $z \gtrsim 9$ are more likely to have nitrogen-enhancements than those at $6 < z < 9$, as we might expect if galaxies are more likely to form stars in denser cluster complexes at $z \simeq 9 - 14$. If our initial spectroscopic census is correct, we should continue to find extreme spectra like GNz11 and GHZ2 as $z \gtrsim 9$ samples grow in number, allowing us to better study the potential connection between the nitrogen emitters and IMBH formation.

6.3. Dust in $z > 9$ Galaxies

The dust content of $z > 9$ galaxies has been a topic of interest in the last several years (e.g., Ferrara et al. 2023; Narayanan et al. 2025), largely driven by *JWST* measurements of UV continuum slopes. NIRCам provided our first statistical exploration of UV slopes at $z \gtrsim 9$, revealing extremely blue colors indicative of negligible attenuation (e.g., Austin et al. 2024; Cullen et al. 2024; Morales et al. 2024; Topping et al. 2024a). Prism spectroscopy has suggested a similar picture, with the average UV colors approaching the values expected from the combined emission of stellar and nebular continuum. At redshifts above $z \simeq 9$, Saxena et al. (2024) have suggested that the evolution in UV colors may plateau (with UV colors potentially even becoming slightly redder), potentially reflecting the strong contribution of nebular continuum to the underlying SED.

In this paper, we have measured UV continuum slopes of 60 $z \simeq 9 - 14$ galaxies using the NIRSpec prism spectra, a factor of $2\times$ larger than the sample considered in Saxena et al. (2024). The average UV slopes we measure are similarly blue as those found in Saxena et al. (2024). However, our spectroscopic sample suggests that the UV slopes may continue to evolve toward bluer colors between $z \simeq 9.7$ ($\beta = -2.28^{+0.05}_{-0.05}$) and $z \simeq 12.3$

($\beta = -2.48^{+0.13}_{-0.08}$), continuing the trend seen at slightly lower redshifts. While uncertainties remain significant at $z \gtrsim 9$, in our prism dataset, we do not find clear evidence for a plateau above $z \simeq 9$. This is consistent with the trend seen in photometric SEDs of the parent population of continuum-selected galaxies (Austin et al. 2024; Cullen et al. 2024; Topping et al. 2024a). Notably these studies have demonstrated UV slope evolution at $z \gtrsim 9$ among fainter ($M_{\text{UV}} \simeq -18.5$) galaxies. Accordingly, for spectroscopic samples to fully capture evolution in UV slopes at $z \gtrsim 9$, it will be necessary to extend existing $z \gtrsim 9$ samples to lower luminosities (see Figure 3). Larger samples would be able to clarify whether UV slope evolution slows down at the highest redshifts ($z \simeq 12$), as might be expected at redshifts where galaxies have negligible dust and minimal scatter in intrinsic slopes.

It remains an outstanding question whether there is a population of dusty sources at $z \gtrsim 9$. As described in Section 3.1, we have identified five red ($\beta \gtrsim -1.5$) galaxies at $z \gtrsim 9$ in our current sample. In the context of the picture put forward by Ferrara et al. (2023), these galaxies may correspond to galaxies without sufficient sSFR to eject their dust (see Ziparo et al. 2023) or those caught before the dust has been expelled. Red colors may also be expected in periods between bursts of star formation (Mirocha & Furlanetto 2023; Narayanan et al. 2025) or in galaxies with high electron densities ($n_e \gtrsim 10^5 \text{ cm}^{-3}$) and stellar populations dominated by very hot stars (Katz et al. 2024). In the latter case, very red slopes arise because the spectrum becomes increasingly nebular-dominated at high stellar temperatures in the far-to-near-UV, with densities large enough to collisionally de-excite the contribution from two photon emission in the far-UV. The slope of the nebular continuum SED without two photon emission is red without requiring dust. Which physical picture is responsible for the red galaxies at $z \gtrsim 9$ is not clear.

Knowledge of the dust content in the five systems is one of the keys to progress. Perhaps not surprisingly, the red galaxies have the largest inferred dust optical depths in our sample. Using the TcSFH BEAGLE models with a SMC extinction curve, we find that the V-band optical depths are in the range τ_V of $0.23 - 0.35$. Of course, these inferences depend on knowledge of the intrinsic continuum and the dust law. If the intrinsic spectrum is redder than allowed in our TcSFH models (as would be predicted in the high density nebular-dominated SEDs suggested in Katz et al. 2024), then the inferred dust attenuation will be overestimated. We can place further constraints on the impact of dust via the Balmer decrement. As discussed in Section 3.5, the two red

sources with constraints on $H\beta$ and $H\gamma$ have Balmer decrements that are consistent with modest reddening (i.e. $E(B - V) \simeq 0.2$). One of the two sources (JADES-GS-20077159) has the smallest $H\gamma/H\beta$ ratio in the sample, suggesting that in addition to showing the reddest UV slopes, these sources also have Balmer decrements that suggest the most nebular reddening in the sample. More complete coverage of the Balmer lines should yield more confident constraints on the attenuation in the future.

The emission lines in the red galaxies also provide useful insight. If the red colors arise during a post burst phase, we may expect to see weaker emission lines as O stars disappear (e.g., [Endsley et al. 2024a](#)). In contrast, if they are high gas density galaxies with very hot stars, we should see strong emission line spectra from transitions with large critical densities (i.e., [O III] $\lambda\lambda 4959, 5007$). Intriguingly, the reddest object in our sample, JADES-GS-20064312 ($\beta = -1.17$) has no emission line detections in its spectrum. To reproduce the weak emission lines, the TcSFH SED fits of this source require the lowest $\text{SFR}_{3\text{Myr}}/\text{SFR}_{3-50\text{Myr}}$ ratios in the sample. However, in two of the other galaxies with red UV colors, we find extremely strong emission line spectra (CAPERS-EGS-25297 and GHZ9), either providing signposts of AGN or strong bursts of star formation. It is plausible these sources could be genuinely dusty, but we also cannot rule out the high density nebular continuum model posted in [Katz et al. \(2024\)](#). Higher resolution spectra probing the far-UV should enable constraints on the ionized gas density in the future, enabling more detailed modeling of the origin of the red UV continuum colors.

7. SUMMARY

We present an analysis of *JWST*/NIRSpec spectra of 61 galaxies at $z = 9 - 14$, characterizing their spectroscopic properties. By comparing against the population at $6 < z < 9$, we quantify the evolution in the stellar populations, gas properties, and dust content. We summarize our key results below.

1. Using the latest publicly available NIRSpec database, we construct a sample of 61 spectroscopically confirmed galaxies at $z > 9$. Spectroscopic redshifts of 30 of these systems are newly confirmed. We measure the rest-frame UV to optical emission line properties and UV continuum slopes for subsets of the 61 galaxies, assembling a sample with size that is at least $2\times$ larger than previous studies of NIRSpec spectra of galaxies at $z > 9$ ([Roberts-Borsani et al. 2024](#); [Saxena et al. 2024](#)).

2. We derive the UV slopes of galaxies at $z > 9$ using NIRSpec prism spectra. The $z > 9$ galaxies are gener-

ally blue, with a median UV slope of $\beta = -2.33^{+0.04}_{-0.04}$. We find a flat trend between UV slopes and M_{UV} , in contrast to what has been seen at lower redshifts. At fixed M_{UV} (< -19.8), galaxies become slightly bluer between $9 < z < 11$ (median $\beta = -2.28^{+0.05}_{-0.05}$) and $z > 11$ (median $\beta = -2.48^{+0.13}_{-0.08}$). The average UV slope of $z > 11$ galaxies approaches the intrinsic value expected from stellar and nebular continuum, suggesting minimal obscuration by dust, as found in previous analysis of spectra and multi-band imaging.

3. We identify five $z > 9$ spectroscopically confirmed galaxies with red UV slopes ($\beta \gtrsim -1.5$). **BEAGLE** models infer the largest dust optical depths for these five red systems among our sample. The only two sources with Balmer line measurements reveal small Balmer decrements, providing independent evidence for modest reddening from dust. These sources may represent a population of galaxies at $z > 9$ with significant dust attenuation. Alternatively, the red colors may arise in galaxies dominated by nebular continuum emission with high enough electron densities to collisionally de-excite the two photon continuum ([Katz et al. 2024](#)). We demonstrate that the emission lines span a range of properties, suggesting a mixture of star formation histories may be linked to the red colors.

4. We quantify the evolution in the distributions of $H\beta$, C III], and C IV EWs from $z \sim 6$ to $z > 9$. Using the composite spectra, we measure that the average $H\beta$ EW and C III] EW increase by a factor of $\simeq 2$ from $z \sim 6$ to $z > 9$. The shift at the upper end of the EW distributions is similar in magnitude. We find that 23 – 31% of the $z > 9$ galaxies show extremely large EWs ($H\beta$ EW $> 240 \text{ \AA}$, C III] EW $> 20 \text{ \AA}$, or C IV EW $> 10 \text{ \AA}$), which are $2 - 3\times$ larger than that at $6 < z < 9$. We quantify the evolution in star formation histories (parameterized by $\text{SFR}_{3\text{Myr}}/\text{SFR}_{3-50\text{Myr}}$ ratios) that would be required to explain the emission line EW evolution using **BEAGLE**. The fits indicate an overall shift toward larger $\text{SFR}_{3\text{Myr}}/\text{SFR}_{3-50\text{Myr}}$ ratios, with the strongest SFR upturns becoming significantly more common between $6 < z < 9$ and $z > 9$. We discuss the connection between the shift in emission line properties and the slow evolution in the UV luminosity function at $z > 9$, commenting on how evolution and mass dependence in several quantities (σ_{UV} , SFE) may alter the inferred star formation histories.

5. We constrain the average ionized gas properties of $z > 9$ galaxies. The composite spectra indicate large ionization-sensitive line ratios ($\text{O32} = 13.4$, $\text{Ne3O2} = 0.88$), as expected if the ISM of $z > 9$ galaxies is highly ionized or has very high densities. The [O III] $\lambda 4363$ detection enables calculation of the gas-phase metallic-

ity via the direct method, revealing a moderately low gas-phase oxygen abundance of $0.08 Z_{\odot}$. The C III] and O III] measurements imply a sub-solar C/O ratio (0.44 C/O_{\odot}), consistent with the C/O – O/H trends seen at lower redshifts. The composite spectrum also presents the N IV] emission line, with line ratios suggesting nitrogen-enhanced abundance ($\text{N/O} = 1.7 \text{ N/O}_{\odot}$). At lower redshifts, this abundance pattern is found primarily in galaxies with extremely young stellar populations formed in recent bursts of star formation where high SFR surface densities are likely present. We suggest that this abundance pattern may arise more frequently at $z > 9$ as stronger bursts become more common in the galaxy population. The shift in star formation histories may also explain the increased incidence of hard ionizing agents in $z > 9$ galaxies, as seen by the prevalence of strong C IV-emitters in the existing spectroscopic database.

ACKNOWLEDGMENTS

The authors would like to thank Adèle Plat for useful discussions. We also thank Stéphane Charlot and Jacopo Chevallard for providing access to the **BEAGLE** tool used for SED fitting analysis. MT acknowledges funding from the *JWST* Arizona/Steward Postdoc in Early galaxies and Reionization (JASPER) Scholar contract at the University of Arizona. DPS acknowledges support from the National Science Foundation through the grant AST-2109066. CAM, VG, and ZC acknowledge support by the Carlsberg Foundation under grant CF22-1322. The Cosmic Dawn Center (DAWN) is funded by the Danish National Research Foundation under grant DNR140.

This work is based on observations made with the NASA/ESA/CSA *James Webb Space Telescope*. The

data were obtained from the Mikulski Archive for Space Telescopes at the Space Telescope Science Institute, which is operated by the Association of Universities for Research in Astronomy, Inc., under NASA contract NAS 5-03127 for *JWST*. These observations are associated with the following public-available programs: GTO 1180, 1181, 1210, 1286, 1287, and GO 3215 (JADES, doi: 10.17909/8tdj-8n28; Rieke, Marcia et al. 2023), ERS 1324 (GLASS, doi: 10.17909/kw3c-n857; Treu, Tommaso & Paris, Diego 2023), ERS 1345 and DDT 2750 (CEERS, doi: 10.17909/z7p0-8481; Finkelstein, Steven et al. 2023), GO 2561 (UNCOVER), GO 4233 (RUBIES), GO 6368 (CAPERS), GO 1871, GO 3073, GO 4287. The authors acknowledge the above teams led by Daniel Eisenstein & Nora Lützgendorf, K. Isaak, Tommaso Treu, Steven L. Finkelstein, Pablo Arrabal Haro, Ivo Labbé & Rachel Bezanson, Anna de Graaff & Gabriel Brammer, Mark Dickinson, John Chisholm, and Marco Castellano for developing their observing programs. Part of the data products presented herein were retrieved from the Dawn *JWST* Archive (DJA). DJA is an initiative of the Cosmic Dawn Center, which is funded by the Danish National Research Foundation under grant DNR140. This work is based in part upon High Performance Computing (HPC) resources supported by the University of Arizona TRIF, UITS, and Research, Innovation, and Impact (RII) and maintained by the UArizona Research Technologies department.

Software: NumPy (Harris et al. 2020), Matplotlib (Hunter 2007), SciPy (Virtanen et al. 2020), Astropy (Astropy Collaboration et al. 2013, 2018, 2022), BEAGLE (Chevallard & Charlot 2016), CLOUDY (Ferland et al. 2013), Prospector (Leja et al. 2019; Johnson et al. 2021), PyNeb (Luridiana et al. 2015).

APPENDIX

A. SPECTROSCOPIC SAMPLE AT $6 < z < 9$

In this section, we describe the selection of $6 < z < 9$ sample and emission line measurements. Our selection of $6 < z < 9$ galaxies largely follows our approach to identifying $z > 9$ galaxies described in Section 2 as well as our methods described in earlier papers (Tang et al. 2024b; Topping et al. 2025a). We create redshift catalogs from our reductions of NIRSpec observations in a large number of programs in the public archive (see Section 2.1). Unlike at $z > 9$, strong rest-frame optical emission lines are accessible with NIRSpec throughout the $6 < z < 9$ redshift range. Redshift confirma-

tion is typically achieved via identifications of multiple emission lines (i.e., H β , [O III], H α). We identify 393 galaxies at $6 < z < 9$ with rest-frame optical emission line detections. The precise spectroscopic redshifts of these 393 galaxies are computed by simultaneously fitting the available strong optical lines with multiple Gaussian profiles and using the fitted line centers. To maximize the sample size and avoid bias against sources with weak emission lines, we also search for objects with Ly α breaks but no emission line detections at $6 < z < 9$. We identify 8 such objects. In total we assemble the $6 < z < 9$ NIRSpec sample containing 401 galaxies.

Among the 401 galaxies in our $6 < z < 9$ sample, there are 55, 118, 73, and 155 galaxies in the Abell 2744, EGS, GOODS-N, and GOODS-S fields, respectively. 332 of these 401 galaxies have low resolution ($R \sim 100$) prism spectra. Medium resolution ($R = 1000$) grating spectra have been obtained in 243 galaxies, and 49 more galaxies have high resolution ($R = 2700$) grating spectra. There are 223 systems with both prism and grating spectra.

Using the methods introduced in Section 2.5, we measure the fluxes and EWs of the available rest-frame UV to optical emission lines in both the prism and grating spectra of galaxies in our $6 < z < 9$ sample. More details about the rest-frame optical spectra of individual systems at $6 < z < 9$ will be presented in a future paper. Here we focus on $H\beta$ emission lines and rest-frame UV lines (i.e., C III], C IV) in $6 < z < 9$ galaxies, with the goal of establishing the connection between $H\beta$ EW and UV line EW.

We detect $H\beta$ emission lines in 374 of the 401 galaxies in our $6 < z < 9$ sample. For the 332 galaxies with prism spectra, we identify $H\beta$ emission detections in 307 systems. From the prism spectra we measure a median $H\beta$ EW of 117 Å for these 307 galaxies, with 16th-84th percentiles of 59 Å and 229 Å, respectively. For the 292 galaxies with medium or high resolution grating spectra, we detect $H\beta$ emission lines in 252 objects. For these 252 systems we measure that the 16th-50th-84th percentiles of $H\beta$ EW are 43 Å, 104 Å, and 237 Å, respectively. There are 185 galaxies at $6 < z < 9$ with $H\beta$ detections in both prism and grating spectra. We find that the $H\beta$ fluxes and EWs measured from both spectra for these 185 objects are consistent, with a standard deviation of the difference between both EWs just $\simeq 0.05$ dex. Combining the $H\beta$ EW measurements from prism and grating spectra, the overall $H\beta$ EW distribution of the 374 galaxies with $H\beta$ detections in our $6 < z < 9$ sample has 16th-50th-84th percentiles of 53 Å, 112 Å, and 230 Å.

C III] emission lines are detected ($S/N > 3$) in 48 galaxies at $6 < z < 9$. We identify C III] detections in the prism spectra of 24 galaxies, with 16th-50th-84th percentiles of C III] EW of 10 Å, 15 Å, and 33 Å, respectively. For galaxies with medium or high resolution grating spectra, we detect C III] emission in 30 systems, with 16th-50th-84th percentiles of C III] EW of 8 Å, 14 Å, and 32 Å. Six galaxies have C III] detections in both their prism and grating spectra. The C III] emission line fluxes and EWs measured from both spectra for these six galaxies are broadly consistent, with a standard deviation of the difference between both EWs

$\simeq 0.13$ dex. For the vast majority of galaxies in our $6 < z < 9$ sample that we do not detect C III] emission (332 systems), we place 3σ upper limits to their C III] EWs. The median 3σ upper limits of C III] EWs derived from prism and grating spectra are 33 Å and 36 Å, respectively.

We identify C IV emission detections in the NIRSpec spectra of 7 galaxies in our $6 < z < 9$ sample. We measure C IV EWs of these seven galaxies ranging from 3.8 Å to 49 Å, with a median C IV EW of 12 Å. C IV measurements of six of these seven systems at $6 < z < 9$ have been reported in literature previously (CEERS-397, JADES-GN-954, JADES-GS-13041, JADES-GN-1899, UNCOVER-10646, CEERS-1019; Fujimoto et al. 2024; Tang et al. 2024a,b; Topping et al. 2025a; Witstok et al. 2025b). We newly-identify C IV emission detection in CEERS-1027 (R.A. = 214.88300, Decl. = 52.84042). The redshift of CEERS-1027 ($z = 7.819$) was first confirmed from the CEERS observations using the medium resolution ($R = 1000$) NIRSpec grating spectra (Heintz et al. 2023; Nakajima et al. 2023; Tang et al. 2023; Sanders et al. 2024). GO 4287 program has obtained high resolution ($R = 2700$) rest-frame UV (G140H/F100LP) spectrum for CEERS-1027. We detect C IV doublet emission lines from the GO 4287 G140H spectrum, with a total EW of 3.8 ± 1.0 Å.

Finally, to investigate how the average spectroscopic properties change with redshift and $H\beta$ EW, we create composite $6 < z < 9$ spectra. We first stack individual prism spectra binning by redshift. We group systems at $6 < z < 7$ (median $z \simeq 6.5$), $7 < z < 8$ (median $z \simeq 7.5$), and $8 < z < 9$ (median $z \simeq 8.5$), with each bin containing 181, 109, and 42 galaxies, respectively. Composite spectra are stacked following the same procedures described in Section 2.3 for the $z > 9$ composite. We also create composites of the prism spectra binning by $H\beta$ EW. To do so, we group galaxies with $H\beta$ EW = 10–80 Å (median 61 Å), 80–150 Å (median 114 Å), 150–230 Å (median 187 Å), 230–500 Å (median 258 Å). The four groups have 99, 103, 56, and 49 galaxies, respectively. The composite spectra of our $6 < z < 9$ galaxies binning by $H\beta$ EW are shown in Figure 9. We measure the available emission line properties from the composite spectra with the same methods described in Section 2.5.

B. TABLE AND NIRSPEC SPECTRA OF GALAXIES AT $z > 9$

Table B1. NIRSpc spectroscopically confirmed galaxies at $z > 9$.

ID	PID	R.A.	Decl.	z_{spec}	M_{UV}	β	$\text{EW}_{\text{CIII}\lambda}$ (Å)	EW_{CIV} (Å)	Ref.
CAPERS-EGS-94554	6368	214.877988	52.856067	9.01	-18.84	-2.45 ± 0.50	< 47	< 58	
RUBIES-EGS-952693	4233	214.977359	52.926498	9.03	-20.47	-2.06 ± 0.28	< 30	< 29	
JADES-GS-20077159	1286	53.133607	-27.844892	9.05	-20.39	-1.47 ± 0.20	11 ± 5	< 22	
JADES-GN-619	1181	189.158251	62.221361	9.07	-19.99	-2.27 ± 0.03	< 6	< 22	(17)
JADES-GS-20083087	1286	53.067692	-27.837861	9.07	-19.52	-2.12 ± 0.13	< 17	< 46	
RUBIES-EGS-929993	4233	215.125158	52.986532	9.17	-19.14	-1.36 ± 0.18	< 53	< 67	
JADES-GN-17858	1181	189.142208	62.284594	9.21	-19.89	-2.06 ± 0.14	< 27	34 ± 13	(17)
CAPERS-UDS-28597	6368	34.465142	-5.217735	9.21	-20.58	-2.18 ± 0.17	18 ± 8	< 20	
CAPERS-UDS-146485	6368	34.249791	-5.142105	9.26	-20.18	-2.59 ± 0.27	24 ± 12	< 37	
CAPERS-UDS-142042	6368	34.249398	-5.130833	9.26	-20.20	
CAPERS-UDS-22431	6368	34.460257	-5.185003	9.27	-20.37	-2.56 ± 0.11	14 ± 4	< 9	(21)
CAPERS-UDS-127376	6368	34.436059	-5.101416	9.27	-19.81	-2.29 ± 0.26	< 34	< 32	
CAPERS-COSMOS-118821	6368	150.090314	2.306922	9.30	-19.66	-2.21 ± 0.19	< 21	< 26	
JADES-GN-19715	1181	189.138322	62.289869	9.30	-20.13	-2.88 ± 0.29	< 27	< 27	(17)
RUBIES-UDS-29385	4233	34.434963	-5.271119	9.31	-20.58	-2.39 ± 0.28	< 23	< 37	
UNCOVER-3686	2561	3.617199	-30.425536	9.32	-21.71	-2.12 ± 0.08	< 7	< 4	(8,13)
GN-z9p4	1181	189.016992	62.241585	9.38	-20.69	-2.14 ± 0.15	< 10	< 10	(16)
CAPERS-EGS-87132	6368	215.044034	52.994331	9.38	-18.87	-2.22 ± 0.14	34 ± 7	< 24	(21)
GS-z9-0	3215	53.112436	-27.774619	9.43	-19.54	-2.60 ± 0.06	12 ± 1	4 ± 1	(4,9,18)
JADES-GS-20064312	1287	53.072431	-27.855456	9.44	-17.22	-1.17 ± 0.28	< 48	< 53	
GLASS-83338	3073	3.454686	-30.316832	9.53	-19.06	-1.80 ± 0.47	< 69	< 28	(20)
UNCOVER-22223	2561	3.568115	-30.383051	9.57	-17.28	-1.99 ± 0.15	26 ± 7	25 ± 5	(13)
JADES-GN-59720	1181	189.239795	62.210830	9.63	-19.70	-3.00 ± 0.28	< 16	< 25	(17)
JADES-GS-20088041	1286	53.175514	-27.780606	9.68	-20.14	-1.96 ± 0.11	41 ± 13	< 36	
JADES-GN-80088	1181	189.239122	62.210934	9.74	-20.15	-2.09 ± 0.26	< 29	< 37	(17)
JADES-GN-55757	1181	189.217683	62.199490	9.74	-19.86	-2.51 ± 0.17	18 ± 3	10 ± 4	(17,21)
CEERS-80026	1345	214.811848	52.737113	9.75	-20.08	-1.73 ± 0.43	< 12	< 8	(1)
CAPERS-COSMOS-52185	6368	150.116572	2.197038	9.80	-21.82	-2.33 ± 0.18	16 ± 8	< 12	
UNCOVER-13151	2561	3.592505	-30.401463	9.80	-17.46	-2.46 ± 0.43	< 27	< 22	(13)
JADES-GS-20076576	1286	53.055108	-27.845593	9.90	-19.04	-2.53 ± 0.32	< 14	< 26	
JADES-GN-11508	1181	189.184460	62.262491	9.93	-19.64	-2.64 ± 0.07	26 ± 10	< 40	(17)
CAPERS-EGS-25297	6368	214.817153	52.748305	9.95	-19.96	-1.53 ± 0.12	28 ± 8	< 23	(21)
UNCOVER-26185	2561	3.567071	-30.377862	10.06	-18.93	-2.36 ± 0.17	36 ± 12	< 14	(6,13)
CEERS-64	2750	214.922774	52.911525	10.07	-19.47	-2.20 ± 0.38	< 14	< 13	(2)
GLASS-z11-17225	3073	3.507323	-30.343183	10.07	-19.06	-2.67 ± 0.01	< 36	< 83	(20)
GHZ9	3073	3.478735	-30.345495	10.16	-19.80	-1.45 ± 0.07	24 ± 7	76 ± 7	(15,20)
GHZ8	3073	3.451447	-30.321795	10.23	-20.37	-2.36 ± 0.07	< 14	< 13	(20)
CEERS-80041	1345	214.732534	52.758092	10.23	-20.37	-2.45 ± 0.04	< 10	< 9	(1)
CAPERS-COSMOS-109917	6368	150.142945	2.288012	10.28	-19.62	-2.84 ± 0.28	20 ± 6	36 ± 8	
UNCOVER-37126	2561	3.590110	-30.359742	10.39	-19.80	-2.67 ± 0.11	< 8	< 7	(13)
GS-z10-0	1210	53.158837	-27.773500	10.39	-18.05	-2.38 ± 0.04	< 31	< 22	(5,9)

Table B1 *continued*

Table B1 (*continued*)

ID	PID	R.A.	Decl.	z_{spec}	M_{UV}	β	EW_{CIII} (Å)	EW_{CIV} (Å)	Ref.
CAPERS-UDS-z10	6368	34.456023	-5.121952	10.44	-19.90	-2.64 ± 0.26	19 ± 10	< 16	(19)
GHZ7	3073	3.451347	-30.320738	10.44	-19.84	-2.22 ± 0.07	24 ± 6	< 52	(20)
JADES-GS-20176151	1287	53.070746	-27.865487	10.53	-19.08	-2.11 ± 0.17	< 10	< 15	
GN-z11	1181	189.106056	62.242052	10.60	-21.89	-2.38 ± 0.13	16 ± 3	6 ± 2	(3)
GHZ4	3073	3.513717	-30.351564	10.72	-19.50	-2.26 ± 0.16	19 ± 11	< 55	(20)
JADES-GS-20177294	1287	53.078997	-27.863582	10.89	-17.65	-2.34 ± 0.55	< 63	< 62	
CAPERS-UDS-z11	6368	34.264455	-5.096191	11.06	-20.41	-2.38 ± 0.31	< 21	< 26	(19)
JADES-GS-20021387	1287	53.067147	-27.883190	11.06	-18.33	-1.85 ± 0.15	< 23	< 29	
JADES-GS-20015720	1287	53.117610	-27.888327	11.26	-19.88	-2.67 ± 0.12	15 ± 5	9 ± 4	
CEERS-10	2750	214.906630	52.945507	11.39	-20.18	-2.02 ± 0.32	< 19	< 21	(2)
CEERS-1	2750	214.943138	52.942444	11.55	-20.07	-2.71 ± 0.29	< 20	< 12	(2)
GS-z11-0	1210	53.164768	-27.774627	11.55	-19.46	-2.20 ± 0.27	< 18	< 12	(5,9,14)
GHZ2	3073	3.498971	-30.324734	12.34	-20.93	-2.58 ± 0.14	21 ± 4	47 ± 3	(11)
UNCOVER-38766	2561	3.513562	-30.356798	12.39	-18.91	-2.35 ± 0.03	< 38	< 14	(7,13)
GS-z12-0	3215	53.166346	-27.821558	12.51	-19.03	-2.19 ± 0.11	29 ± 7	< 40	(5,9,12)
UNCOVER-13077	2561	3.570886	-30.401556	13.05	-19.22	-2.35 ± 0.23	< 57	< 32	(7)
JADES-GS-z13-1-LA	1287	53.064771	-27.890294	13.06	-18.27	-2.87 ± 0.27	< 19	< 70	(22)
GS-z13-0	3215	53.149886	-27.776504	13.22	-18.78	-2.64 ± 0.39	< 45	< 17	(5,9,14)
GS-z14-1	1287	53.074245	-27.885980	14.04	-18.79	-2.85 ± 0.29	< 23	< 23	(10)
GS-z14-0	1287	53.082917	-27.855628	14.22	-20.99	-2.19 ± 0.14	7 ± 2	< 9	(10)

NOTE—References: (1) Arrabal Haro et al. (2023a); (2) Arrabal Haro et al. (2023b); (3) Bunker et al. (2023); (4) Cameron et al. (2023b); (5) Curtis-Lake et al. (2023); (6) Goulding et al. (2023); (7) Wang et al. (2023); (8) Boyett et al. (2024b); (9) Bunker et al. (2024); (10) Carniani et al. (2024); (11) Castellano et al. (2024); (12) D’Eugenio et al. (2024); (13) Fujimoto et al. (2024); (14) Hainline et al. (2024b); (15) Napolitano et al. (2024); (16) Schaerer et al. (2024); (17) Tang et al. (2024b); (18) Curti et al. (2025); (19) Kokorev et al. (2025); (20) Napolitano et al. (2025); (21) Pollock et al. (2025); (22) Witstok et al. (2025a).

REFERENCES

- Adams, N. J., Conselice, C. J., Ferreira, L., et al. 2023, MNRAS, 518, 4755, doi: [10.1093/mnras/stac3347](https://doi.org/10.1093/mnras/stac3347)
- Adams, N. J., Conselice, C. J., Austin, D., et al. 2024, ApJ, 965, 169, doi: [10.3847/1538-4357/ad2a7b](https://doi.org/10.3847/1538-4357/ad2a7b)
- Akerman, C. J., Carigi, L., Nissen, P. E., Pettini, M., & Asplund, M. 2004, A&A, 414, 931, doi: [10.1051/0004-6361:20034188](https://doi.org/10.1051/0004-6361:20034188)
- Amorín, R., Fontana, A., Pérez-Montero, E., et al. 2017, Nature Astronomy, 1, 0052, doi: [10.1038/s41550-017-0052](https://doi.org/10.1038/s41550-017-0052)
- Arellano-Córdova, K. Z., Berg, D. A., Chisholm, J., et al. 2022, ApJL, 940, L23, doi: [10.3847/2041-8213/ac9ab2](https://doi.org/10.3847/2041-8213/ac9ab2)
- Arrabal Haro, P., Dickinson, M., Finkelstein, S. L., et al. 2023a, ApJL, 951, L22, doi: [10.3847/2041-8213/acdd54](https://doi.org/10.3847/2041-8213/acdd54)
- . 2023b, Nature, 622, 707, doi: [10.1038/s41586-023-06521-7](https://doi.org/10.1038/s41586-023-06521-7)
- Asplund, M., Grevesse, N., Sauval, A. J., & Scott, P. 2009, ARA&A, 47, 481, doi: [10.1146/annurev.astro.46.060407.145222](https://doi.org/10.1146/annurev.astro.46.060407.145222)
- Astropy Collaboration, Robitaille, T. P., Tollerud, E. J., et al. 2013, A&A, 558, A33, doi: [10.1051/0004-6361/201322068](https://doi.org/10.1051/0004-6361/201322068)
- Astropy Collaboration, Price-Whelan, A. M., Sipőcz, B. M., et al. 2018, AJ, 156, 123, doi: [10.3847/1538-3881/aabc4f](https://doi.org/10.3847/1538-3881/aabc4f)
- Astropy Collaboration, Price-Whelan, A. M., Lim, P. L., et al. 2022, ApJ, 935, 167, doi: [10.3847/1538-4357/ac7c74](https://doi.org/10.3847/1538-4357/ac7c74)
- Austin, D., Conselice, C. J., Adams, N. J., et al. 2024, arXiv e-prints, arXiv:2404.10751, doi: [10.48550/arXiv.2404.10751](https://doi.org/10.48550/arXiv.2404.10751)
- Bayliss, M. B., Rigby, J. R., Sharon, K., et al. 2014, ApJ, 790, 144, doi: [10.1088/0004-637X/790/2/144](https://doi.org/10.1088/0004-637X/790/2/144)

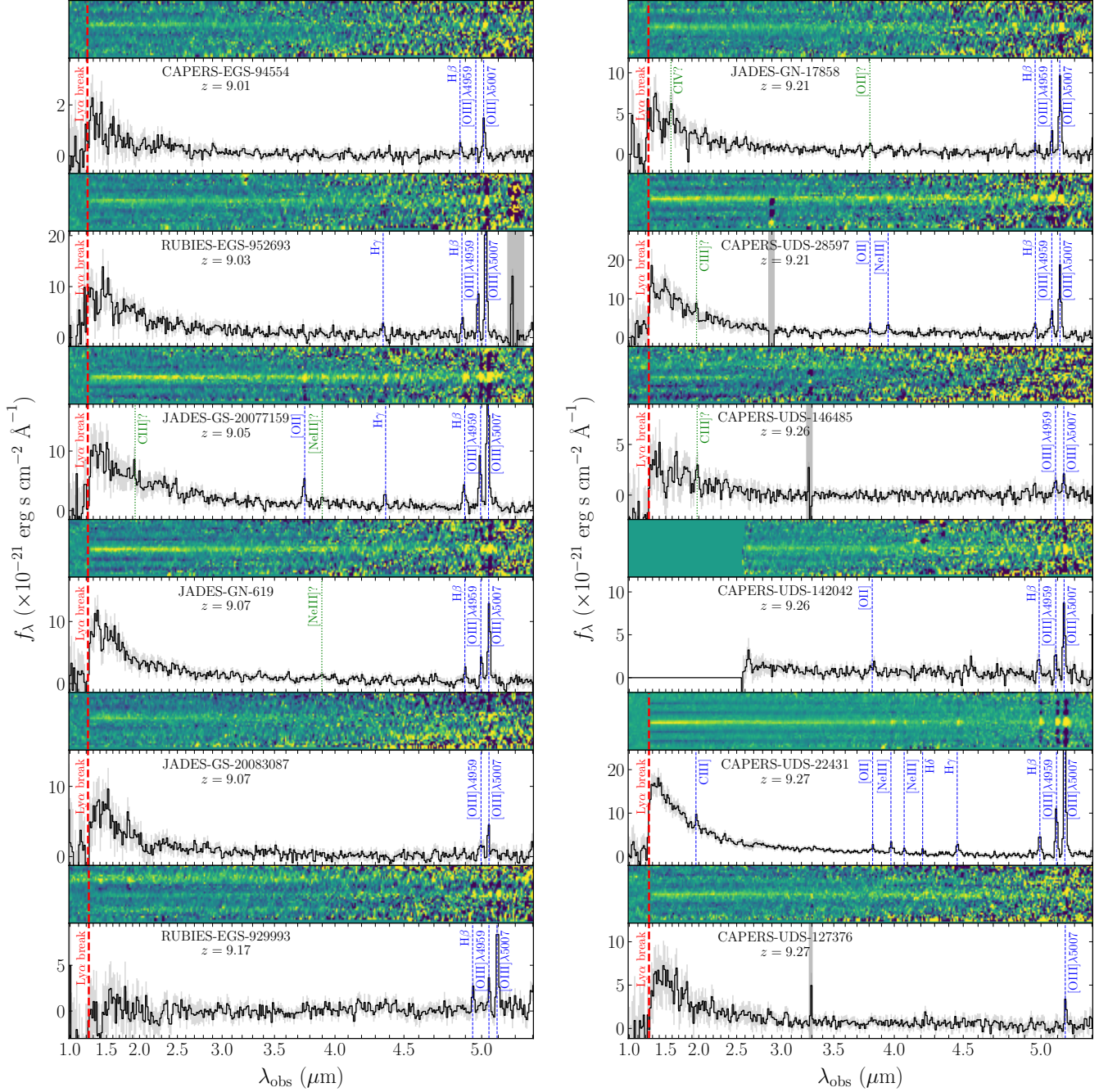
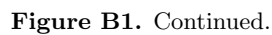


Figure B1. NIRSpect prism spectra of the 30 newly identified galaxies at $z > 9$. For each object, the top panel shows the 2D spectrum and the bottom panels shows the 1D spectrum. We mark detected emission lines ($S/N > 3$) with blue dashed lines and tentative detections ($S/N = 2 - 3$) with green dotted lines. Spectra contaminated by noise pixels are masked by grey shaded regions.



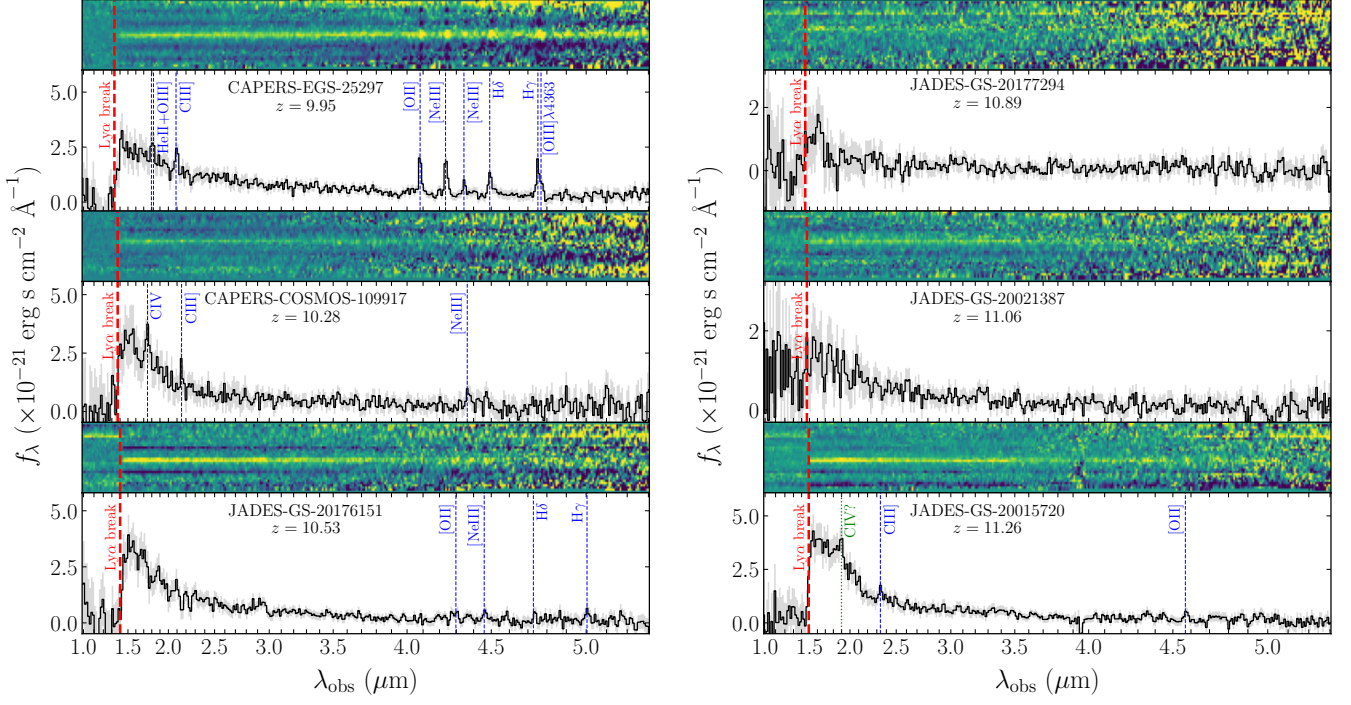


Figure B1. Continued.

- Begley, R., McLure, R. J., Cullen, F., et al. 2025, MNRAS, 537, 3245, doi: [10.1093/mnras/staf211](https://doi.org/10.1093/mnras/staf211)
- Bensby, T., & Feltzing, S. 2006, MNRAS, 367, 1181, doi: [10.1111/j.1365-2966.2006.10037.x](https://doi.org/10.1111/j.1365-2966.2006.10037.x)
- Berg, D. A., Erb, D. K., Auger, M. W., Pettini, M., & Brammer, G. B. 2018, ApJ, 859, 164, doi: [10.3847/1538-4357/aab7fa](https://doi.org/10.3847/1538-4357/aab7fa)
- Berg, D. A., Erb, D. K., Henry, R. B. C., Skillman, E. D., & McQuinn, K. B. W. 2019, ApJ, 874, 93, doi: [10.3847/1538-4357/ab020a](https://doi.org/10.3847/1538-4357/ab020a)
- Berg, D. A., Skillman, E. D., Henry, R. B. C., Erb, D. K., & Carigi, L. 2016, ApJ, 827, 126, doi: [10.3847/0004-637X/827/2/126](https://doi.org/10.3847/0004-637X/827/2/126)
- Bezanson, R., Labbe, I., Whitaker, K. E., et al. 2024, ApJ, 974, 92, doi: [10.3847/1538-4357/ad66cf](https://doi.org/10.3847/1538-4357/ad66cf)
- Böker, T., Beck, T. L., Birkmann, S. M., et al. 2023, PASP, 135, 038001, doi: [10.1088/1538-3873/acb846](https://doi.org/10.1088/1538-3873/acb846)
- Bouwens, R. J., Illingworth, G. D., Oesch, P. A., et al. 2010, ApJL, 708, L69, doi: [10.1088/2041-8205/708/2/L69](https://doi.org/10.1088/2041-8205/708/2/L69)
- Bouwens, R. J., Stefanon, M., Brammer, G., et al. 2023, MNRAS, 523, 1036, doi: [10.1093/mnras/stad1145](https://doi.org/10.1093/mnras/stad1145)
- Boyet, K., Bunker, A. J., Curtis-Lake, E., et al. 2024a, MNRAS, 535, 1796, doi: [10.1093/mnras/stae2430](https://doi.org/10.1093/mnras/stae2430)
- Boyet, K., Trenti, M., Leethochawalit, N., et al. 2024b, Nature Astronomy, 8, 657, doi: [10.1038/s41550-024-02218-7](https://doi.org/10.1038/s41550-024-02218-7)
- Bruzual, G., & Charlot, S. 2003, MNRAS, 344, 1000, doi: [10.1046/j.1365-8711.2003.06897.x](https://doi.org/10.1046/j.1365-8711.2003.06897.x)
- Bunker, A. J., Saxena, A., Cameron, A. J., et al. 2023, A&A, 677, A88, doi: [10.1051/0004-6361/202346159](https://doi.org/10.1051/0004-6361/202346159)
- Bunker, A. J., Cameron, A. J., Curtis-Lake, E., et al. 2024, A&A, 690, A288, doi: [10.1051/0004-6361/202347094](https://doi.org/10.1051/0004-6361/202347094)
- Bushouse, H., Eisenhamer, J., Dencheva, N., et al. 2024, JWST Calibration Pipeline, 1.16.1, Zenodo, doi: [10.5281/zenodo.6984365](https://doi.org/10.5281/zenodo.6984365)
- Byler, N., Dalcanton, J. J., Conroy, C., & Johnson, B. D. 2017, ApJ, 840, 44, doi: [10.3847/1538-4357/aa6c66](https://doi.org/10.3847/1538-4357/aa6c66)
- Caffau, E., Ludwig, H. G., Steffen, M., Freytag, B., & Bonifacio, P. 2011, SoPh, 268, 255, doi: [10.1007/s11207-010-9541-4](https://doi.org/10.1007/s11207-010-9541-4)
- Calzetti, D., Kinney, A. L., & Storchi-Bergmann, T. 1994, ApJ, 429, 582, doi: [10.1086/174346](https://doi.org/10.1086/174346)
- Cameron, A. J., Katz, H., Rey, M. P., & Saxena, A. 2023a, MNRAS, 523, 3516, doi: [10.1093/mnras/stad1579](https://doi.org/10.1093/mnras/stad1579)
- Cameron, A. J., Katz, H., Witten, C., et al. 2024, MNRAS, 534, 523, doi: [10.1093/mnras/stae1547](https://doi.org/10.1093/mnras/stae1547)
- Cameron, A. J., Saxena, A., Bunker, A. J., et al. 2023b, A&A, 677, A115, doi: [10.1051/0004-6361/202346107](https://doi.org/10.1051/0004-6361/202346107)
- Campbell, A., Terlevich, R., & Melnick, J. 1986, MNRAS, 223, 811, doi: [10.1093/mnras/223.4.811](https://doi.org/10.1093/mnras/223.4.811)
- Cardelli, J. A., Clayton, G. C., & Mathis, J. S. 1989, ApJ, 345, 245, doi: [10.1086/167900](https://doi.org/10.1086/167900)

- Carnall, A. C., Leja, J., Johnson, B. D., et al. 2019, *ApJ*, 873, 44, doi: [10.3847/1538-4357/ab04a2](https://doi.org/10.3847/1538-4357/ab04a2)
- Carniani, S., Hainline, K., D'Eugenio, F., et al. 2024, *Nature*, 633, 318, doi: [10.1038/s41586-024-07860-9](https://doi.org/10.1038/s41586-024-07860-9)
- Casey, C. M., Akins, H. B., Shuntov, M., et al. 2024, *ApJ*, 965, 98, doi: [10.3847/1538-4357/ad2075](https://doi.org/10.3847/1538-4357/ad2075)
- Castellano, M., Fontana, A., Treu, T., et al. 2022, *ApJL*, 938, L15, doi: [10.3847/2041-8213/ac94d0](https://doi.org/10.3847/2041-8213/ac94d0)
- . 2023, *ApJL*, 948, L14, doi: [10.3847/2041-8213/accea5](https://doi.org/10.3847/2041-8213/accea5)
- Castellano, M., Napolitano, L., Fontana, A., et al. 2024, *ApJ*, 972, 143, doi: [10.3847/1538-4357/ad5f88](https://doi.org/10.3847/1538-4357/ad5f88)
- Chabrier, G. 2003, *PASP*, 115, 763, doi: [10.1086/376392](https://doi.org/10.1086/376392)
- Charbonnel, C., Schaerer, D., Prantzos, N., et al. 2023, *A&A*, 673, L7, doi: [10.1051/0004-6361/202346410](https://doi.org/10.1051/0004-6361/202346410)
- Chevallard, J., & Charlot, S. 2016, *MNRAS*, 462, 1415, doi: [10.1093/mnras/stw1756](https://doi.org/10.1093/mnras/stw1756)
- Chisholm, J., Berg, D. A., Endsley, R., et al. 2024, *MNRAS*, 534, 2633, doi: [10.1093/mnras/stae2199](https://doi.org/10.1093/mnras/stae2199)
- Christensen, L., Laursen, P., Richard, J., et al. 2012, *MNRAS*, 427, 1973, doi: [10.1111/j.1365-2966.2012.22007.x](https://doi.org/10.1111/j.1365-2966.2012.22007.x)
- Citro, A., Berg, D. A., Erb, D. K., et al. 2024, *ApJ*, 969, 148, doi: [10.3847/1538-4357/ad4600](https://doi.org/10.3847/1538-4357/ad4600)
- Clarke, L., Shapley, A. E., Sanders, R. L., et al. 2024, *ApJ*, 977, 133, doi: [10.3847/1538-4357/ad8ba4](https://doi.org/10.3847/1538-4357/ad8ba4)
- Conroy, C., Gunn, J. E., & White, M. 2009, *ApJ*, 699, 486, doi: [10.1088/0004-637X/699/1/486](https://doi.org/10.1088/0004-637X/699/1/486)
- Conroy, C., White, M., & Gunn, J. E. 2010, *ApJ*, 708, 58, doi: [10.1088/0004-637X/708/1/58](https://doi.org/10.1088/0004-637X/708/1/58)
- Cooke, R., Pettini, M., Steidel, C. C., Rudie, G. C., & Jorgenson, R. A. 2011, *MNRAS*, 412, 1047, doi: [10.1111/j.1365-2966.2010.17966.x](https://doi.org/10.1111/j.1365-2966.2010.17966.x)
- Cullen, F., McLure, R. J., Khochfar, S., Dunlop, J. S., & Dalla Vecchia, C. 2017, *MNRAS*, 470, 3006, doi: [10.1093/mnras/stx1451](https://doi.org/10.1093/mnras/stx1451)
- Cullen, F., McLure, R. J., McLeod, D. J., et al. 2023, *MNRAS*, 520, 14, doi: [10.1093/mnras/stad073](https://doi.org/10.1093/mnras/stad073)
- Cullen, F., McLeod, D. J., McLure, R. J., et al. 2024, *MNRAS*, 531, 997, doi: [10.1093/mnras/stae1211](https://doi.org/10.1093/mnras/stae1211)
- Curti, M., Witstok, J., Jakobsen, P., et al. 2025, *A&A*, 697, A89, doi: [10.1051/0004-6361/202451410](https://doi.org/10.1051/0004-6361/202451410)
- Curtis-Lake, E., Carniani, S., Cameron, A., et al. 2023, *Nature Astronomy*, 7, 622, doi: [10.1038/s41550-023-01918-w](https://doi.org/10.1038/s41550-023-01918-w)
- de Graaff, A., Brammer, G., Weibel, A., et al. 2025, *A&A*, 697, A189, doi: [10.1051/0004-6361/202452186](https://doi.org/10.1051/0004-6361/202452186)
- Dekel, A., Sari, R., & Ceverino, D. 2009, *ApJ*, 703, 785, doi: [10.1088/0004-637X/703/1/785](https://doi.org/10.1088/0004-637X/703/1/785)
- Dekel, A., Sarkar, K. C., Birnboim, Y., Mandelker, N., & Li, Z. 2023, *MNRAS*, 523, 3201, doi: [10.1093/mnras/stad1557](https://doi.org/10.1093/mnras/stad1557)
- D'Eugenio, F., Maiolino, R., Carniani, S., et al. 2024, *A&A*, 689, A152, doi: [10.1051/0004-6361/202348636](https://doi.org/10.1051/0004-6361/202348636)
- D'Eugenio, F., Cameron, A. J., Scholtz, J., et al. 2025, *ApJS*, 277, 4, doi: [10.3847/1538-4365/ada148](https://doi.org/10.3847/1538-4365/ada148)
- Donnan, C. T., McLeod, D. J., Dunlop, J. S., et al. 2023, *MNRAS*, 518, 6011, doi: [10.1093/mnras/stac3472](https://doi.org/10.1093/mnras/stac3472)
- Donnan, C. T., McLure, R. J., Dunlop, J. S., et al. 2024, *MNRAS*, 533, 3222, doi: [10.1093/mnras/stae2037](https://doi.org/10.1093/mnras/stae2037)
- Eisenstein, D. J., Willott, C., Alberts, S., et al. 2023a, *arXiv e-prints*, arXiv:2306.02465, doi: [10.48550/arXiv.2306.02465](https://doi.org/10.48550/arXiv.2306.02465)
- Eisenstein, D. J., Johnson, B. D., Robertson, B., et al. 2023b, *arXiv e-prints*, arXiv:2310.12340, doi: [10.48550/arXiv.2310.12340](https://doi.org/10.48550/arXiv.2310.12340)
- Endsley, R., Chisholm, J., Stark, D. P., Topping, M. W., & Whitler, L. 2024a, *arXiv e-prints*, arXiv:2410.01905, doi: [10.48550/arXiv.2410.01905](https://doi.org/10.48550/arXiv.2410.01905)
- Endsley, R., Stark, D. P., Whitler, L., et al. 2024b, *MNRAS*, 533, 1111, doi: [10.1093/mnras/stae1857](https://doi.org/10.1093/mnras/stae1857)
- Erb, D. K., Pettini, M., Shapley, A. E., et al. 2010, *ApJ*, 719, 1168, doi: [10.1088/0004-637X/719/2/1168](https://doi.org/10.1088/0004-637X/719/2/1168)
- Esteban, C., Bresolin, F., Peimbert, M., et al. 2009, *ApJ*, 700, 654, doi: [10.1088/0004-637X/700/1/654](https://doi.org/10.1088/0004-637X/700/1/654)
- Esteban, C., García-Rojas, J., Carigi, L., et al. 2014, *MNRAS*, 443, 624, doi: [10.1093/mnras/stu1177](https://doi.org/10.1093/mnras/stu1177)
- Esteban, C., Peimbert, M., García-Rojas, J., et al. 2004, *MNRAS*, 355, 229, doi: [10.1111/j.1365-2966.2004.08313.x](https://doi.org/10.1111/j.1365-2966.2004.08313.x)
- Feldmann, R., Boylan-Kolchin, M., Bullock, J. S., et al. 2025, *MNRAS*, 536, 988, doi: [10.1093/mnras/stae2633](https://doi.org/10.1093/mnras/stae2633)
- Ferland, G. J., Porter, R. L., van Hoof, P. A. M., et al. 2013, *RMxAA*, 49, 137, doi: [10.48550/arXiv.1302.4485](https://doi.org/10.48550/arXiv.1302.4485)
- Ferrara, A., Pallottini, A., & Dayal, P. 2023, *MNRAS*, 522, 3986, doi: [10.1093/mnras/stad1095](https://doi.org/10.1093/mnras/stad1095)
- Ferrara, A., Pallottini, A., & Sommovigo, L. 2025, *A&A*, 694, A286, doi: [10.1051/0004-6361/202452707](https://doi.org/10.1051/0004-6361/202452707)
- Ferruit, P., Jakobsen, P., Giardino, G., et al. 2022, *A&A*, 661, A81, doi: [10.1051/0004-6361/202142673](https://doi.org/10.1051/0004-6361/202142673)
- Finkelstein, S. L., Papovich, C., Salmon, B., et al. 2012, *ApJ*, 756, 164, doi: [10.1088/0004-637X/756/2/164](https://doi.org/10.1088/0004-637X/756/2/164)
- Finkelstein, S. L., Bagley, M. B., Ferguson, H. C., et al. 2023, *ApJL*, 946, L13, doi: [10.3847/2041-8213/acade4](https://doi.org/10.3847/2041-8213/acade4)
- Finkelstein, S. L., Leung, G. C. K., Bagley, M. B., et al. 2024, *ApJL*, 969, L2, doi: [10.3847/2041-8213/ad4495](https://doi.org/10.3847/2041-8213/ad4495)
- Finkelstein, S. L., Bagley, M. B., Arrabal Haro, P., et al. 2025, *ApJL*, 983, L4, doi: [10.3847/2041-8213/adbbd3](https://doi.org/10.3847/2041-8213/adbbd3)

- Finkelstein, Steven, Bagley, Micaela, & Yang, Guang. 2023, Data from The Cosmic Evolution Early Release Science Survey (CEERS), STScI/MAST, doi: [10.17909/Z7P0-8481](https://doi.org/10.17909/Z7P0-8481)
- Flury, S. R., Arellano-Córdova, K. Z., Moran, E. C., & Einsig, A. 2024, arXiv e-prints, arXiv:2412.06763, doi: [10.48550/arXiv.2412.06763](https://doi.org/10.48550/arXiv.2412.06763)
- Franco, M., Akins, H. B., Casey, C. M., et al. 2024, ApJ, 973, 23, doi: [10.3847/1538-4357/ad5e6a](https://doi.org/10.3847/1538-4357/ad5e6a)
- Fujimoto, S., Wang, B., Weaver, J. R., et al. 2024, ApJ, 977, 250, doi: [10.3847/1538-4357/ad9027](https://doi.org/10.3847/1538-4357/ad9027)
- Furtak, L. J., Zitrin, A., Weaver, J. R., et al. 2023, MNRAS, 523, 4568, doi: [10.1093/mnras/stad1627](https://doi.org/10.1093/mnras/stad1627)
- García-Rojas, J., & Esteban, C. 2007, ApJ, 670, 457, doi: [10.1086/521871](https://doi.org/10.1086/521871)
- García-Rojas, J., Esteban, C., Peimbert, A., et al. 2005, MNRAS, 362, 301, doi: [10.1111/j.1365-2966.2005.09302.x](https://doi.org/10.1111/j.1365-2966.2005.09302.x)
- García-Rojas, J., Esteban, C., Peimbert, M., et al. 2004, ApJS, 153, 501, doi: [10.1086/421909](https://doi.org/10.1086/421909)
- Gardner, J. P., Mather, J. C., Abbott, R., et al. 2023, PASP, 135, 068001, doi: [10.1088/1538-3873/acd1b5](https://doi.org/10.1088/1538-3873/acd1b5)
- Garnett, D. R. 1992, AJ, 103, 1330, doi: [10.1086/116146](https://doi.org/10.1086/116146)
- Garnett, D. R., Skillman, E. D., Dufour, R. J., et al. 1995, ApJ, 443, 64, doi: [10.1086/175503](https://doi.org/10.1086/175503)
- Gehrels, N. 1986, ApJ, 303, 336, doi: [10.1086/164079](https://doi.org/10.1086/164079)
- Gelli, V., Mason, C., & Hayward, C. C. 2024, ApJ, 975, 192, doi: [10.3847/1538-4357/ad7b36](https://doi.org/10.3847/1538-4357/ad7b36)
- Gelli, V., Pallottini, A., Salvadori, S., et al. 2025, ApJ, 985, 126, doi: [10.3847/1538-4357/adc722](https://doi.org/10.3847/1538-4357/adc722)
- Goulding, A. D., Greene, J. E., Setton, D. J., et al. 2023, ApJL, 955, L24, doi: [10.3847/2041-8213/acf7c5](https://doi.org/10.3847/2041-8213/acf7c5)
- Greene, J. E., Strader, J., & Ho, L. C. 2020, ARA&A, 58, 257, doi: [10.1146/annurev-astro-032620-021835](https://doi.org/10.1146/annurev-astro-032620-021835)
- Gustafsson, B., Karlsson, T., Olsson, E., Edvardsson, B., & Ryde, N. 1999, A&A, 342, 426, doi: [10.48550/arXiv.astro-ph/9811303](https://doi.org/10.48550/arXiv.astro-ph/9811303)
- Gutkin, J., Charlot, S., & Bruzual, G. 2016, MNRAS, 462, 1757, doi: [10.1093/mnras/stw1716](https://doi.org/10.1093/mnras/stw1716)
- Hainline, K. N., Johnson, B. D., Robertson, B., et al. 2024a, ApJ, 964, 71, doi: [10.3847/1538-4357/ad1ee4](https://doi.org/10.3847/1538-4357/ad1ee4)
- Hainline, K. N., D'Eugenio, F., Jakobsen, P., et al. 2024b, ApJ, 976, 160, doi: [10.3847/1538-4357/ad8447](https://doi.org/10.3847/1538-4357/ad8447)
- Harikane, Y., Ouchi, M., Oguri, M., et al. 2023, ApJS, 265, 5, doi: [10.3847/1538-4365/acaaa9](https://doi.org/10.3847/1538-4365/acaaa9)
- Harikane, Y., Inoue, A. K., Ellis, R. S., et al. 2025, ApJ, 980, 138, doi: [10.3847/1538-4357/ad9b2c](https://doi.org/10.3847/1538-4357/ad9b2c)
- Harris, C. R., Millman, K. J., van der Walt, S. J., et al. 2020, Nature, 585, 357, doi: [10.1038/s41586-020-2649-2](https://doi.org/10.1038/s41586-020-2649-2)
- Heintz, K. E., Brammer, G. B., Giménez-Arteaga, C., et al. 2023, Nature Astronomy, 7, 1517, doi: [10.1038/s41550-023-02078-7](https://doi.org/10.1038/s41550-023-02078-7)
- Heintz, K. E., Watson, D., Brammer, G., et al. 2024, Science, 384, 890, doi: [10.1126/science.adj0343](https://doi.org/10.1126/science.adj0343)
- Heintz, K. E., Brammer, G. B., Watson, D., et al. 2025, A&A, 693, A60, doi: [10.1051/0004-6361/202450243](https://doi.org/10.1051/0004-6361/202450243)
- Hu, W., Papovich, C., Dickinson, M., et al. 2024, ApJ, 971, 21, doi: [10.3847/1538-4357/ad5015](https://doi.org/10.3847/1538-4357/ad5015)
- Hunter, J. D. 2007, Computing in Science and Engineering, 9, 90, doi: [10.1109/MCSE.2007.55](https://doi.org/10.1109/MCSE.2007.55)
- Iani, E., Zanella, A., Vernet, J., et al. 2023, MNRAS, 518, 5018, doi: [10.1093/mnras/stac3198](https://doi.org/10.1093/mnras/stac3198)
- Inoue, A. K., Shimizu, I., Iwata, I., & Tanaka, M. 2014, MNRAS, 442, 1805, doi: [10.1093/mnras/stu936](https://doi.org/10.1093/mnras/stu936)
- Isobe, Y., Ouchi, M., Tominaga, N., et al. 2023, ApJ, 959, 100, doi: [10.3847/1538-4357/ad09be](https://doi.org/10.3847/1538-4357/ad09be)
- Isobe, Y., Maiolino, R., D'Eugenio, F., et al. 2025, MNRAS, 541, L71, doi: [10.1093/mnras/slaf056](https://doi.org/10.1093/mnras/slaf056)
- Jakobsen, P., Ferruit, P., Alves de Oliveira, C., et al. 2022, A&A, 661, A80, doi: [10.1051/0004-6361/202142663](https://doi.org/10.1051/0004-6361/202142663)
- James, B. L., Pettini, M., Christensen, L., et al. 2014, MNRAS, 440, 1794, doi: [10.1093/mnras/stu287](https://doi.org/10.1093/mnras/stu287)
- Jaskot, A. E., & Ravindranath, S. 2016, ApJ, 833, 136, doi: [10.3847/1538-4357/833/2/136](https://doi.org/10.3847/1538-4357/833/2/136)
- Ji, X., Belokurov, V., Maiolino, R., et al. 2025, arXiv e-prints, arXiv:2505.12505, doi: [10.48550/arXiv.2505.12505](https://doi.org/10.48550/arXiv.2505.12505)
- Ji, X., Übler, H., Maiolino, R., et al. 2024, MNRAS, 535, 881, doi: [10.1093/mnras/stae2375](https://doi.org/10.1093/mnras/stae2375)
- Johnson, B. D., Leja, J., Conroy, C., & Speagle, J. S. 2021, ApJS, 254, 22, doi: [10.3847/1538-4365/abef67](https://doi.org/10.3847/1538-4365/abef67)
- Jones, T., Sanders, R., Chen, Y., et al. 2023, ApJL, 951, L17, doi: [10.3847/2041-8213/acd938](https://doi.org/10.3847/2041-8213/acd938)
- Katz, H., Rosdahl, J., Kimm, T., et al. 2023, The Open Journal of Astrophysics, 6, 44, doi: [10.21105/astro.2309.03269](https://doi.org/10.21105/astro.2309.03269)
- Katz, H., Cameron, A. J., Saxena, A., et al. 2024, arXiv e-prints, arXiv:2408.03189, doi: [10.48550/arXiv.2408.03189](https://doi.org/10.48550/arXiv.2408.03189)
- Kobayashi, C., & Ferrara, A. 2024, ApJL, 962, L6, doi: [10.3847/2041-8213/ad1de1](https://doi.org/10.3847/2041-8213/ad1de1)
- Kokorev, V., Chávez Ortiz, Ó. A., Taylor, A. J., et al. 2025, arXiv e-prints, arXiv:2504.12504, doi: [10.48550/arXiv.2504.12504](https://doi.org/10.48550/arXiv.2504.12504)
- Kovács, O. E., Bogdán, Á., Natarajan, P., et al. 2024, ApJL, 965, L21, doi: [10.3847/2041-8213/ad391f](https://doi.org/10.3847/2041-8213/ad391f)
- Kravtsov, A., & Belokurov, V. 2024, arXiv e-prints, arXiv:2405.04578, doi: [10.48550/arXiv.2405.04578](https://doi.org/10.48550/arXiv.2405.04578)

- Kremer, K., Spera, M., Becker, D., et al. 2020, *ApJ*, 903, 45, doi: [10.3847/1538-4357/abb945](https://doi.org/10.3847/1538-4357/abb945)
- Kron, R. G. 1980, *ApJS*, 43, 305, doi: [10.1086/190669](https://doi.org/10.1086/190669)
- Laporte, N., Meyer, R. A., Ellis, R. S., et al. 2021, *MNRAS*, 505, 3336, doi: [10.1093/mnras/stab1239](https://doi.org/10.1093/mnras/stab1239)
- Leja, J., Carnall, A. C., Johnson, B. D., Conroy, C., & Speagle, J. S. 2019, *ApJ*, 876, 3, doi: [10.3847/1538-4357/ab133c](https://doi.org/10.3847/1538-4357/ab133c)
- López-Sánchez, Á. R., Esteban, C., García-Rojas, J., Peimbert, M., & Rodríguez, M. 2007, *ApJ*, 656, 168, doi: [10.1086/510112](https://doi.org/10.1086/510112)
- Luridiana, V., Morisset, C., & Shaw, R. A. 2015, *A&A*, 573, A42, doi: [10.1051/0004-6361/201323152](https://doi.org/10.1051/0004-6361/201323152)
- Mainali, R., Kollmeier, J. A., Stark, D. P., et al. 2017, *ApJL*, 836, L14, doi: [10.3847/2041-8213/836/1/L14](https://doi.org/10.3847/2041-8213/836/1/L14)
- Mainali, R., Stark, D. P., Tang, M., et al. 2020, *MNRAS*, 494, 719, doi: [10.1093/mnras/staa751](https://doi.org/10.1093/mnras/staa751)
- Maiolino, R., Scholtz, J., Witstok, J., et al. 2024, *Nature*, 627, 59, doi: [10.1038/s41586-024-07052-5](https://doi.org/10.1038/s41586-024-07052-5)
- Marques-Chaves, R., Schaerer, D., Kuruvanthodi, A., et al. 2024, *A&A*, 681, A30, doi: [10.1051/0004-6361/202347411](https://doi.org/10.1051/0004-6361/202347411)
- Mason, C. A., Chen, Z., Stark, D. P., et al. 2025, *arXiv e-prints*, arXiv:2501.11702, doi: [10.48550/arXiv.2501.11702](https://doi.org/10.48550/arXiv.2501.11702)
- Mason, C. A., Trenti, M., & Treu, T. 2023, *MNRAS*, 521, 497, doi: [10.1093/mnras/stad035](https://doi.org/10.1093/mnras/stad035)
- Matthee, J., Sobral, D., Hayes, M., et al. 2021, *MNRAS*, 505, 1382, doi: [10.1093/mnras/stab1304](https://doi.org/10.1093/mnras/stab1304)
- McBride, J., Fakhouri, O., & Ma, C.-P. 2009, *MNRAS*, 398, 1858, doi: [10.1111/j.1365-2966.2009.15329.x](https://doi.org/10.1111/j.1365-2966.2009.15329.x)
- McLeod, D. J., Donnan, C. T., McLure, R. J., et al. 2024, *MNRAS*, 527, 5004, doi: [10.1093/mnras/stad3471](https://doi.org/10.1093/mnras/stad3471)
- McLure, R. J., Dunlop, J. S., Cullen, F., et al. 2018, *MNRAS*, 476, 3991, doi: [10.1093/mnras/sty522](https://doi.org/10.1093/mnras/sty522)
- Miller, M. C., & Hamilton, D. P. 2002, *MNRAS*, 330, 232, doi: [10.1046/j.1365-8711.2002.05112.x](https://doi.org/10.1046/j.1365-8711.2002.05112.x)
- Mirocha, J., & Furlanetto, S. R. 2023, *MNRAS*, 519, 843, doi: [10.1093/mnras/stac3578](https://doi.org/10.1093/mnras/stac3578)
- Morales, A. M., Finkelstein, S. L., Leung, G. C. K., et al. 2024, *ApJL*, 964, L24, doi: [10.3847/2041-8213/ad2de4](https://doi.org/10.3847/2041-8213/ad2de4)
- Nagele, C., & Umeda, H. 2023, *ApJL*, 949, L16, doi: [10.3847/2041-8213/acd550](https://doi.org/10.3847/2041-8213/acd550)
- Naidu, R. P., Oesch, P. A., van Dokkum, P., et al. 2022, *ApJL*, 940, L14, doi: [10.3847/2041-8213/ac9b22](https://doi.org/10.3847/2041-8213/ac9b22)
- Naidu, R. P., Oesch, P. A., Brammer, G., et al. 2025, *arXiv e-prints*, arXiv:2505.11263, doi: [10.48550/arXiv.2505.11263](https://doi.org/10.48550/arXiv.2505.11263)
- Nakajima, K., Ouchi, M., Isobe, Y., et al. 2023, *ApJS*, 269, 33, doi: [10.3847/1538-4365/acd556](https://doi.org/10.3847/1538-4365/acd556)
- Nakajima, K., Schaerer, D., Le Fèvre, O., et al. 2018, *A&A*, 612, A94, doi: [10.1051/0004-6361/201731935](https://doi.org/10.1051/0004-6361/201731935)
- Napolitano, L., Castellano, M., Pentericci, L., et al. 2024, *arXiv e-prints*, arXiv:2410.18763, doi: [10.48550/arXiv.2410.18763](https://doi.org/10.48550/arXiv.2410.18763)
- . 2025, *A&A*, 693, A50, doi: [10.1051/0004-6361/202452090](https://doi.org/10.1051/0004-6361/202452090)
- Narayanan, D., Stark, D. P., Finkelstein, S. L., et al. 2025, *ApJ*, 982, 7, doi: [10.3847/1538-4357/adb41c](https://doi.org/10.3847/1538-4357/adb41c)
- Neistein, E., & Dekel, A. 2008, *MNRAS*, 383, 615, doi: [10.1111/j.1365-2966.2007.12570.x](https://doi.org/10.1111/j.1365-2966.2007.12570.x)
- Nissen, P. E., Chen, Y. Q., Carigi, L., Schuster, W. J., & Zhao, G. 2014, *A&A*, 568, A25, doi: [10.1051/0004-6361/201424184](https://doi.org/10.1051/0004-6361/201424184)
- Oke, J. B., & Gunn, J. E. 1983, *ApJ*, 266, 713, doi: [10.1086/160817](https://doi.org/10.1086/160817)
- Osterbrock, D. E., & Ferland, G. J. 2006, *Astrophysics of gaseous nebulae and active galactic nuclei*
- Pei, Y. C. 1992, *ApJ*, 395, 130, doi: [10.1086/171637](https://doi.org/10.1086/171637)
- Pilyugin, L. S., Grebel, E. K., & Mattsson, L. 2012, *MNRAS*, 424, 2316, doi: [10.1111/j.1365-2966.2012.21398.x](https://doi.org/10.1111/j.1365-2966.2012.21398.x)
- Plat, A., Charlot, S., Bruzual, G., et al. 2019, *MNRAS*, 490, 978, doi: [10.1093/mnras/stz2616](https://doi.org/10.1093/mnras/stz2616)
- Pollock, C. L., Gottumukkala, R., Heintz, K. E., et al. 2025, *arXiv e-prints*, arXiv:2506.15779, <https://arxiv.org/abs/2506.15779>
- Portegies Zwart, S. F., & McMillan, S. L. W. 2002, *ApJ*, 576, 899, doi: [10.1086/341798](https://doi.org/10.1086/341798)
- Price, S. H., Bezanson, R., Labbe, I., et al. 2025, *ApJ*, 982, 51, doi: [10.3847/1538-4357/adaec1](https://doi.org/10.3847/1538-4357/adaec1)
- Qin, Y., Balu, S., & Wyithe, J. S. B. 2023, *MNRAS*, 526, 1324, doi: [10.1093/mnras/stad2448](https://doi.org/10.1093/mnras/stad2448)
- Rantala, A., Lahén, N., Naab, T., Escobar, G. J., & Iorio, G. 2025, *arXiv e-prints*, arXiv:2506.04330, doi: [10.48550/arXiv.2506.04330](https://doi.org/10.48550/arXiv.2506.04330)
- Reddy, N. A., Erb, D. K., Pettini, M., Steidel, C. C., & Shapley, A. E. 2010, *ApJ*, 712, 1070, doi: [10.1088/0004-637X/712/2/1070](https://doi.org/10.1088/0004-637X/712/2/1070)
- Reddy, N. A., Oesch, P. A., Bouwens, R. J., et al. 2018, *ApJ*, 853, 56, doi: [10.3847/1538-4357/aaa3e7](https://doi.org/10.3847/1538-4357/aaa3e7)
- Rieke, M. J., Kelly, D. M., Misselt, K., et al. 2023, *PASP*, 135, 028001, doi: [10.1088/1538-3873/acac53](https://doi.org/10.1088/1538-3873/acac53)
- Rieke, Marcia, Robertson, Brant, Tacchella, Sandro, et al. 2023, *Data from the JWST Advanced Deep Extragalactic Survey (JADES), STScI/MAST*, doi: [10.17909/8TDJ-8N28](https://doi.org/10.17909/8TDJ-8N28)
- Rigby, J., Perrin, M., McElwain, M., et al. 2023, *PASP*, 135, 048001, doi: [10.1088/1538-3873/acb293](https://doi.org/10.1088/1538-3873/acb293)

- Roberts-Borsani, G., Treu, T., Shapley, A., et al. 2024, ApJ, 976, 193, doi: [10.3847/1538-4357/ad85d3](https://doi.org/10.3847/1538-4357/ad85d3)
- Roberts-Borsani, G. W., Ellis, R. S., & Laporte, N. 2020, MNRAS, 497, 3440, doi: [10.1093/mnras/staa2085](https://doi.org/10.1093/mnras/staa2085)
- Robertson, B., Johnson, B. D., Tacchella, S., et al. 2024, ApJ, 970, 31, doi: [10.3847/1538-4357/ad463d](https://doi.org/10.3847/1538-4357/ad463d)
- Sanders, R. L., Shapley, A. E., Topping, M. W., Reddy, N. A., & Brammer, G. B. 2024, ApJ, 962, 24, doi: [10.3847/1538-4357/ad15fc](https://doi.org/10.3847/1538-4357/ad15fc)
- Sanders, R. L., Shapley, A. E., Kriek, M., et al. 2016, ApJ, 816, 23, doi: [10.3847/0004-637X/816/1/23](https://doi.org/10.3847/0004-637X/816/1/23)
- Sanders, R. L., Shapley, A. E., Reddy, N. A., et al. 2020, MNRAS, 491, 1427, doi: [10.1093/mnras/stz3032](https://doi.org/10.1093/mnras/stz3032)
- Saxena, A., Cameron, A. J., Katz, H., et al. 2024, arXiv e-prints, arXiv:2411.14532, doi: [10.48550/arXiv.2411.14532](https://doi.org/10.48550/arXiv.2411.14532)
- Schaerer, D., Marques-Chaves, R., Xiao, M., & Korber, D. 2024, A&A, 687, L11, doi: [10.1051/0004-6361/202450721](https://doi.org/10.1051/0004-6361/202450721)
- Senchyna, P., Plat, A., Stark, D. P., et al. 2024, ApJ, 966, 92, doi: [10.3847/1538-4357/ad235e](https://doi.org/10.3847/1538-4357/ad235e)
- Senchyna, P., Stark, D. P., Chevallard, J., et al. 2019, MNRAS, 488, 3492, doi: [10.1093/mnras/stz1907](https://doi.org/10.1093/mnras/stz1907)
- Senchyna, P., Stark, D. P., Vidal-García, A., et al. 2017, MNRAS, 472, 2608, doi: [10.1093/mnras/stx2059](https://doi.org/10.1093/mnras/stx2059)
- Shapley, A. E., Reddy, N. A., Sanders, R. L., Topping, M. W., & Brammer, G. B. 2023, ApJL, 950, L1, doi: [10.3847/2041-8213/acd939](https://doi.org/10.3847/2041-8213/acd939)
- Shapley, A. E., Sanders, R. L., Salim, S., et al. 2022, ApJ, 926, 145, doi: [10.3847/1538-4357/ac4742](https://doi.org/10.3847/1538-4357/ac4742)
- Shen, X., Vogelsberger, M., Boylan-Kolchin, M., Tacchella, S., & Kannan, R. 2023, MNRAS, 525, 3254, doi: [10.1093/mnras/stad2508](https://doi.org/10.1093/mnras/stad2508)
- Somerville, R. S., Yung, L. Y. A., Lancaster, L., et al. 2025, arXiv e-prints, arXiv:2505.05442, doi: [10.48550/arXiv.2505.05442](https://doi.org/10.48550/arXiv.2505.05442)
- Speagle, J. S., Steinhardt, C. L., Capak, P. L., & Silverman, J. D. 2014, ApJS, 214, 15, doi: [10.1088/0067-0049/214/2/15](https://doi.org/10.1088/0067-0049/214/2/15)
- Stark, D. P., Topping, M. W., Endsley, R., & Tang, M. 2025, arXiv e-prints, arXiv:2501.17078, doi: [10.48550/arXiv.2501.17078](https://doi.org/10.48550/arXiv.2501.17078)
- Stark, D. P., Richard, J., Siana, B., et al. 2014, MNRAS, 445, 3200, doi: [10.1093/mnras/stu1618](https://doi.org/10.1093/mnras/stu1618)
- Stark, D. P., Walth, G., Charlot, S., et al. 2015, MNRAS, 454, 1393, doi: [10.1093/mnras/stv1907](https://doi.org/10.1093/mnras/stv1907)
- Steidel, C. C., Strom, A. L., Pettini, M., et al. 2016, ApJ, 826, 159, doi: [10.3847/0004-637X/826/2/159](https://doi.org/10.3847/0004-637X/826/2/159)
- Sun, G., Faucher-Giguère, C.-A., Hayward, C. C., et al. 2023, ApJL, 955, L35, doi: [10.3847/2041-8213/acf85a](https://doi.org/10.3847/2041-8213/acf85a)
- Tacchella, S., Finkelstein, S. L., Bagley, M., et al. 2022, ApJ, 927, 170, doi: [10.3847/1538-4357/ac4cad](https://doi.org/10.3847/1538-4357/ac4cad)
- Tacchella, S., Eisenstein, D. J., Hainline, K., et al. 2023a, ApJ, 952, 74, doi: [10.3847/1538-4357/acdbbc6](https://doi.org/10.3847/1538-4357/acdbbc6)
- Tacchella, S., Johnson, B. D., Robertson, B. E., et al. 2023b, MNRAS, 522, 6236, doi: [10.1093/mnras/stad1408](https://doi.org/10.1093/mnras/stad1408)
- Tang, M., Stark, D. P., Chevallard, J., & Charlot, S. 2019, MNRAS, 489, 2572, doi: [10.1093/mnras/stz2236](https://doi.org/10.1093/mnras/stz2236)
- Tang, M., Stark, D. P., Chevallard, J., et al. 2021, MNRAS, 501, 3238, doi: [10.1093/mnras/staa3454](https://doi.org/10.1093/mnras/staa3454)
- Tang, M., Stark, D. P., & Ellis, R. S. 2022, MNRAS, 513, 5211, doi: [10.1093/mnras/stac1280](https://doi.org/10.1093/mnras/stac1280)
- Tang, M., Stark, D. P., Ellis, R. S., et al. 2024a, ApJ, 972, 56, doi: [10.3847/1538-4357/ad5ae0](https://doi.org/10.3847/1538-4357/ad5ae0)
- Tang, M., Stark, D. P., Topping, M. W., Mason, C., & Ellis, R. S. 2024b, arXiv e-prints, arXiv:2408.01507, doi: [10.48550/arXiv.2408.01507](https://doi.org/10.48550/arXiv.2408.01507)
- Tang, M., Stark, D. P., Chen, Z., et al. 2023, MNRAS, 526, 1657, doi: [10.1093/mnras/stad2763](https://doi.org/10.1093/mnras/stad2763)
- Topping, M. W., Stark, D. P., Endsley, R., et al. 2022, ApJ, 941, 153, doi: [10.3847/1538-4357/aca522](https://doi.org/10.3847/1538-4357/aca522)
- . 2024a, MNRAS, 529, 4087, doi: [10.1093/mnras/stae800](https://doi.org/10.1093/mnras/stae800)
- Topping, M. W., Stark, D. P., Senchyna, P., et al. 2024b, MNRAS, 529, 3301, doi: [10.1093/mnras/stae682](https://doi.org/10.1093/mnras/stae682)
- . 2025a, ApJ, 980, 225, doi: [10.3847/1538-4357/ada95c](https://doi.org/10.3847/1538-4357/ada95c)
- Topping, M. W., Sanders, R. L., Shapley, A. E., et al. 2025b, arXiv e-prints, arXiv:2502.08712, doi: [10.48550/arXiv.2502.08712](https://doi.org/10.48550/arXiv.2502.08712)
- Toribio San Cipriano, L., García-Rojas, J., Esteban, C., Bresolin, F., & Peimbert, M. 2016, MNRAS, 458, 1866, doi: [10.1093/mnras/stw397](https://doi.org/10.1093/mnras/stw397)
- Treu, T., Roberts-Borsani, G., Bradac, M., et al. 2022, ApJ, 935, 110, doi: [10.3847/1538-4357/ac8158](https://doi.org/10.3847/1538-4357/ac8158)
- Treu, Tommaso, & Paris, Diego. 2023, High-level science products produced by the GLASS-JWST team, as described in Paris, et al. 2024 (ADS bibcode: 2023ApJ...952...20P), and in Mascia, et al. 2024 (ADS bibcode: 2024A&A...690A...2M), STScI/MAST, doi: [10.17909/KW3C-N857](https://doi.org/10.17909/KW3C-N857)
- Valentino, F., Brammer, G., Gould, K. M. L., et al. 2023, ApJ, 947, 20, doi: [10.3847/1538-4357/acbefa](https://doi.org/10.3847/1538-4357/acbefa)
- Virtanen, P., Gommers, R., Oliphant, T. E., et al. 2020, Nature Methods, 17, 261, doi: [10.1038/s41592-019-0686-2](https://doi.org/10.1038/s41592-019-0686-2)
- Wang, B., Fujimoto, S., Labbé, I., et al. 2023, ApJL, 957, L34, doi: [10.3847/2041-8213/acfe07](https://doi.org/10.3847/2041-8213/acfe07)
- Whitler, L., Endsley, R., Stark, D. P., et al. 2023a, MNRAS, 519, 157, doi: [10.1093/mnras/stac3535](https://doi.org/10.1093/mnras/stac3535)
- Whitler, L., Stark, D. P., Endsley, R., et al. 2023b, MNRAS, 519, 5859, doi: [10.1093/mnras/stad004](https://doi.org/10.1093/mnras/stad004)

Whitler, L., Stark, D. P., Topping, M. W., et al. 2025, arXiv e-prints, arXiv:2501.00984, doi: [10.48550/arXiv.2501.00984](https://doi.org/10.48550/arXiv.2501.00984)

Witstok, J., Jakobsen, P., Maiolino, R., et al. 2025a, Nature, 639, 897, doi: [10.1038/s41586-025-08779-5](https://doi.org/10.1038/s41586-025-08779-5)

Witstok, J., Maiolino, R., Smit, R., et al. 2025b, MNRAS, 536, 27, doi: [10.1093/mnras/stae2535](https://doi.org/10.1093/mnras/stae2535)

Ziparo, F., Ferrara, A., Sommovigo, L., & Kohandel, M. 2023, MNRAS, 520, 2445, doi: [10.1093/mnras/stad125](https://doi.org/10.1093/mnras/stad125)